# Precise Measurement of Photomultiplier Tube Non-Linearity for the MOLLER Experiment

by

M.P.A.V. Gunawardhana

A Thesis submitted to the Faculty of Graduate Studies of

The University of Manitoba

in partial fulfilment of the requirements of the degree of

MASTER OF SCIENCE

Department of Physics and Astronomy

University of Manitoba

Winnipeg

# Abstract

The MOLLER (Measurement of a Lepton-Lepton Electroweak Reaction) experiment is an international collaboration formed to achieve unprecedented precision in measuring the parity-violating asymmetry in electron-electron scattering to probe the weak mixing angle, and to explore potential physics beyond the Standard Model. A critical component of this measurement is the use of photomultiplier tubes (PMTs) operating in integration mode within the main detector array. Accurate characterization of PMT non-linearity is essential to minimize systematic uncertainties.

This study develops and validates a robust methodology for measuring the non-linearity of PMTs under conditions replicating those of the MOLLER experiment. A novel bench-top apparatus integrating UV-LED light sources, optical chopper, neutral density (ND) filters and a light diffuser was designed to generate controlled light signals mimicking the experimental environment. Automation techniques were leveraged heavily when implementing the data collection to efficiently evaluate over 300 PMTs while achieving the stringent MOLLER's PMT non-linearity precision goal of $\pm 0.1\%$.

The results demonstrate that PMT non-linearity (differential) remains below the critical threshold of 0.5%, confirming their suitability for the MOLLER experiment. These findings provide confidence in the integrity of the detector system and ensure the precision required for the measurement of parity-violating asymmetry. Beyond its immediate application, this study contributes to the broader field of experimental particle physics by advancing methods for detector characterization and by setting a benchmark for similar high-precision measurements.

# Acknowledgment

First, I would like to express my deepest gratitude to my advisor, Dr.Savino Longo, for his unwavering support, guidance, and insightful feedback throughout the course of this research. His expertise and encouragement have been invaluable.

I also wish to extend my thanks to the members of my thesis committee, Dr.Michael Gericke and Dr.Jessica Rodgers, for their time, advice, and constructive critiques.

Special thanks to undergraduate students Tavleen Kainth, Jocelyn Roney, and Anish Madaan, for their invaluable assistance with the data collection. I am grateful to the administrative team in the Department of Physics and Astronomy, including Susan Beshta, Aysley Bishop-Mahon, Milijana Prstojevic, and IT personnel Maiko Langelaar, for their support.

I would also like to acknowledge the MOLLER collaboration team at the University of Manitoba, including Dr.Michael Gericke, Dr.Mohammad Laheji, Dr.Jie Pan, Brynne Blaikie, Nafis Niloy, and Kristofer Isaak, for their continuous support.

My heartfelt thanks go to my family for their constant love, support, and encouragement. Your belief in me has been a driving force in completing this thesis.

Finally, I gratefully acknowledge the financial support from Research Manitoba.

# Contents

# Chapter 1

# Introduction and Background

## 1.1 Standard Model

The Standard Model in particle physics refers to the most accurate theory that scientists have developed to describe how fundamental particles and forces interact, excluding gravity [1]. It integrates three of the four known fundamental forces: electromagnetic, weak, and strong interactions. With the help of the Standard Model, physicists now have a better understanding of how these particles interact to form the complex structures observed in nature. Despite its success, the Standard Model leaves some fundamental questions unanswered. Experiments such as MOLLER, discussed in detail later in this chapter, aim to address these gaps through highly precise measurements.

### 1.1.1 Elementary Particles

In the current view, the universe is considered to be made up of three kinds of elementary particles: quarks, leptons, and mediators. There are six leptons and six *flavors* of quarks categorized into three generations, with each generation containing a pair of quarks and a pair of leptons. These fundamental particles are often categorized into groups using *spin*, an intrinsic property of particles that indicates the amount of angular momentum associated with them [1].

Fermions are a group of particles that have half-odd-integer spins (spin $\frac{1}{2}$, spin $\frac{3}{2}$, etc.). All quarks and leptons are spin $\frac{1}{2}$ particles. Therefore, all 12 quarks and leptons are grouped under fermions. Table 1.1 shows the three generations of fermions [1, 2].

Quarks have different flavors (up, down, charm, strange, top, bottom) and they are the only known elementary particles that experience all four fundamental interactions.

Table 1.1: Categorization of fundamental particles.

| **Fermions** | **Generations** | | |
|---|---|---|---|
| | **I** | **II** | **III** |
| Quark | up (u)<br>down (d) | charm (c)<br>strange (s) | top (t)<br>bottom (b) |
| Leptons | e<br>$\nu_e$ | $\mu$<br>$\nu_\mu$ | $\tau$<br>$\nu_\tau$ |

Quarks combine to make composite particles called hadrons, the most stable of which are protons and neutrons, with compositions of *uud* and *udd*, respectively. Quarks are never found in isolation and are always found only within hadrons. Although hadrons composed of generation II and III quarks have been observed in laboratory settings, all commonly observable matter is composed of up quarks, down quarks, and electrons [1].

Leptons are elementary particles with half integer spin that participate in all other fundamental interactions except for strong interactions. Leptons come in six different types: electron, muon, tau, and their corresponding neutrinos [1].

Bosons are integer spin particles (a boson with spin 2, called the graviton [2] has been theorized but has not yet been integrated into the Standard Model). *Gauge bosons* are responsible for mediating fundamental interactions between matter particles. There are four known kinds of gauge bosons: photon, W and Z bosons, and gluons. The electromagnetic interaction is mediated by photons which are responsible for interaction between electrically charged particles. Gluons mediate the strong interactions that bind quarks together. Finally, the weak force, which governs the interactions involving all fermions, is mediated by the W and Z bosons. Table 1.2 summarizes the fundamental interactions and their mediator particles [1, 2].

Bosons with spin 0 are call *scalar bosons* and there is only one kind, the Higgs boson. It is a fundamental particle associated with the Higgs field, which gives mass to the W and Z bosons through the mechanism of *spontaneous symmetry breaking* [1]. The discovery of the Higgs boson at CERN's Large Hadron Collider (LHC) in 2012 confirmed the existence of the Higgs field [3].

### 1.1.2 Fundamental Forces

Forces or interactions that cannot be reduced to simpler forms are called fundamental forces. All interactions in the universe can be broken down into four basic forms;

gravity, electromagnetism, weak interaction, and strong interaction. The gravitational force is described by Einstein's general theory of relativity as the curvature of *spacetime*. The other three forces are mathematically described as discrete quantum fields whose interactions are mediated by elementary force carrier particles [1].

Table 1.2: Summary of fundamental forces and force mediating particles [1].

| **Interaction** | **Mediator** |
|---|---|
| Strong | Gluon |
| Electromagnetic | Photon |
| Weak | W and Z |
| Gravitational | Graviton[†] |

[†]The graviton is a hypothetical particle that mediates the gravitational force.

Electromagnetism describes the interactions between electrically charged particles and photons. The electromagnetic (EM) force is mediated by the exchange of photons [1] and is the dominant interaction responsible for phenomena such as electron–electron scattering. However, it is not the only interaction that allows electron–electron scattering, as weak interactions can also contribute at higher energy scales, albeit with much smaller probabilities [4].

Weak interaction is responsible for processes like beta decay in radioactive nuclei. The weak force is mediated by the W and Z bosons, and operates at very short ranges, much shorter than the electromagnetic and strong forces [1].

Strong interaction describes the interactions between quarks and gluons. The strong force binds quarks together to form protons, neutrons, and other hadrons, and is mediated by the exchange of gluons. This is the strongest of the four fundamental forces [1].

Although the theory of general relativity can describe the behavior of gravity on a macroscopic scale, there is no mechanism to explain how the gravitational force operates at the quantum level. It has been theorized that gravitational interaction is mediated by a particle called the *graviton* [2], but it has not been observed. Therefore, gravity is not included in the Standard Model. Figure 1.1 summarizes elementary particles and their corresponding interactions.

### 1.1.3 Experimental Verification

The Standard Model has been remarkably successful in predicting the existence of elementary particles such as the W and Z bosons, gluons, the top quark, and the charm

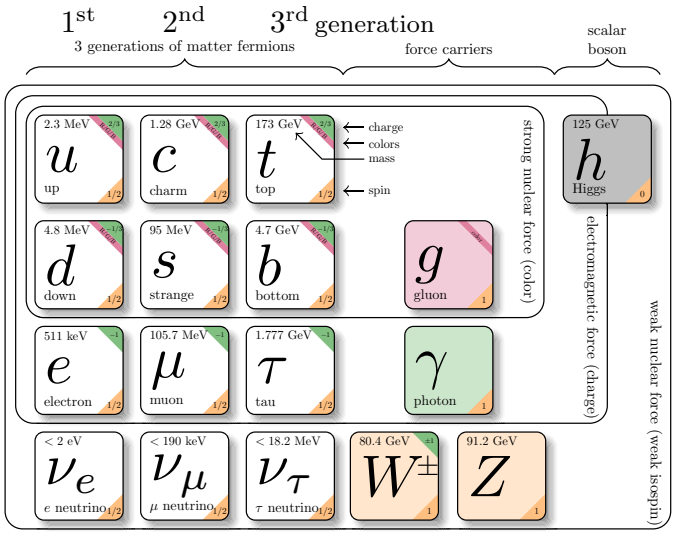


Figure 1.1: The Standard Model of particle physics. Consist of elementary particles and their interactions [5].

quark [1]. These predictions were experimentally confirmed with high precision using particle accelerators, such as the LHC at CERN and the Tevatron at Fermilab. The discovery of the Higgs boson at the LHC in 2012 [3] was the final fundamental particle predicted by the Standard Model to be confirmed experimentally.

Considering the electroweak sector of the Standard Model, the SLAC-E158 experiment [6] was the first to measure the *parity-violating asymmetry* in electron-electron scattering, confirming predictions of the Standard Model within their uncertainties.

### 1.1.4 Unsolved Questions in the Standard Model

Although the Standard Model is the most successful theory of particle physics to date, it is not without its flaws. It is fundamentally an incomplete theory, as it fails to adequately explain certain fundamental physical phenomena in nature like gravity, nature of dark matter, and matter-antimatter asymmetry of the universe. Apart from these major limitations, there are numerous questions that need answers [1, 2].

The MOLLER experiment is going to probe the limits of the electroweak sector of the standard model hoping to answer several unsolved questions [7],

- Is there any evidence of new particles or forces beyond the Standard Model?
- What is the true nature of the *weak mixing angle* at low energies, and will it deviate from the Standard Model prediction if measured extremely precisely?
- Can low-energy precision experiments detect dark sector interactions?

### 1.1.5 Parity

If a system undergoes a certain transformation and remain unchanged, the system is said to be symmetric under that transformation. For example, a circle is symmetric under rotation, which is a continuous symmetry. It also has mirror symmetries through its diameter, which is an example of a discrete symmetry. These physical symmetries are important because Noether's Theorem indicates that symmetries in nature reflect underlying conservation laws [1].

In quantum mechanics, parity relates to the symmetry of the wave function of a system under spatial inversion [1]. The parity operator **P** transforms such a system into its mirrored image. Mathematically, this is done by inverting the algebraic sign of one of the spatial coordinates. In the case of point reflection, the signs of all spatial coordinates are simultaneously flipped, as shown in Equation 1.1.

$$\mathbf{P}: \begin{bmatrix} x \\ y \\ z \end{bmatrix} \rightarrow \begin{bmatrix} -x \\ -y \\ -z \end{bmatrix} \tag{1.1}$$

Helicity is the projection of the spin $\vec{s}$ into the direction of momentum $\vec{p}$. Figure 1.2 shows how parity transformation changes the helicity of a particle.

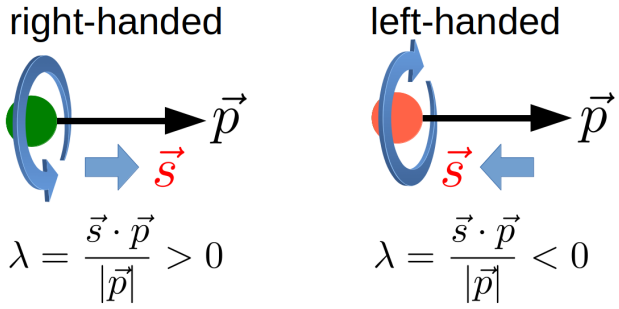


Figure 1.2: Helicity $\lambda$ of a particle is right-handed (positive) if spin and direction of motion is parallel. Left-handed (negative) if the spin and direction of motion is antiparallel [5].

Under parity transformations, the helicity of a particle is flipped because it changes the direction of the momentum $\vec{p}$.

### 1.1.6 Parity Violation in Weak Interaction

Before 1956, it was commonly believed that the laws of physics were the same for the mirrored image of any physical system. However, Lee and Yang [8] proposed that

the weak interaction might violate this parity symmetry. Later that year, Wu [9] resolved this issue with an experiment involving radioactive Cobalt-60 nuclei. Wu observed that the direction of the emitted beta decayed electrons was independent of the initial spin of the Cobalt-60 nuclei. This finding provided evidence of parity violation in weak interaction [1]. Lee and Yang were awarded the Nobel Prize for this discovery in 1957.

With these new results and ample evidence for parity invariance in strong and electromagnetic processes, parity violation became practically the signature of weak interactions. It violates parity the strongest possible way [1, 2].

## 1.2 Weak Mixing Angle

Weak mixing angle, also known as the Weinberg angle and denoted by $\theta_W$, is a parameter in the Standard Model that describes the mixing between the two fundamental interactions: the weak interaction and the electromagnetic interaction [5].

This mixing is part of the electroweak unification which combined weak and electromagnetic interactions, and describe them as different manifestations of a single underlying force. In 1979, physicists S. Glashow, A. Salam, and S. Weinberg were jointly awarded the Nobel Prize for their work on unifying the weak and electromagnetic forces. Their research led to the development of the Glashow-Weinberg-Salam theory [10, 11].

Coupling strengths (a dimensionless quantity that specifies the strength of the interaction) of electromagnetic and weak interactions, $g$ and $g'$ can be used to define the weak mixing angle as $\tan\theta_W = g'/g$ [5]. The angle can also be defined using the relationship between the masses of W and Z bosons ($M_W$ and $M_Z$) as in Equation 1.2 [2].

$$\sin^2\theta_W = 1 - \left(\frac{M_W}{M_Z}\right)^2 = 0.231\ 21(4) \tag{1.2}$$

Since $\theta_W$ is a fundamental parameter of the Standard Model, precisely measuring it is a valuable tool for cross-checking the consistency of the Standard Model across different energy scales.

## 1.3 MOLLER Experiment

The MOLLER (Measurement of a Lepton-Lepton Electroweak Reaction) experiment is an international collaboration designed to measure the weak mixing angle ($\theta_W$) using parity-violating asymmetry in the scattering of longitudinally polarized electrons off unpolarized target electrons ($A_{\mathrm{PV}}$). A key differentiating factor of this experiment compared to previous similar experiments, is its proposed precision at low momentum transfers. MOLLER aims to measure the weak mixing angle with a precision of $\delta(\sin^2\theta_W) = \pm 0.00028$. This level of precision is several orders of magnitude higher than previous measurements at similar energy scales, as shown in Figure 1.3 [7].

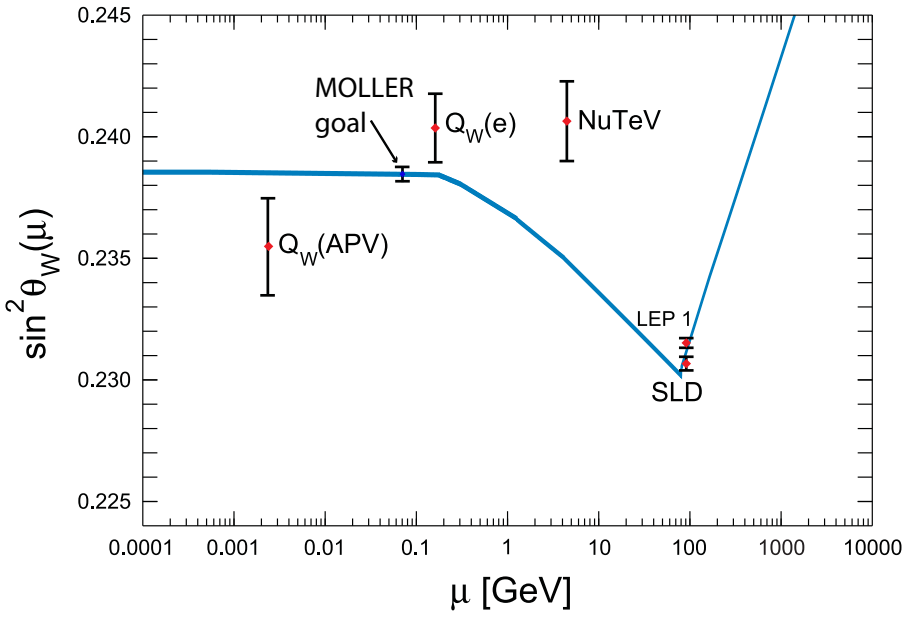


Figure 1.3: Running of weak mixing angle $\sin^2\theta_W(\mu)$ is shown with the proposed MOLLER measurement at expected $\mu$ energy scale with error bar. The central value was set to nominal Standard Model prediction [7].

.

The experiment proposes to measure the $A_{PV}$ in electron-electron scattering, which is also known as Møller scattering. In electroweak theory, this process described at the tree level by Feynman diagrams involving interactions through a photon and the $Z^0$ boson, as shown in Figure 1.4. The $Z^0$ weak interaction is a purely left-handed process, while the photon is symmetric by nature. Therefore, the scattering cross-section ($\sigma$) depends on the polarization of the electrons ($\sigma_R \neq \sigma_L$) . The electron $A_{\mathrm{PV}}$ can be expressed as in the Equation 1.3 [7].

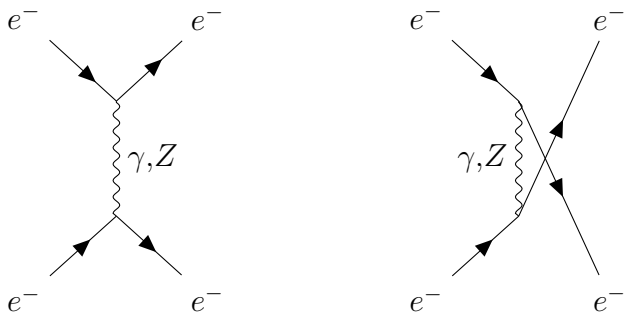


Figure 1.4: Møller scattering tree level Feynman diagrams [12].

$$A_{\mathrm{PV}} = \frac{\sigma_R - \sigma_L}{\sigma_R + \sigma_L} = mE \frac{G_F}{\sqrt{2}\pi\alpha} \frac{4\sin^2\theta}{(3+\cos^2\theta)^2} Q_W^e \tag{1.3}$$

Where $Q_W^e$ is called the *weak charge*, $E$ is the incident beam energy, the fine structure constant is denoted as $\alpha$, $\theta$ is the scattering angle in the center of mass frame, $G_F$ is the Fermi constant, and $m$ is the electron mass. The weak charge is expressed as $Q_W^e = 1 - 4\sin^2\theta_W$ at the tree level, and it is depended on the energy scale at which the experiment is conducted when modified at the 1-loop level [7]. This *running* of $\sin^2\theta_W$ is illustrated in Figure 1.3.

The $A_{\mathrm{PV}}$ for the proposed experiment is anticipated to be approximately 33 parts per billion (ppb), and MOLLER aims to measure it with a precision of 0.7 ppb, resulting in an overall fractional accuracy of 2.4% [7]. MOLLER's $A_{\mathrm{PV}}$ measurement, performed at low energy, will be the first to match the precision of high-energy measurements previously conducted at the $Z^0$ resonance ($\sim 90\,GeV$) [7]. The total Møller scattering cross-section ($\sigma$) can be expressed as Equation 1.4 [13] using the electromagnetic scattering amplitude through photon ($\mathcal{M}_\gamma$), and the scattering amplitude due to weak interaction through Z ($\mathcal{M}_Z$).

$$\sigma \propto |\mathcal{M}_\gamma + \mathcal{M}_Z|^2 = \mathcal{M}_\gamma^2 + \mathcal{M}_Z^2 + 2\mathcal{M}_\gamma\mathcal{M}_Z \tag{1.4}$$

At lower energies ($\ll M_Z$), the probability of scattering through Z goes to zero and the interference term $2\mathcal{M}_\gamma\mathcal{M}_Z$ give rise to the parity violation [13].

MOLLER's precision measurement at low energies makes it highly sensitive to hypothetical new interactions, and can detect interactions with strengths as low as $\sim 10^3 \cdot G_F$ (where $G_F$ is the Fermi constant), which provide a sensitivity of 7.5 TeV in effective mass scale. This means MOLLER could reveal influences from particles or forces too weak to appear directly at colliders like the LHC [7].

Low energy transfers experiments like MOLLER will have the sensitivity to explore possible *Beyond Standard Model* physics event detected by LHC. Figure 1.5 shows the predicted deviations of the $\sin^2\theta_W$ if exists a theorized particle "dark" Z for two proposed masses [7].

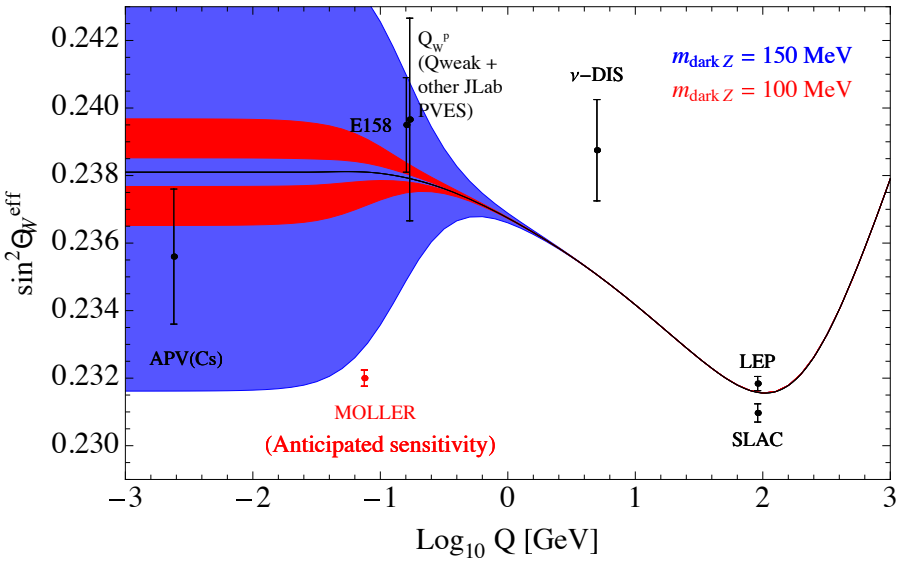


Figure 1.5: Theorized deviations of the $\sin^2\theta_W$ to explain the existence of dark Z [7].

### 1.3.1 MOLLER Apparatus

The MOLLER experiment proposes to conduct measurements using the upgraded 11 GeV polarized electron beam at Jefferson Laboratory (JLab) in Virginia, USA. The CAD design of MOLLER the apparatus, which is planned to be placed in Hall A at JLab, is shown in Figure 1.6 [7].

First, the electron beam will hit the liquid hydrogen target, and Møller electrons (beam electrons scattered from the target) will be separated from the background using the spectrometer system. It comprises a pair of toroidal magnet assemblies and precise collimators to filter the Møller events from the elastically and inelastically scattered electrons from the nuclei in the target. The filtered electrons are then focused onto detectors in the main electron detector [7].

Rather than counting individual electrons, the main detector array is designed to precisely measure the scattered electron flux through the integration of the incident signal. Use of a flux integration technique to detect and record particles is required for high precision measurements of minuscule polarization-dependent Møller scattering asymmetries. The spectrometer is responsible for spatially separating the Møller

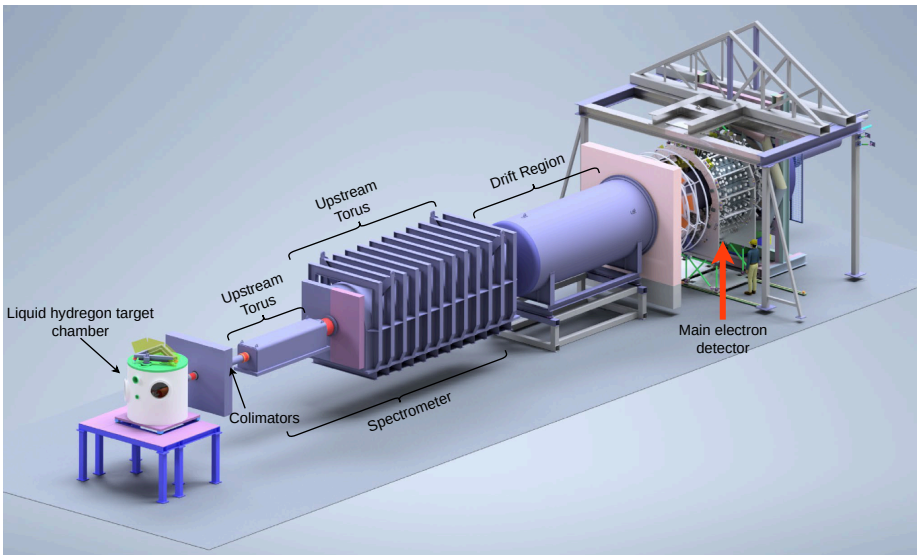


Figure 1.6: MOLLER experiment layout [14]. Main detector sits at the end of the beam-line (marked with a red arrow) is where the $A_{\text{PV}}$ is measured.

electrons from the background such as elastic and inelastic electron-proton scattering. The apparatus compares the integrated flux rate measurements ($F$) from the detectors with opposite beam helicity polarizations (right-handed and left-handed). The scattering asymmetry $A^{\text{raw}}$ is then measured for a pair of helicity-changing windows as shown in Equation 1.5. This is the raw asymmetry measured at the detectors, which requires additional corrections (Equation 1.6) for it to be used as the final $A_{\text{PV}}$ (Equation 1.3). The helicity reversal is performed at a high frequency of 1920 Hz to measure the asymmetry in a short time frame, thereby avoiding variations in experimental conditions [15].

$$A^{\text{raw}} \equiv \left( \frac{F_R - F_L}{F_R + F_L} \right) \tag{1.5}$$

### 1.3.2 Integrating Detector

The construction of the main detector, which is being built by the team at the University of Manitoba, is shown in Figure 1.7, along with its inner detector modules. This thesis contributes to the commissioning of the main integrating detector by characterizing all the photomultiplier tubes (PMTs) installed within it.

The main electron detector consists of 224 detector modules arranged in 6 radial rings around the beamline as shown in Figure 1.7. Each detector module has three main components; a fused silica (quartz) tile, a photomultiplier tube (PMT), and a light guide. The quartz tile, which act as a Cherenkov radiator, is positioned at the

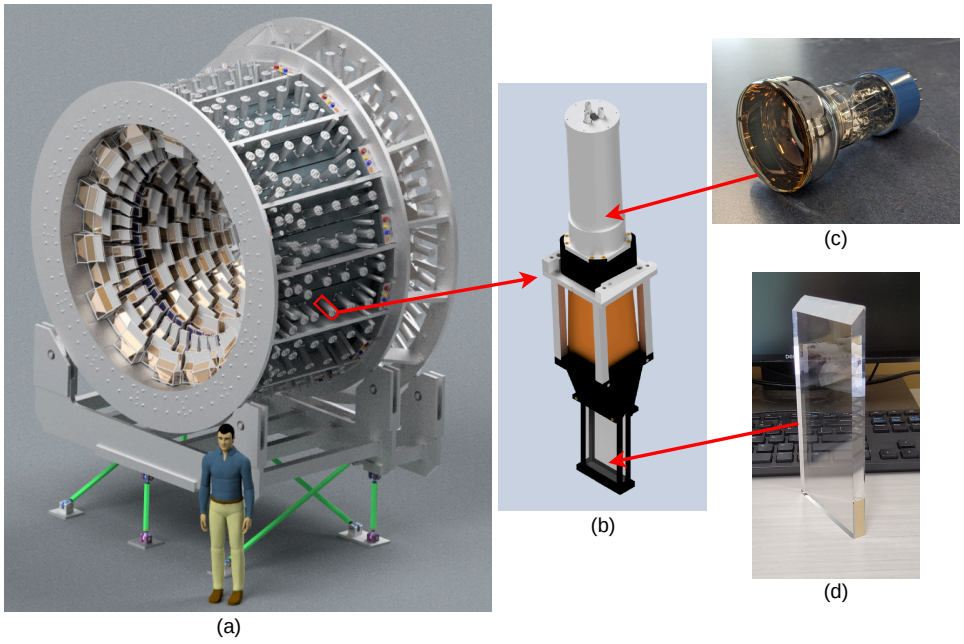


Figure 1.7: CAD design of the (a) MOLLER main integrating electron detector and (b) a *detector module*. (c) Photomultiplier Tube which is placed at the end of the detector module. (d) A quartz crystal that goes inside the main detector [7].

front of the detector module. The quartz tiles are positioned inside the main detector ring (as shown in Figure 1.7(a)) and are exposed to the incoming scattered electrons. The collimator in the MOLLER apparatus ensures that the tiles have no line-of-sight to the target to reduce background. Scattered electrons generate Cherenkov light inside the quartz tiles if the speed of the electrons are greater than the speed of light in the quartz medium. The geometry of the tiles are precisely controlled during the polishing process to ensure that the generated light is totally internally reflected until it exits at the back of the tile [15].

The Cherenkov photons then enter the air-core light guide, which direct the photons towards the PMT at the top. The light guide's geometry is calibrated to minimize the background by increasing the number of reflections for the photons generated by Cherenkov events within the light guide and reducing reflections for photons entering the light guide from the quartz crystal [15]. According to Figure 1.8(b) which shows the wavelength distribution of Cherenkov photons per unit length in the quartz tile, most of the generated photons are in the ultraviolet region.

The final part of the detector module is the PMT, which detects the Cherenkov photons and generates electrical signals proportional to the incident flux of electrons. These signals from the PMT are conditioned by the PMT electronics in the PMT base

(see Section 1.4.2) then fed to the data acquisition (DAQ) system to digitize. More details about the PMT construction and operation are discussed later in Section 1.4.

As discussed in the previous section, the spectrometer spatially separates the Møller electrons from background and delivers them to the rings of the main detector. Figure 1.8(a) shows the radial distribution of the detector rates for the proposed six-ring segmentation. The final Møller $A_{\mathrm{PV}}$ will be calculated using measurements from Ring 5, where the Møller peak is located. Most of the elastically scattered electrons from the target nucleus are concentrated closer to the beamline in Ring 2.

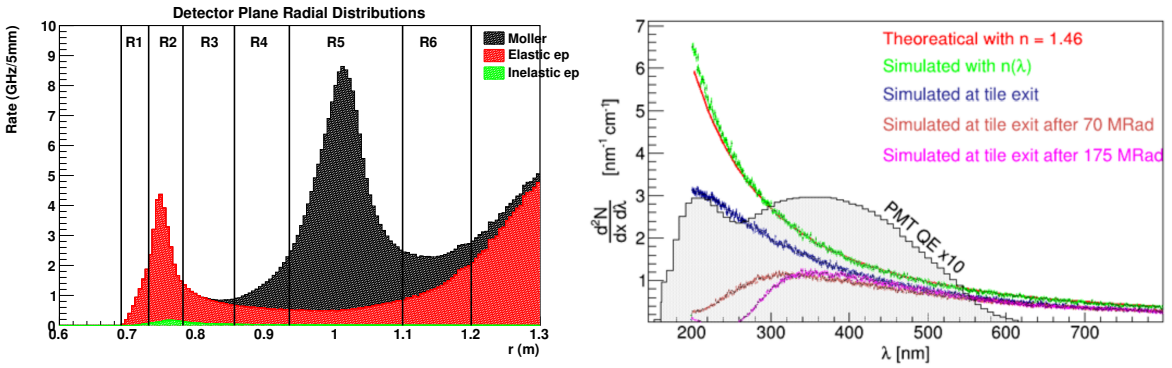


(a) (b)

Figure 1.8: (a): Radial distribution of the detector rates for Møller, elastic and inelastic electron scattering [7]. (b): Theoretical (red) and simulated (green) Cherenkov photons generation distribution in quartz crystal as a function of wavelength $\lambda$. Gray area shows the quantum efficiency of the PMT used for prototyping [15].

## 1.4 Photomultiplier Tubes

Photomultiplier tubes (PMTs) are highly sensitive light detectors. They work by converting photons into electrical signals through the *photoelectric effect* and subsequent electron multiplication [16]. For the construction of the main detector in the MOLLER apparatus, 224 PMTs are proposed to be used to detect Cherenkov light generated by the quartz detector tiles.

### 1.4.1 Anatomy of a Photomultiplier Tube

Photomultiplier Tube (PMT) is a vacuum tube consisting of an input window, a photocathode, focusing electrodes, electron multipliers, and an anode to measure the output signal. Basic construction of a PMT is shown in Figure 1.9. Incoming

photons pass through the input window and strike the photo-sensitive photocathode. Photons excite electrons in the photocathode, causing photo-electron emission into the vacuum [16].

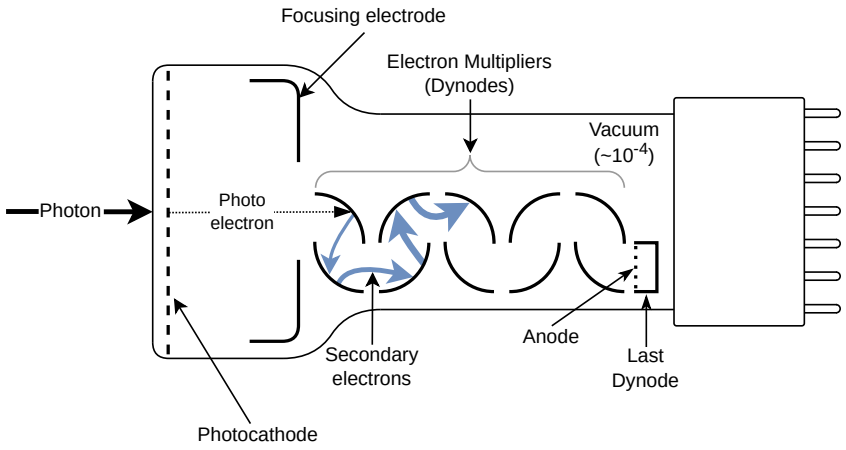


Figure 1.9: Basic elements of a photomultiplier tube.

These photo-electrons are accelerated and focused by the focusing electrodes onto the dynode chain, where they are multiplied at each stage through *secondary electron emission*. A single photoelecton multiplied up to $10^8$ times during this process before being extracted at the anode. PMTs are used to reliably produce a current output that is proportional to the incident photon flux. However, a PMT requires a high-voltage source and a voltage divider to distribute the desired voltages to the dynodes to produce a measurable output at the anode. The required high voltage typically ranges from 500 V to 2000 V [16].

PMTs have two operational modes. *Pulse mode* is where the PMTs have the capability to distinguish single photons. However, the MOLLER experiment is expected to observer electron rates as high as several GHz (see Figure 1.8(a)) at some quartz tiles. At such high rates, it is not feasible to count individual electrons, necessitating the operation of PMTs in *integration mode*. When individual photon pulses overlap, they produce a continuous current at the photocathode. Hence, this mode of operation is sometimes referred to as the *current mode*. For high-rate detectors in the MOLLER experiment, cathode currents are expected to range between 10 and 25 nA [15].

The manufacturer of the PMT specifies the maximum anode current that the PMT can handle. Consequently, at a given cathode current, the maximum anode current determines the applicable HV for the PMT. The MOLLER experiment will

use 9305QKB PMTs manufactured by ET Enterprises [17]. Although these PMTs have a maximum anode current rating of 100 $\mu A$, it is planned to operate well below this limit (around 10$\mu A$) to ensure both longevity and long-term gain stability [15].

### 1.4.2 PMT Base

A PMT requires a voltage divider (Appendix A provides the schematic of the 3-stage voltage divider [15].) to properly distribute the HV among the dynodes, which accelerates the electrons, and signal processing electronics primarily to amplify and convert the small current signal produced by the PMT into a measurable voltage signal for the DAQ. Depending on the application, the signal processing electronics may also include pulse shaping and/or discriminator circuitry to modify the signal into desired form. Typically, all these components are attached to the back of the PMT and are collectively referred to as the PMT base.

Figure 1.10 shows the proposed design of the PMT base for the MOLLER apparatus. It consists of a voltage divider, pulse mode and current mode preamplifiers, output filters, and gain selectors. The PMT base requires two power inputs: ±10 VDC input to power the preamplifiers, and high voltage supply for the PMT operations. To suppress common-mode noise, the entire signal chain is fully differential [15]. This means that the PMT signals are transmitted via two separate lines, with one signal being the inverse of the other. At the readout, the two signals are combined by taking the difference, which cancels out noise common to both lines due to their inverse nature.

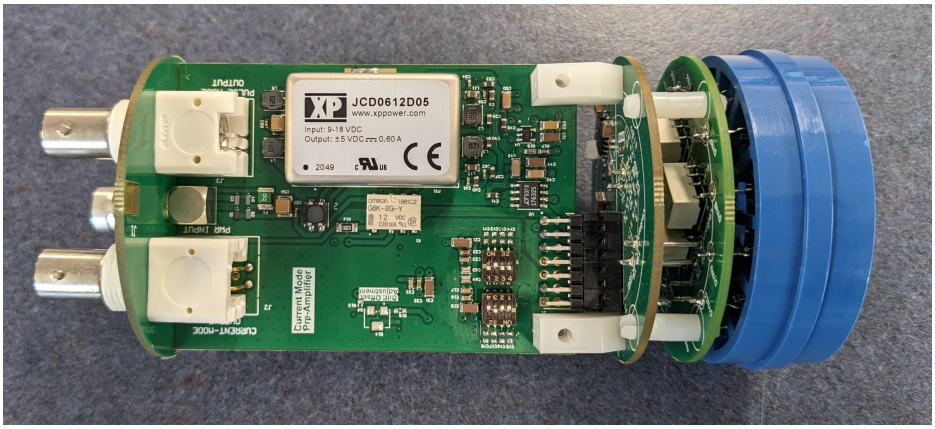


Figure 1.10: PMT base which contains current and pulse mode preamplifiers, and a voltage divider.

The PMT base is designed so that during operations the gain of the PMT and

the operation mode (pulse or current mode) can be selected remotely by changing polarity of the DC power supply [15].

9305QKB PMTs contain 10 dynodes staged for electron multiplication. However, to improve stability and linearity of the PMTs in the MOLLER experiment, only the first few dynodes were utilized by the voltage divider in the PMT base [15]. The rest of the dynodes are tied to the anode and kept grounded. There are two base configurations, 3-stage and 4-stage which utilized first 3 and 4 dynode stages respectively. A simplified schematic of the 3-stage base is shown in Figure 1.11.

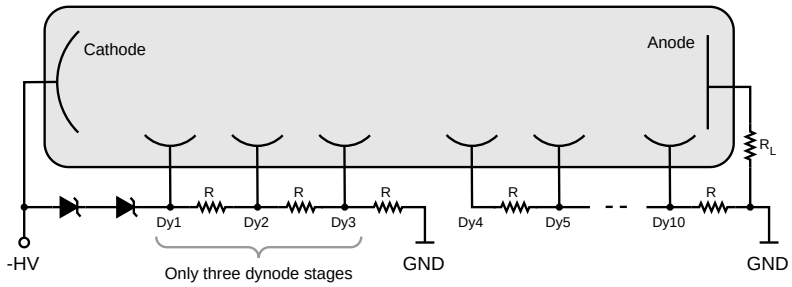


Figure 1.11: Simplified voltage divider schematic in the 3-stage base. Only the first three dynodes were utilized for electron multiplication. The complete schematic of the 3-stage divider is provided in Appendix A.

## 1.5 Methods of Measuring PMT Non-Linearity

A PMT is considered to have non-linear characteristics when its output is not proportional to its input. Non-linear behavior in PMTs typically arises when the input light level is too high compared to the manufacturer's recommended operating range [16]. When a large amount of charges flows through a region, such as near the dynodes, the charge cloud (space charges) can disrupt the flow of subsequent charges, leading non-linear behavior of in the PMT [16, 18].

The MOLLER $A_{\mathrm{PV}}$ measurement relies on PMTs operating in integration mode, where the signal output is proportional to the incident electron flux. To achieve the proposed precision of the MOLLER experiment, the integrated detector asymmetry $\langle A \rangle$ need additional corrections before it is used as the parity violating analyzing power of the Møller scattering, $A_{\mathrm{PV}}$. Equation 1.6 describes these corrections [15].

$$A_{\mathrm{PV}} \propto \left( \langle A \rangle - A_F - A_{\mathrm{lin}} - \sum_i f_i^{\mathrm{bkgd}} A_i^{\mathrm{bkgd}} \right) \tag{1.6}$$

$f_i^{\mathrm{bkgd}}$, the relative background signal size, and its asymmetry $A_i^{\mathrm{bkgd}}$ are used to correct for elastic and inelastic nuclear scattering events, where $i$ denotes the specific background process. $A_F$ accounts for the asymmetries in the measurements that are not covered by other corrections. The precision goal of MOLLER requires the non-linearity of the PMTs to be $\leq 0.5\%$ and measure it to an precision of 0.1% [15].

Various methods for measuring PMT non-linearity are documented in the literature, with the choice of method depending on the specific use case for the PMT. A method of measuring non-linearity in current mode involves using a light source with a PMT to measure the current output and check if it is proportional to the light input. However, this method requires calibrations to know the changes in light level beforehand [19]. Another method provided by Hamamatsu [16] involves using an aperture with four separate shutters placed after the light source. By measuring the PMT currents as $q_1, q_2, q_3, q_4$ with each shutter opened individually, and then measuring the current with all four shutter open to obtain $q_0$, one can calculate the linearity using the Equation 1.7 [16]. A derivation of this method which uses 2 LEDs is implemented in studies [20–22].

$$\text{Non-Linearity} = \left( \frac{q_0}{q_1 + q_2 + q_3 + q_4} - 1 \right) \times 100\% \tag{1.7}$$

A popular method for measuring non-linearity in pulse mode involves using two pulsing light sources, typically LEDs. There are several variations of this approach. Hamamatsu [16] recommends using two pulsing LEDs with different brightness levels and compare the recorded ratio between the two pulse heights ($r_1$) while varying the distance to the LEDs from the PMT. If $r_2$ is the pulse height ratio at a closer distance, the non-linearity can be expressed as Equation 1.8 [16].

$$\text{Non-Linearity} = \left( \frac{r_2 - r_1}{r_1} \right) \times 100\% \tag{1.8}$$

Since the ratio is defined at the light source, any discrepancies between two locations should be attributed to the non-linear response of the PMT. The method has been employed in studies [23, 24] to test PMTs for non-linearities. This approach is particularly suitable for PMTs with smaller windows, as it can introduce systematic biases for large and/or spherical photocathodes due to non-uniform surface illuminations at short distances [25]. Instead of moving the light sources, Longhitano [26] used

a laser system with an attenuator and a fiber optic delayer to measure non-linearity through the same analysis.

The PMT non-linearity measurements conducted in the study [27] also utilized two pulsing LEDs, but the methodology differed. One LED is a bright while the other is dim. Considering $f(x)$ as the integrated PMT response for a bright LED flash $x$, and $f(\delta)$ for a dim LED flash $\delta$. The non-linearity of the PMT is assessed using $f(x+\delta) - f(x)$ as a function of $x$. In simpler terms, if the PMT were linear, the integrated response to a smaller light pulse should be the same regardless of the background light level. Hence, $f(x+\delta) - f(x)$ should remain constant [27].

The following Table 1.3 summarizes the non-linearity thresholds of the discussed studies and their measurement precision.

Table 1.3: Non-linearity measurement summary of previous studies with the non-linearity requirement for MOLLER.

| **Study** | **PMT operation** | **Threshold target (%)** |
|---|---|---|
| Yin et al. [19] | Pulse mode | – |
| Lv et al. [20] | | 5 |
| Barnhill et al. [21] | | 6 |
| Wu et al. [22] | | 10 |
| Zhang et al. [23] | | 5 |
| Yu et al. [24] | | 5 |
| Wang et al. [25] | | 5 |
| Longhitano et al. [26] | | 5 |
| Friend et al. [27] | | 1 |
| PREX-2 & CREX [28] | Integration mode | 0.3 |
| MOLLER (this study) [15] | | 0.5±0.1 |

### PMT Non-Linearity Measurement for MOLLER

In the context of the MOLLER experiment, PMT non-linearity is defined as the variations measured by the PMT for a fixed asymmetry due to changes in the overall signal amplitude [15]. This approach replicates the light conditions of the MOLLER experiment and quantifies the non-linearity of the asymmetry measurement itself. A similar method for measuring non-linearity has been employed in previous $A_{\mathrm{PV}}$ experiments, PREX-2 and CREX [28].

To measure the PMT non-linearity for the MOLLER experiment, it is crucial to develop a method that accurately replicates the light signals the PMTs will encounter in the actual experiment. The following chapters will explore the design considerations

for this method, the construction of the experimental setup, the processes for data collection and data storage for numerous MOLLER PMTs, and the subsequent data analysis. Finally, the results will be presented.

# Chapter 2

# Experimental Setup

The goal of this study is to precisely measure the non-linearity of the numerous PMTs that are going to be placed inside the MOLLER main integrating detector. This measurement aims to parameterize the non-linearity of individual PMTs under light conditions, cathode currents, and anode currents similar to those of the actual MOLLER experiment.

An apparatus was built to characterize the non-linearity of PMTs, based on a similar approach taken by [29], which was developed to test PMTs used in the previous asymmetry-measuring experiments PREX-2 and CREX.

## 2.1 Apparatus Design Requirements

During the MOLLER measurement, it is expected that the wavelengths of most of the photons generated from the quartz crystals will lie in the ultraviolet (UV) region (see Figure 1.8b) [15]. Therefore, a PMT sensitive to the UV region of the electromagnetic spectrum was selected (9305QKB PMT), which has a spectral range of 295 - 630 nm [17]. Due to this constraint, the light sources employed to measure the PMT non-linearity in this study used 400 nm LEDs.

Since the goal is to measure the non-linearity of the PMT readout as a function of signal amplitude, a method was required to generate light signals similar to ones observed by a PMT in the MOLLER experiment. Figure 2.1 illustrates the expected time dependence of the current mode PMT readout during the MOLLER parity violating measurement. Parity-violating scattering means that there is a difference between the cross-sections of scattering right-handed and left-handed electrons from the target [7]. Therefore, the scattered electron intensity changes between the two helicity states. Since the generated Cherenkov photon flux in the quartz tiles is

proportional to the electron intensity, the PMT readout follows the same trend.

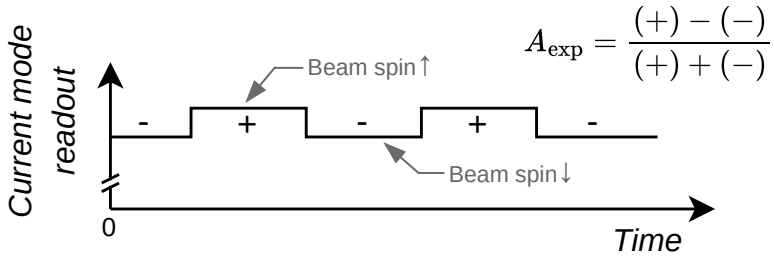


Figure 2.1: Expected current mode PMT readout during the MOLLER measurement. Depending on the helicity of the electron beam, the PMT readout changes due to the parity violation at the target. The helicity reversal rate of MOLLER is 1920 Hz [15].

To replicate the PMT readout signal shown in Figure 2.1 which represent the helicity reversal of the MOLLER electron beam, this study uses two UV LEDs and an optical chopper wheel. To simulate the variations in electron beam intensities in the actual MOLLER experiment, a filter wheel with Neutral Density (ND) filters was used.

Even if the electron beam operates at different currents, the expected asymmetry value should not change as it is independent of intensity. Therefore, this study assesses how the PMT response affects the asymmetry measurement due to variations in overall signal amplitude. To accurately quantify the systematic uncertainties of the MOLLER experiment necessitates precise knowledge of the PMT behavior. This study provides a controlled environment to characterize the non-linear behavior of this component prior to the main experiment. Table 2.1 outlines the methods and equipment employed to replicate the MOLLER conditions in the lab apparatus.

Table 2.1: Methods used in the lab apparatus that replicate components of the MOLLER experiment.

| | **MOLLER Experiment** | **Lab Setup** |
|---|---|---|
| Beam intensity | Beam current | ND filter wheel |
| Helicity reversal | Controlled by the accelerator | Optical chopper wheel |
| True asymmetry | Determined by nature | Brightness of two UV LEDs |

As defined in Equation 2.1, the LED asymmetry (true asymmetry) is set by adjusting the voltages of the LEDs, and the overall light intensity is then varied using the filter wheel with its ND filters. If the PMT measures the same LED asymmetry over the intensity range of interest, it is considered linear in the context of the

MOLLER experiment. Any non-linearities need to be measured precisely to minimize the uncertainty of the final MOLLER measurement.

Another major requirement is setting the maximum LED light intensities correctly to match the conditions of the MOLLER experiment. Based on simulations conducted by the MOLLER collaboration and physical beam tests using quartz tiles, it has been estimated that the maximum cathode current the PMT would produce in the experiment is around 20 nA [15]. Additionally, it was proposed that the anode currents of the PMTs should stay well below the maximum level of 100 $\mu$A [17] during MOLLER operations ($\sim$ 10 $\mu$A) for longevity and stability reasons discussed earlier in Section 1.4.1.

Apart from these considerations, one key aspect taken into account during the construction of the test apparatus was automation. Since the test setup needs to measure the non-linearity of all 300 PMTs ordered for the MOLLER experiment, the apparatus required a high level of automation to complete the tests with minimal intervention, ensuring they are repeatable and reliable. Results shown later in Section 5.1 provide more details about the stability of this apparatus.

## 2.2 Apparatus Construction

The apparatus prepared for this study uses two dark boxes connected via fiber optic cables. All the major components used in the setup are shown in Figure 2.2. The dark box that houses the two LEDs contains an optical chopper apparatus, which is used to generate a flashing light output from a continuous light source. The light signals generated by LED 1 and the chopper apparatus are coupled to separate optical fibers and carried over to the dark box 2 where the PMT is located. In the second dark box, several components modify and measure the incoming light. The optical signals first pass through a filter wheel and a diffuser, which attenuate and diffuse the incoming light, and are then measured by the PMT and a temperature controlled photodiode. The photodiode readout serves as an independent light intensity measurement alongside the PMT.

One of the custom-designed 16-channel analog-to-digital converter (ADC) boards made specifically for the MOLLER experiment was used to perform the photodiode and PMT readout. After the signals were digitized, they were communicated to the data acquisition computer (DAQ-PC) over an Ethernet connection for further analysis. As the ADC board, and all other digital equipment, such as the direct current (DC) power supply, optical chopper controller, and filter wheel, are connected

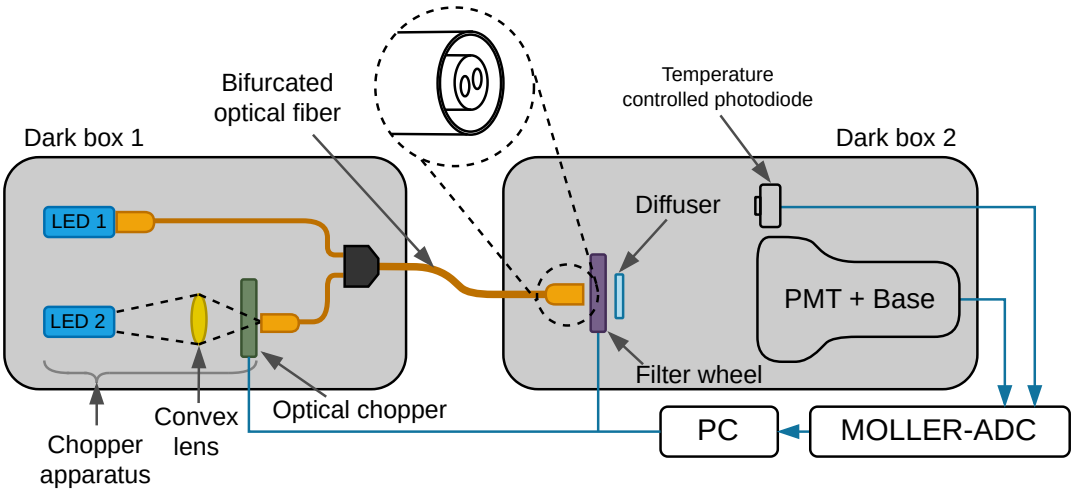


Figure 2.2: Block diagram of main components of the experimental setup.

to the DAQ-PC and controlled through a custom-made automation script that was made accessible in the repository [30]. The functions of this automation process are discussed in later Chapters 3, and 4.

### 2.2.1 Dark Box 1: Preparing Input Light Signals

Two 400 nm LEDs were used in this apparatus to generate a combined light signal similar to what the PMT would encounter in the actual MOLLER experiment. LED 1 is brighter than LED 2. This brightness difference is achieved by selecting appropriate current-limiting resistors: LED 1 is paired with a 100 Ω resistor, while LED 2 is paired with a 4.7 kΩ resistor. This combination ensures that the expected LED asymmetry at the PMT (using Equation 2.1) is maintained between 2–3% when the LEDs are at the same voltage. The expected $A_{\mathrm{PV}}$ at MOLLER is ≈33 ppb [7] which is not practical to achieve with LEDs using the current apparatus. Therefore, a reasonable value of 2–3% was chosen. The LEDs are powered by two separate channels of a BK PRECISION 9129B 3-channel DC power supply.

#### Optical Chopper Apparatus

The dim LED (LED 2) with the chopper wheel is used to produce a flashing signal which then produced the required light signal (Figure 2.1) when combined with the constant bright LED light. Instead of electrically flashing the LED, which could introduce errors due to the non-linear characteristics of LEDs, the chopper wheel is used to produce a flashing light output from the continuously lit dim LED. The

optical chopper system used in this study is Thorlabs' MC2000B optical chopper system with an MC1F30 chopper blade.

The Computer-Aided Design (CAD) diagram of the optical chopper apparatus is shown in Figure 2.3. It consists of several components to produce a flashing output from the continuously lit dim LED.

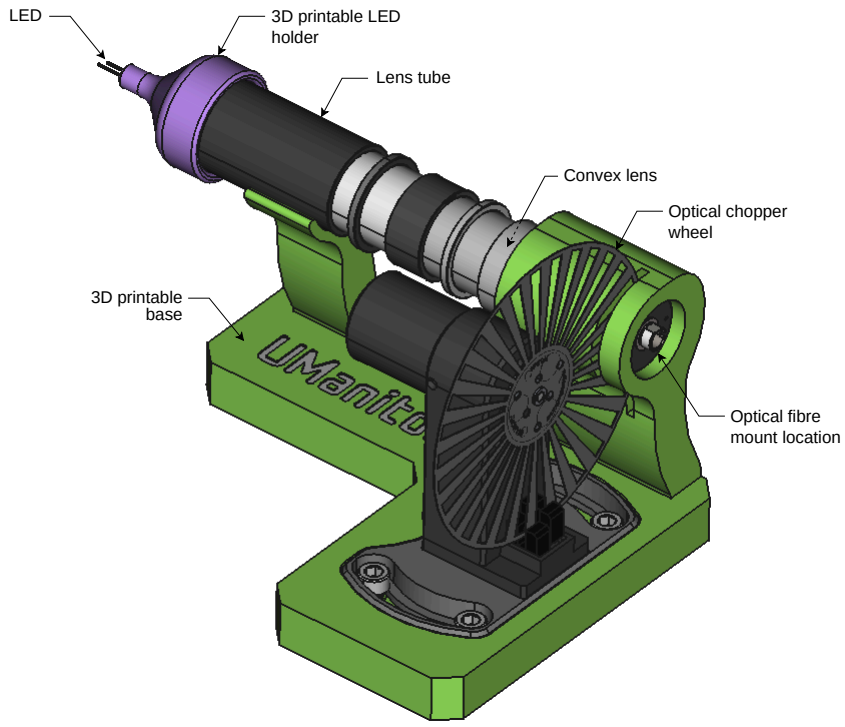


Figure 2.3: CAD design of the optical chopper apparatus used to generate flashing light output from a constant LED light source.

The LED is mounted to the back of the lens tube, which has two bi-convex lenses with 50 mm focal lengths at the other end to focus the gathered light into the 400 $\mu$m optical fiber opening. Before the light enters the fiber, the chopper wheel intercepts the beam and chops it to generate the desired flashing frequency set by the chopper controller. The width of the chopper blade openings is equal to the blade width, resulting in a flashing output with a duty cycle of 50%. The base (green) of the chopper apparatus and the LED holders (purple) were 3D printed. With the help of another 3D-printed adapter, light of the bright LED is coupled into the remaining fiber cable by placing it as close to the LED as possible for maximum light collection. Figure 2.4 (b) shows the completed build of the chopper wheel apparatus with the bright LED mount.

The chopper wheel is connected to the chopper wheel controller, which sits outside

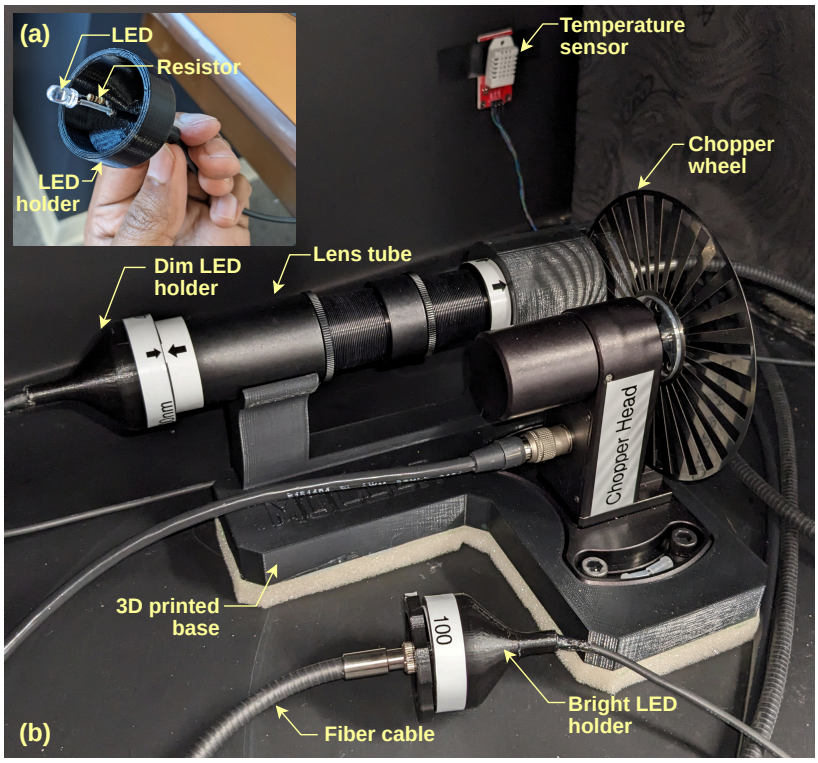


Figure 2.4: (a) An LED attached to the holder (LED is pushed outward otherwise usually sits at the back of the holder), (b) Complete chopper wheel apparatus.

the dark box and provides power and control signals to the wheel. The two LEDs are directly connected to the 3-channel DC power supply, which is also placed outside the dark box. Figure 2.9 shows all the external controllers. The power supply controls the voltage and subsequently adjusts the brightness of the LEDs when necessary. Both the chopper controller and the power supply are connected to the DAQ-PC over separate Universal Serial Bus (USB) interfaces, and two separate Python scripts [30] were developed to communicate with the devices through the *serial* protocol.

The non-linearity testing apparatus frequently leveraged 3D printing for mounting components together and proved to be an invaluable asset when building experimental setups. All the 3D-printed parts were made from Poly-lactic Acid (PLA) in black to ensure light tightness and reduce reflections. After assembling all the optical parts, markers (black arrows on white labels) were placed on both sides of every mounting surface as shown in Figure 2.4 to realign components if for any reason it is necessary to disassemble the components.

### Combined Light Signal

When the intensities of the two light signals are combined, they produce a signal similar to a square wave, as shown in Figure 2.5. However, unlike a square wave that could be observed if the LED were flashed electrically, the signal here does not have instantaneous rising and falling edges. Instead, it takes some time to transition from one state to the other. This delay occurs due to the physical nature of covering and uncovering the light source to produce a flashing output.

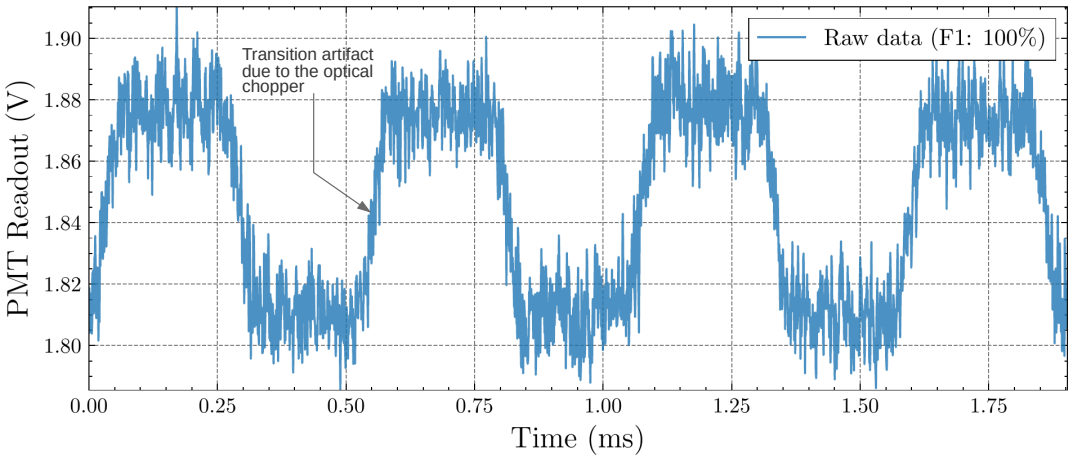


Figure 2.5: PMT readout due to combined LED light signals used to replicate the light levels in the MOLLER experiment.

This changing light level simulates the helicity reversal of the electron beam that give rise to the parity violation. The frequency of the chopper wheel is set to match the helicity flipping rate of the MOLLER experiment which is 1920 Hz [15]. Throughout the rest of the document, the light intensity level '$H$' (high) refers to the combined light level of both the constant and flashing LEDs. The light intensity of only the bright, constant LED is referred to as the intensity level '$L$' (low). With these definitions in place, the measured LED asymmetry ($A_{\text{LED}}$) can be expressed for a high-low pair as

$$A_{\text{LED}} = \left(\frac{H - L}{H + L}\right) \tag{2.1}$$

## 2.2.2 Dark Box 2: Measuring Light Signal

Light signals from the first dark box are fed to the second dark box, where the PMT is located, through a bifurcated optical fiber. Although the two fiber cables are bundled together within a single wrapped cable, they remain separate in a bifurcated optical

fiber, as shown in Figure 2.2. A bifurcated optical fiber was specifically chosen to facilitate the simultaneous transmission of both light signals into the filter wheel. The arrangement of the components in the second dark box is shown in Figure 2.6 which contains the filter wheel, PMT with its base, temperature-controlled photodiode, and a temperature sensor.

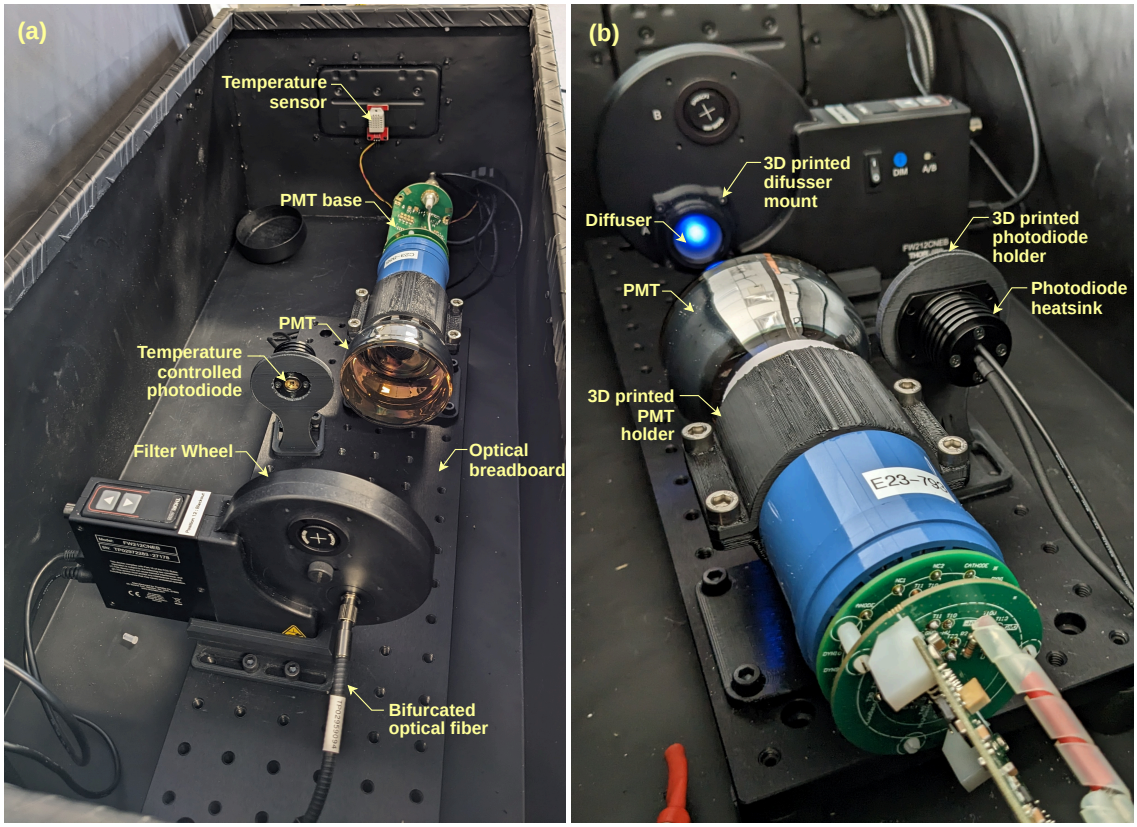


Figure 2.6: Separate side views of the components in the second dark box including PMT with its base, filter wheel, photodiode, and temperature sensor.

The filter wheel, the PMT, and the photodiode are mounted on an optical aluminum breadboard to achieve alignment of components with relative ease. The parts were attached to the breadboard using 3D-printed holders. To create these mounts, all the individual components were designed in a CAD software (3D files for some parts, such as the filter wheel and optical breadboard, were available on the manufacturer's website) and aligned with each other inside the 3D environment. The mounts were then designed around each part to hold them securely. Since better alignment of optical components leads to improved optical performance by reducing light losses and focusing issues, assembling all the parts beforehand in a 3D environment allowed for finer adjustments to their relative positions while accounting for 3D printing tolerances. Some 3D-printed parts, such as the base of the chopper wheel apparatus that

aligns the LED light with the fiber optic cable, had to be designed in incremental steps because precise focusing of the light on the fiber opening is crucial for optimal light transmission.

### Filter Wheel

The filter wheel used for this study is the FW212CNEB 12-position motorized filter wheel from Thorlabs. The light from the fiber cable first passes through the filter wheel, which contains 12 ND filters. The transmission rates of these filters are listed in the Table 2.2 [31].

Table 2.2: Transmission rates of neutral density filters.

| **Filter** | 1 | 2 | 3 | 4 | 5 | 6 | 7 | 8 | 9 | 10 | 11 | 12 |
|---|---|---|---|---|---|---|---|---|---|---|---|---|
| **Transmission (%)** | 100 | 79 | 63 | 50 | 40 | 32 | 25 | 10 | 5 | 1 | 0.1 | 0.01 |

Individual filters were rearranged pseudo-randomly to avoid systematic errors that might occur if the light level always increased or decreased as the filter rotates. An internal view of the filter wheel with the rearranged filter positions is shown in Figure 2.7. I t was found that all 12 positions of the filter wheel could not be used for the non-linearity measurement, as the later filters which have lower than 5% transmission rates did not have sufficient light throughput for measurable LED asymmetry. Therefore, data from only the first 9 brightest filter positions were selected for further analysis, and the 12$^{\text{th}}$ position was repurposed as the blackout position to block all light coming from the fiber.

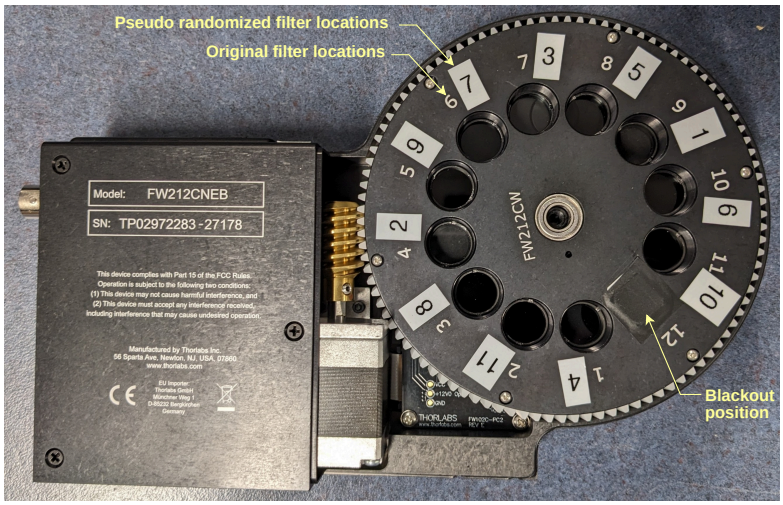


Figure 2.7: Randomized filter locations inside the motorized filter wheel.

The filter wheel was also connected to the DAQ-PC via a USB connection, and the position of the filter aligned with the light coming out of the fiber was controlled by another Python script that is available in the Git repository [30].

When the filtered light signals exit from the other side of the filter wheel, they pass through a diffuser so that, instead of producing a bright spot, the light spreads out and covers the photocathode of the PMT evenly. This minimized the spatially non-uniform photocathode response.

### 2.2.3 Signal Chain

A high-level overview of the signal chain is shown in Figure 2.8. The cathode current of the PMT was measured using a *unitary gain base* connected to a picoammeter, which is illustrated in Figure 2.8(a). The unitary gain base is a specially designed component used to measure the current flow between the photocathode and the first dynode of the PMT. The procedure for measuring the maximum cathode current is discussed in Section 3.1.1.

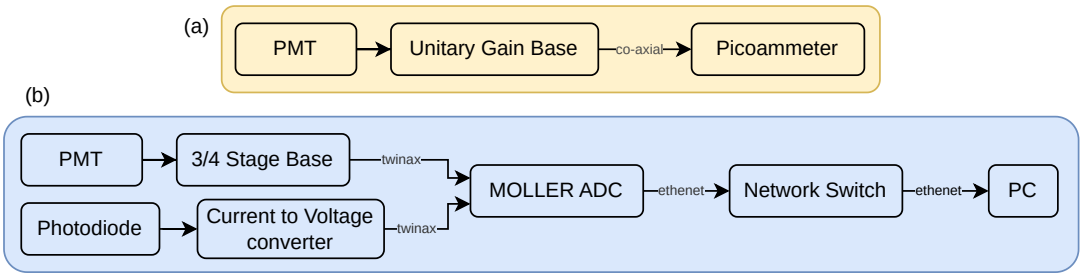


Figure 2.8: A high-level overview of (a): PMT cathode current and (b): PMT anode current measuring signal chains.

The current mode output of the PMT is dual-ended (differential) to reject common-mode noise. The differential signals from the PMT base output port are then transmitted to the ADC board via a twin-axial (twinax) cable for digitization. To operate the PMT in current mode, the PMT base requires a +10 VDC input and a high voltage (HV) supply (HV value changes depending on the PMT and base stages used.). The +10 VDC input powers the preamplifier circuitry in the PMT base and is connected to one of the outputs of the 3-channel DC power supply. The high voltage required for the operation of the PMT dynodes is supplied by a dedicated HV power supply (CANBERRA 3002D).

The photodiode used in this study is the UV-sensitive Hamamatsu S2592-03 thermoelectrically cooled silicon photodiode. It is equipped with a heat sink, a thermo-

electric cooler, and a thermistor to monitor and maintain a constant temperature via the C1103-04 temperature controller, which is located outside the dark box (see Figure 2.9). The output of the photodiode is a current signal that varies proportionally with the incident light. However, the ADC readout board requires voltage inputs; therefore, the current signals from the photodiode are converted and amplified through a Hamamatsu C9051-01 current-to-voltage conversion amplifier. Although the ADC board is designed to accept only differential signals through its twinax BNC inputs, the single-ended output of the photodiode was made compatible with the ADC board using a custom-made cable that converts the single-ended output to dual-ended by shorting one of the signal lines to ground.

### 2.2.4 Final Design Considerations

#### Cable Routing

When routing cables into and out of the dark boxes, it was done without compromising light tightness. If a routing hole in a box was only going to be used once, it was sealed off after routing the necessary cables. When a routing hole had to be left open for further access during prototyping, an 'S'-shaped 3D-printed cable guide was attached to the hole to prevent outside light from entering the dark box while allowing for easy routing of new cables when necessary. Finally, the dark box was covered with a blackout sheet for additional isolation, as shown in Figure 2.9.

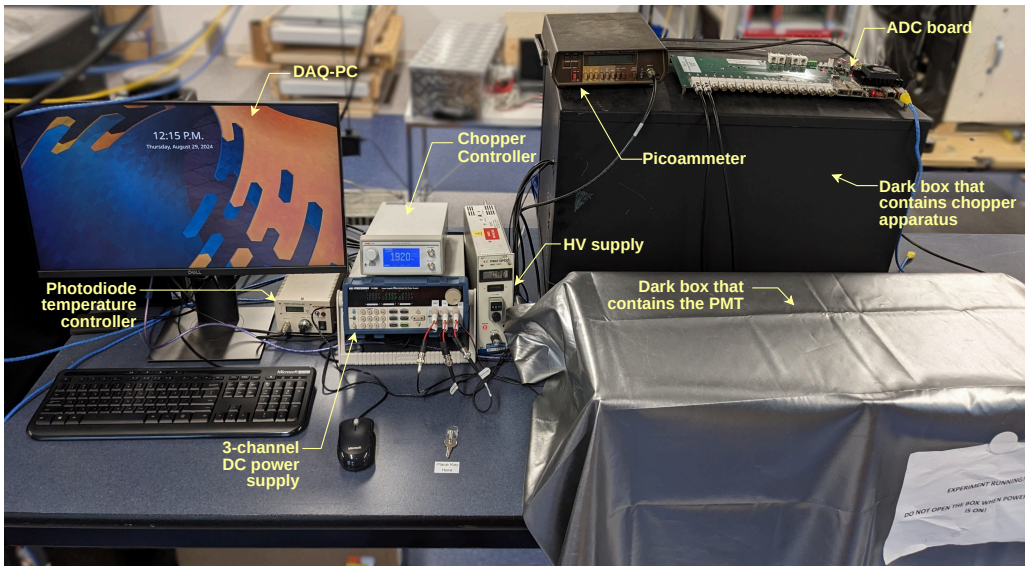


Figure 2.9: Complete bench top PMT non-linearity test apparatus.

### Temperature Measurement

To measure the temperature inside both dark boxes, a temperature sensor (DHT22) was placed in each box. The readings from these sensors were collected by an Arduino microcontroller board connected to the DAQ-PC. The board reads the sensors every 10 seconds and temporarily holds the data in its serial buffer. A Python script [30] was developed to read the buffer whenever a measurement was needed.

### Automation

A Linux kernel base operating system was chosen for the DAQ-PC as it is generally easier to automate file handling tasks using 'bash scripting', a programming language generally used in unix-like system. A bash script [30] was written in the end to combine all the Python communication programs developed separately to talk with different components of the apparatus, and to handle the data management.

### Grounding

As the apparatus contains many sensitive digital components, it was crucial to keep every component that uses electricity at the same reference voltage level (same ground) to avoid unwanted noise pickup and DC offset issues. During the prototyping stage, it was observed that without proper grounding, the apparatus was especially susceptible to 60 Hz noise from alternating current (AC) power lines. This issue was resolved by connecting the metal dark box enclosing the PMT to the same ground potential as the rest of the equipment. Furthermore, all critical electrical and signal wiring of the apparatus was done using coaxial or twisted-pair cables to further reduce noise pickup.

### Summary

The ultimate goal of this test apparatus is to produce light signals that a PMT is expected to measure in the MOLLER experiment and to provide a mechanism for adjusting the overall light amplitude to measure PMT non-linearity. A summary of major test parameters used for the PMT non-linearity measurements are tabulated in table 2.3.

With all the discussed components in place and the A sample acquisition window is shown in Figure 3.5, the apparatus has achieved this goal. The next chapter will discuss how the non-linearity measurement is performed and how the apparatus leveraged automation.

Table 2.3: Summary of the apparatus parameters.

| **Parameter** | **Value** |
|---|---|
| Maximum cathode current (nA) | 20 |
| Maximum anode current ($\mu$A) | 10 |
| PMT base preamplifier impedance (k$\Omega$) | 200 |
| PMT warm up time (h) | 2 |
| PMT HV range (–V) | 550 - 950 |
| LED wavelength (nm) | 400 |
| True LED asymmetry (%) | $\sim$2 |
| Optical chopper frequencies$^{\dagger}$ (Hz) | 960, 1920 |
| ADC sampling rate (samples/s) | 14,705,883 |
| ADC down sampling factor | 10 |
| Data acquisition period per filter (s) | 0.5 |
| Total measurement time (s) | $\sim$112 |
| Temperature sensor resolution ($^{o}$C) | 0.1 |
| Photodiode temperature ($^{o}$C) | 20 |

$^{\dagger}$ Two frequencies are analyzed with 'quartet' and 'pairwise' methods respectively (see chapter 3)

# Chapter 3

# Data Collection

The main goal of the data collection stage is recording PMT signals and relevant test parameters from various components of the apparatus and store it in the DAQ-PC to calculate the non-linearity of the PMT.

Apart from the main LED asymmetry data extracted from the PMT through the ADC, there are several other data sources to keep track of during each test, such as the temperature of the dark box, the voltages and currents used for the LEDs and PMT base, the maximum PMT anode and cathode currents, etc. All the recorded test parameters are listed in the Table 2.3. Data from most of these sources are extracted digitally via an automation program, but some parameters, such as the PMT cathode current, were recorded manually.

Multiple custom Python scripts were prepared to control and gather data from the digital equipment such as the filter wheel, optical chopper, DC power supply, and temperature sensors. A bash script then controls all the individual Python programs as a whole to perform the measurement. This automation program also accommodates the collection of manually obtained data.

The data collection process can be separated into three main sections: *Pre-tests*, *data acquisition*, and *post-tests*. Preparing all the equipment for data collection is done during the pre-tests. Next, all the data necessary for the non-linearity analysis is recorded during the data acquisition step and stored in the DAQ-PC. Finally, the post-tests involve checking for any potential data losses, unusable data, or corrupted data. Figure 3.1 shows the flow of the data collection process.

If all these repetitive tests were to be done manually for each PMT, it would require a lot of error-prone manual labor and would be highly inefficient. Instead, this study automates each step of the data collection process where possible.

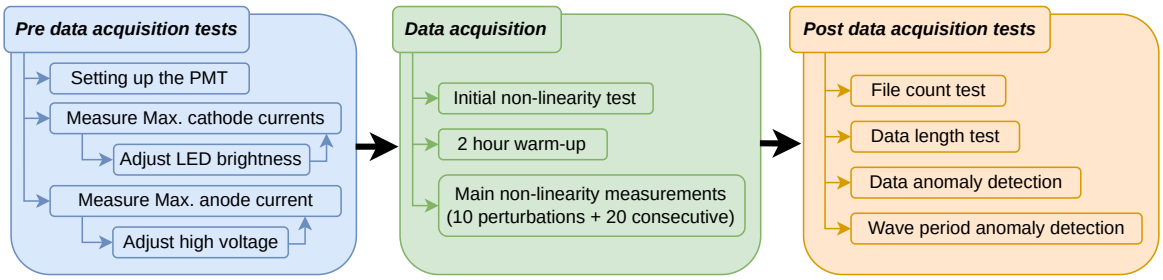


Figure 3.1: Breakdown of major stages in the data collection process.

## 3.1 Pre Data Acquisition Tests

There are multiple checks that need to be completed prior to performing a non-linearity measurement. These checks serve as a set of fail-safes to collect consistent, quality data during each PMT test. Some of these checks are performed manually, but most are written into the automation script [30], which has made the whole process more efficient.

The manual work includes setting up a PMT for measurement (as shown in Figure 3.1), collecting data from the high-voltage power supply, and measuring the maximum cathode currents using a picoammeter (KEITHLEY 485) because the equipment does not provide digital outputs that can be connected to the DAQ-PC.

After setting up the PMT in the dark box and before starting a non-linearity measurement comprises multiple steps. To ensure all critical steps are followed when preparing the apparatus and to gather the manually collected data, a comprehensive checklist was created and is included in Appendix C.

### 3.1.1 Maximum Cathode Current Measurement

Simulations and beam tests conducted by the MOLLER collaboration estimate that the mean maximum cathode current experienced by a PMT in the MOLLER detector is approximately 20 nA [15]. To replicate the MOLLER conditions, the LED brightness must be adjusted so that, at maximum brightness during the non-linearity test, the PMT's cathode current does not exceed 20 nA. Furthermore, measuring the maximum cathode current at different brightness levels allowed the PMTs to be tested multiple times under varying light conditions.

The maximum cathode current data collection process is entirely manual and streamlined through the use of the checklist provided in Appendix C. At the beginning of a test, the whole apparatus was powered down, and a PMT was taken out from the lot and mounted on the PMT holder in the dark box while ensuring that the distance

from the front of the PMT to the filter wheel was 14 cm. Then, a *unitary-gain* base was connected to the PMT to measure the maximum cathode current. The unitary gain base is a specially designed base in which only the first dynode of the PMT is utilized. There are no zener diodes to regulate the voltage between the photocathode and the first dynode, as in regular 3 (see Figure 1.11) or 4-stage bases. Instead, when using the unitary gain base, the HV supply was set to –280 V to match the voltage drop of the regular base. Then, the filter wheel was set to the fully open position (100% transmission), and the voltage of the constant bright LED was varied while recording the voltage values when the cathode current reads 7, 9, 12, 15, and 18 nA. Figure 3.2 shows the LED voltages used to achieve these cathode currents. A range of voltages is used to achieve each cathode current level, indicating variations in the photocathode sensitivity to light (quantum efficiency) among the PMTs.

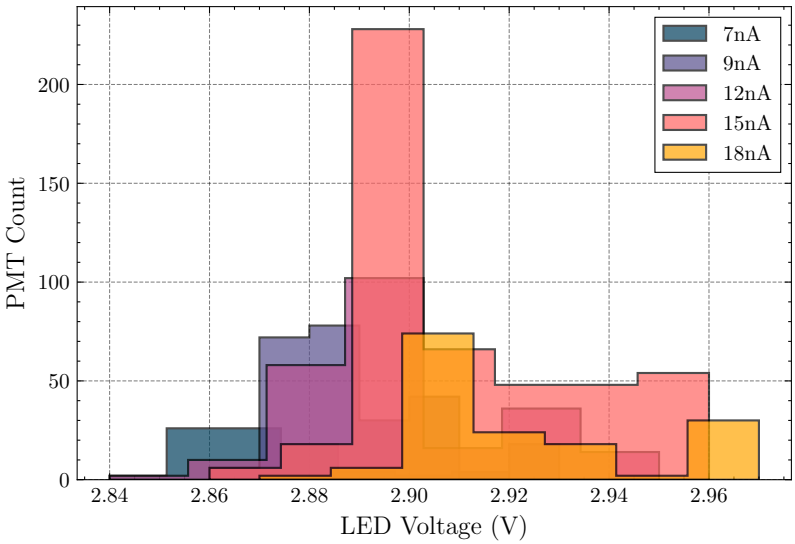


Figure 3.2: Distribution of LED voltages used to achieve various cathode current outputs from the tested PMTs. Higher voltages result in a brighter LED.

These LED voltage values are later used in the main data acquisition for the asymmetry measurement. Lower cathode currents of 7, 9, and 12 nA are used for PMTs tested with the 4-stage base, as it has an additional amplification stage that results in higher gain and therefore requires lower light levels to avoid high anode currents. The 12, 15, and 18 nA maximum cathode currents are used with the 3-stage base. Fixing the LED voltage at the desired cathode current using the 100% transmission filter ensures that the limit is not exceeded during filter rotations.

### 3.1.2 Maximum Anode Current Measurement

After recording the voltages associated with maximum cathode currents in the checklist, the 3-stage base was installed with the PMT while keeping the distance to the filter wheel, 14 cm, the same during installation.

To enhance the longevity and improve the non-linearity of PMTs [15], it was proposed to set the maximum anode current below 10 $\mu$A. To facilitate this, an initial measurement of the maximum anode current was taken at the brightest filter position (100% transmission) using the recorded LED voltage value associated with 15 nA cathode current (with already installed 3-stage base at the end of the max cathode current measurement). The HV was manually set to –800 V.

The maximum anode current measurement was taken by recording 0.5 s of a continuous stream of voltage values from the current mode output of the PMT via the ADC board. Additionally, to apply a pedestal correction (adjust the DC offset), another stream of values was recorded at the blackout position ($12^{\text{th}}$ filter position). The maximum anode current, $I_{\text{anodeMax}}$, can then be calculated using Equation 3.1, where $V_{\text{max}}$ is the mean voltage at the 100% transmission filter, $V_{\text{pedestal}}$ is the mean voltage at the blackout filter position, and $g$ is the preamplifier impedance.

$$I_{\text{anodeMax}} = \frac{V_{\text{max}} - V_{\text{pedestal}}}{g} \tag{3.1}$$

The impedance of the preamplifier in the PMT base is set by a dip switch on the circuit board of the base and can be set to values of 20, 100, 200, and 1000 k$\Omega$. The impedance was set to 200 k$\Omega$ for all the measurements, as it provides the most suitable amplification without saturating the ADC at the required cathode and anode current ranges.

Since this study focuses on anode currents less than 10 $\mu$A, it was decided that the $I_{\text{anodeMax}}$ for every PMT tested should be in the range of 8–10 $\mu$A. If the calculated anode current did not fall between the range of 8–10 $\mu$A, the high voltage was adjusted accordingly, and the anode current measurement was repeated until it satisfied this condition. Since the maximum anode current was set before the warm-up period, it experienced a drift during the 2-hour warm-up. Figure 3.3 illustrates the distribution of the maximum anode current for all tested PMTs after the warm-up period.

Due to manufacturing tolerances, the gain values of the PMTs were found to vary during the prototyping stage. Therefore, some PMTs could not satisfy the above-mentioned 8–10 $\mu$A maximum anode current condition even with high voltages up to –950 V. A 4-stage base, utilizing the first four dynodes, is used with PMTs that

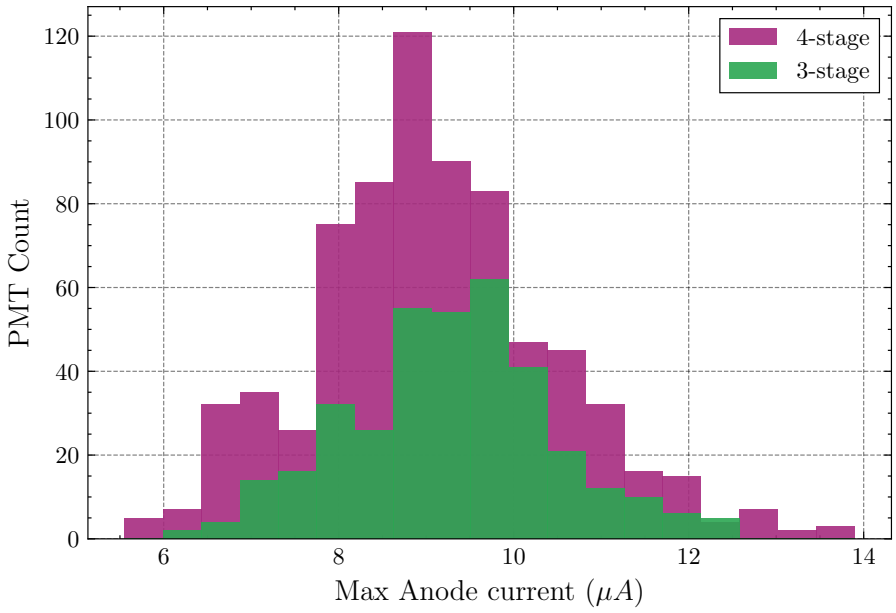


Figure 3.3: The distribution of maximum anode currents after the 2-hour warm-up period.

exhibit low-gain responses. If the maximum anode current could not be brought into the desired range by increasing the high voltage, the measurement continued with the 4-stage base. When changing the high voltage with either base, it was done so that it did not exceed the absolute maximum rating of the PMT or the maximum allowed voltage between dynodes, whichever came first.

After switching to the 4-stage base if necessary and reaching the desired maximum anode current, this marked the end of the pre data acquisition tests.

## 3.2 Automation Program

To make the data collection more efficient and consistent, an automation program [30] was developed as a command-line tool. After initiation, the automation program will take care of setting up all the test conditions and data recording, storage and analysis.

Initiation of the program requires several test parameters that are gathered manually with the checklist, such as the PMT serial number, the number of stages in the employed PMT base, the LED voltages for maximum cathode currents, and the supplied HV.

The following command-line output shown in Listing 3.1 displays the help prompt of the automation script '`record.sh`' with an example use case.

```
1 $./record.sh --help
```

```
-------------------------------------------------
|  MOLLER PMT Non-Linearity Measurement : Usage  |
-------------------------------------------------
Code by: Anuradha Gunawardhana
Date: 03.06.2024
Version: 0.4

Options:
-s,   --serial        PMT serial number
-v7,  --VLEDat7nA     LED voltage at 7nA cathode current (@-b=4)
-v9,  --VLEDat9nA     LED voltage at 9nA cathode current (@-b=4)
-v12, --VLEDat12nA    LED voltage at 12nA cathode current
-v15, --VLEDat15nA    LED voltage at 15nA cathode current (@-b=3)
-v18  --VLEDat18nA    LED voltage at 18nA cathode current (@-b=3)
-b,   --base          [Optional] Number of stages in the base (3,4)(default=3)
-on   --overnight     [Optional] set overnight wait time during runs (min=2)
-hv,  --highVolt      [Optional] High voltage readout (0-1000)(default=-800V)V
-g,   --gain          [Optional] Base preamp gain (20k, 100k, 200k, 1M)(default=200k)
-ts,  --timeStamp     [Optional] Time stamp of PMT powerd on time (YYYYMMDDhhmm)

Usage:
./record.sh -s C23-888 -b 3 -v12 2.87 -v15 2.88 -v18 2.90 -hv 800
```

Listing 3.1: Automation script usage

When the program is executed with the required initial parameters, first, it helps the user with the maximum anode current test that was discussed earlier by sending commands to the 3-channel DC power supply to set the PMT and bright LED voltages (`-v9` or `-v15` values are used depending on the information about the connected base). It then communicates with the filter wheel to rotate it to the desired positions (0% and 100% transmission filters) and records PMT data through the ADC. The helper program used to communicate with the ADC board over Ethernet was written by Dr.Gericke [32] for the MOLLER collaboration.

Depending on the measured maximum anode current, the user will be prompted to either adjust the high voltage, or the program will begin the next phase, 'Data Acquisition'. Beyond this point, the apparatus does not require any further input from the user.

The modular nature of the developed automation program allows for the validation of commands at each stage of information exchange between scripts. If a user accidentally enters an incorrect value for a critical parameter, such as the voltage of the LEDs, it is immediately detected before being passed to the power supply control script, which interacts directly with the 3-channel DC power supply. This also applies to all other inputs from the user. Each input to the automation script is re-checked to ensure it is within the acceptable range before being passed on to the next stage.

Even when the DC supply control script is used as a standalone program during

prototyping, it contains the necessary fail-safes to prevent damage, such as catching incorrect inputs, setting voltage and current limits at the hardware level, and monitoring current draw. It will immediately shut off power if any anomalies are detected.

Since multiple pieces of equipment in the apparatus need to operate in parallel to perform tests, not only were critical fail-safes implemented, but numerous small checks were also added throughout the data chain to identify anomalous behavior. For example, whenever the program set a parameter of an equipment (eg: position of the filter wheel) remotely, it was reconfirmed through another request to the device. The automation program also performs the data quality checks discussed in Section 3.5.

Having these fail-safes and checks facilitated easier troubleshooting during the prototyping stage and, more importantly, they act as indicators of a successful measurement.

## 3.3 Data Acquisition

The second stage of the data collection process involves recording the required data for the non-linearity analysis. After the pre-tests mentioned in the previous section are completed without any errors, the automation script will perform an initial test non-linearity measurement and its analysis to ensure all components are functioning as intended. At this point, the user can review the generated analysis plots (see Chapter 4 for more details) and any messages produced by the automation program for issues, as the program will check for and report any anomalies it finds during the analysis (Section 3.5).

The PMT is then allowed to warm up for two hours. This warm-up period is crucial because the pedestal (mean of the PMT integration mode output voltage recorded without any light) of the PMT drifts for a short time after the PMT is powered on. Therefore, the final measurements must wait until the PMT has stabilized. During the prototyping stage, it was identified that a PMT with the base electronics generally requires about two hours to stabilize after being powered on. This pedestal drift is shown in Figure 3.4.

After the 2-hour warm-up period, the automation script begins the main data collection, which measures the non-linearity of the PMT under test. This measurement involves several steps. First, the voltage of the LEDs is set by the automation script according to the initialization parameters. The chopper wheel to set its frequency to

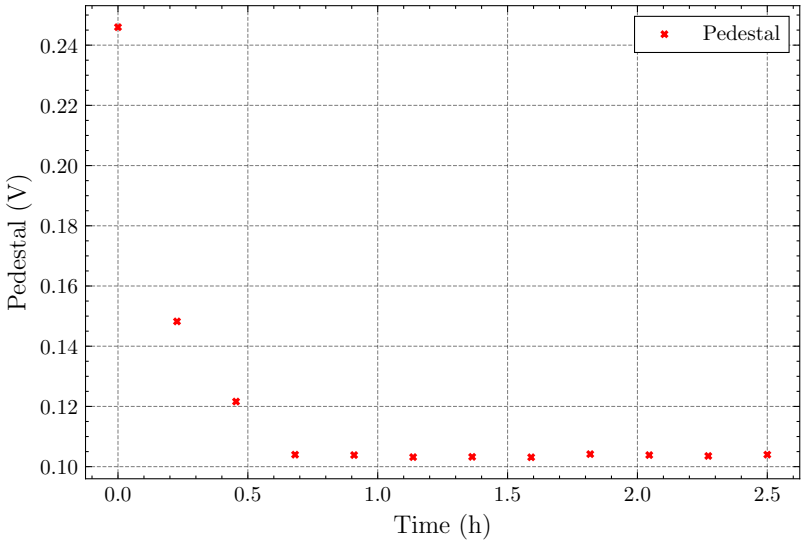


Figure 3.4: Typical PMT pedestal variations over 2.5 hours after being turned on.

1920 Hz. Then, the filter wheel is rotated starting from the blackout position. At each filter position, 0.5 seconds of data is recorded through the ADC board. A final record is taken from the blackout position to measure the pedestal drift.

Figure 3.5 illustrates the raw data recorded from the PMT as it goes through each filter in the filter wheel. Although each record contains data for 0.5 seconds, the plot shows only approximately 2% of the total length. The figure shows the effect of light attenuation caused by passing through the ND filters. As the transmission rate of the filter decreases, both the mean amplitude of the signal and the flashing amplitude are reduced.

The automation script allows for multiple measurements with small perturbations to the test conditions. This is primarily achieved by varying the LED voltages during each run. The LED voltages, initially recorded during the maximum cathode current measurement, are provided to the automation program using `-v7` to `-v18` inputs, depending on the connected base. The program performs 5 separate non-linearity runs with these voltages, as detailed in Table 3.1.

The voltage perturbations shown here are used for non-linearity runs performed with the 3-stage base. The combinations used for the 4-stage base follow a similar pattern[1]. The first three runs use the same voltages for both LEDs, which maintains the LED asymmetry as it was set by the current limiting resistors. However, this changes the maximum cathode currents for each run. These runs are used to assess

[1]Most of the flashing LED voltage values had to be reduced by ∼0.03 V to keep the asymmetry within the acceptable 2% range.

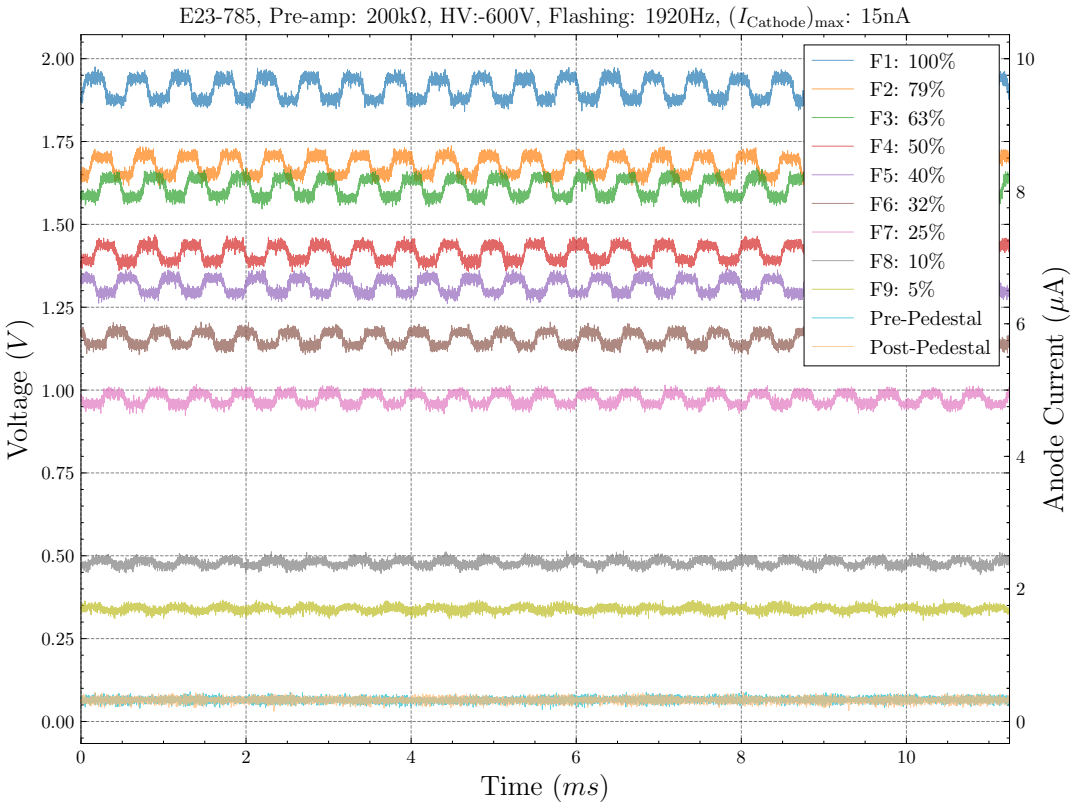


Figure 3.5: Sample raw PMT data necessary for the non-linearity calculation which were recorded via the ADC by going through the filter positions. The light signal contains both the bright constant and flashing LEDs which is then attenuated by the ND filters. Only 2% of the full 500 ms length is plotted.

non-linearity at different maximum cathode currents as shown in Figures 5.19 and 5.20. Runs 2, 4, and 5 keep the bright LED at a constant voltage while varying the flashing LED voltage, which changes the measured LED asymmetry between these runs. These LED perturbations allow for studying the variations in non-linearity due to changes in asymmetry.

To allow the recorded data to be analyzed using these two methods, another set of 5 non-linearity runs (using Table 3.1 perturbations) were recorded with an LED flashing frequency of 960 Hz. The analysis of the non-linearity measurement was performed using two separate methods called *pairwise* and *quartet*, which relate to the helicity reversal pattern of the MOLLER experiment. More details about these analyses are discussed later in Section 4.2. Thus, a total of 10 separate non-linearity runs were performed with each PMT.

Additionally, to assess the systematic uncertainty of a non-linearity measurement, 20 consecutive non-linearity runs were performed. This test also demonstrates the

Table 3.1: Combinations of LED voltage inputs used to perform multiple non-linearity runs that uses a 3-stage base.

| **Run** | **Bright LED voltage value at max cathode current (nA)** | **Flashing LED voltage at max cathode current (nA)** |
|---|---|---|
| 1 | 12 | 12 |
| 2 | 15 | 15 |
| 3 | 18 | 18 |
| 4 | 15 | 15 - 0.02 V |
| 5 | 15 | 15 + 0.02 V |

repeatability of the measurement (see Section **??**).

As shown in Figure 3.5, even when all light is blocked by the blackout filter, a pedestal (DC offset) remains that must be corrected before calculating non-linearity. Since one non-linearity measurement takes around 2 minutes to complete, this study takes two measurements: one at the beginning and another at the end of each non-linearity run to account for any pedestal drift during the 2-minute measurement window. Although this offset could be adjusted at the hardware level using the provided potentiometer on the PMT base, it was found to be unreliable because the offset value tends to differ from PMT to PMT. Therefore, the pedestal was subtracted at the analysis (see Section 4.1).

### 3.3.1 Other Data Recorded

In addition to the raw voltage values recorded through the ADC, several other pieces of information were collected from various sources during each non-linearity run. Following Table 3.2 describes all the collected data from different sources.

All of these listed parameters are recorded during the operation of the automation script. Some parameters are collected from the inputs to the automation script, while others, such as chopper frequency and preamp gain, are hard-coded into the script (though they can be changed if needed). Since the values of most of these parameters change between non-linearity runs, this study keeps track of all parameters listed in Table 3.2 during each non-linearity run.

At this stage, the study collects data from at least 30 non-linearity runs per PMT, including the 20 consecutive runs discussed earlier. Each non-linearity run consists of 13 data files recorded during ND filter rotations and two text files containing values of all the extra parameters listed in the Table 3.2. The next section will discuss how

Table 3.2: List of all the recorded parameters during a non-linearity measurement of a PMT.

| **Parameter** | **Collection method** |
|---|---|
| Utilized PMT base (3 or 4-stage)<br>PMT Serial number<br>PMT high voltage (V) | Manual inputs to the automation script when initializing. |
| Temperature of each dark box ($^o$C)<br>Constant LED (mA)<br>PMT base current (mA) | Measured from external sensors and equipment through the automation script. |
| Chopper Frequency (Hz)<br>Constant LED (V)<br>Flashing LED (V)<br>Preamp gain (impedance) (k$\Omega$)<br>Maximum cathode current (nA) | Values are selected by the automation script by default or based on inputs. |
| PMT power on time (Time stamp)<br>Total run time (s) | Generated by the automation script. |
| ADC prescale factor<br>Record time per filter (s) | Collected from the ADC configuration file. |

these files are managed and stored on the DAQ-PC.

## 3.4 Data Management and Storage

Since there are numerous PMTs to test and each PMT produces a large amount of data, a robust data management and storage method was needed. During each non-linearity run, the automation program goes through each filter in the filter wheel and records the voltage signals from the PMT through the ADC board. These data are stored in ROOT files, a file format developed by CERN that can handle large-scale data efficiently [33]. In this case, the ADC generates one ROOT file per ND filter.

Apart from the ADC data, several other data sources need to be tracked during non-linearity runs, as listed in the Table 3.2. The automation script communicates with different equipment to gather the required parameters and generates a text file called `Experiment_data.txt` to store the collected data. Each non-linearity run will get unique data file. This file includes all the extra parameters needed for the analysis, except for the initialization data used for the ADC. The ADC requires a configuration

file called `CMDataSettings.txt` to initialize its functions. Among other settings, this file contains the period during which the ADC should record data and the prescale factor used to down sample the ADC data rate. Therefore, during each non-linearity run, this configuration file is also copied.

Each recorded data file (ROOT file) from the ADC at each filter rotation is renamed according to the corresponding filter position and then saved in the DAQ-PC using the directory structure shown in Figure 3.6.

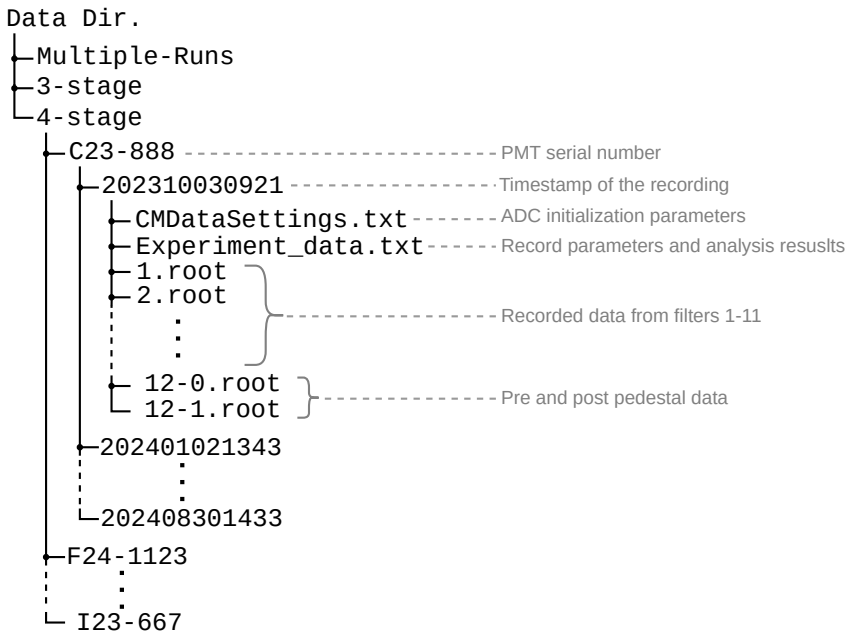


Figure 3.6: The directory structure of the stored data in the DAQ-PC. *Multiple-Runs* and *3-stage* directories have the same structure as the expanded view of the *4-stage* directory.

The base directory where all recorded data is stored is divided into three subdirectories: *Multiple-Runs*, *3-stage*, and *4-stage*. The 20 consecutive non-linearity runs collected from the PMTs are recorded in the *Multiple-Runs* directory, while the remaining runs performed with various perturbations are saved in either the *3-stage* or *4-stage* directory, depending on the PMT base used. All three subdirectories follow the same structure. Each PMT has its own separate directory, and every non-linearity measurement performed with the same PMT gets a unique folder named after the timestamp of the initiation. For example, if a non-linearity run was to be performed at 1:30 PM on 2024/Sep/23 using the PMT with the serial number 'A24-1292' attached to the 3-stage base, the automation script will create a folder 'A24-1292' (if there is no existing one) inside the '3-stage' and copy all the generated ROOT files and text files into a unique folder inside the PMT directory named '202409231330'.

This naming conversion and the data text files allowed streamlining the creation of a final database that contains all the necessary analysis data for handover to the MOLLER collaboration. The process of generating this database is discussed in the next chapter.

With a 0.5-second recording period per filter, each non-linearity run generates approximately 60 megabytes (MB) of data files. If the data from the 20 consecutive non-linearity runs are excluded, it is expected that the 10 perturbed non-linearity runs alone will generate around 200 gigabytes (GB) of data from all the 300 PMTs.

## 3.5 Post Data Acquisition Tests

At the completion of each non-linearity run, the automation script will perform the non-linearity analysis using a dedicated Python script [30], which processes all the data stored in the run directory named with the initiation timestamp. The main purpose of performing the data analysis is to verify the data integrity.

Before moving on to the next non-linearity measurement, it is crucial to check whether all the necessary files are in place for the analysis and to ensure there are no anomalies in the data. To achieve this, the analysis script is equipped with several data check functionalities. Specifically, the analysis script will perform the following four data integrity tests:

1. File count check
2. Data length test
3. Data anomaly detection
4. Wave period anomaly detection

The file count check ensures that the non-linearity run being analyzed contains all the required files necessary for the analysis. This check not only counts the total number of files but also reads the names of each data file to identify if any files are missing.

The data length check, which applies only to the ADC data, counts the number of data points in each saved ROOT file and verifies that none of them contain fewer data points than a preset *data limit* value. This value is dynamically calculated using Equation 3.2, based on the record period per filter (T), ADC sampling rate (R), and the prescale (down-sampling factor) (p) values.

$$\text{Data limit} = \frac{RT}{p} \times 90\% \tag{3.2}$$

With this data limit, the length test ensures that at least 90% of the expected number of data points is present for the analysis and there are no large data losses. Based on the record period and prescale value used for the final production apparatus, the data limit is calculated to be 661,764 data points per filter. Furthermore, since the data limit is not hard-coded, it allows integrity checks for data recorded with various record periods and prescale factors. Having a dynamically changing data limit was highly advantageous during the prototyping stage, as several combinations of record periods and prescale values were tested before settling on the final configuration.

The next check tests whether the recorded data contain any outliers. Due to various reasons such as external EM noise, temperature, vibrations, etc., some data points could randomly produce spikes in the data stream. This test is detecting these voltage spikes using the mean ($\mu_{\text{data}}$) and standard deviation ($\sigma_{\text{data}}$) of the data. If the distance of any data point ($x$) from the mean is larger than three standard deviations ($|\mu_{\text{data}} - x| \geq 3\sigma_{\text{data}}$), it is considered an outlier. The size of $3\sigma_{\text{data}}$ relative to the standard deviation is shown in Figure 3.7. Since these spikes are random, they cannot be completely avoided. Therefore, only the ROOT files that contain fewer than 1% outliers compared to its full record length are considered suitable for analysis. Every ROOT file must pass this test for the run to be deemed acceptable for analysis.

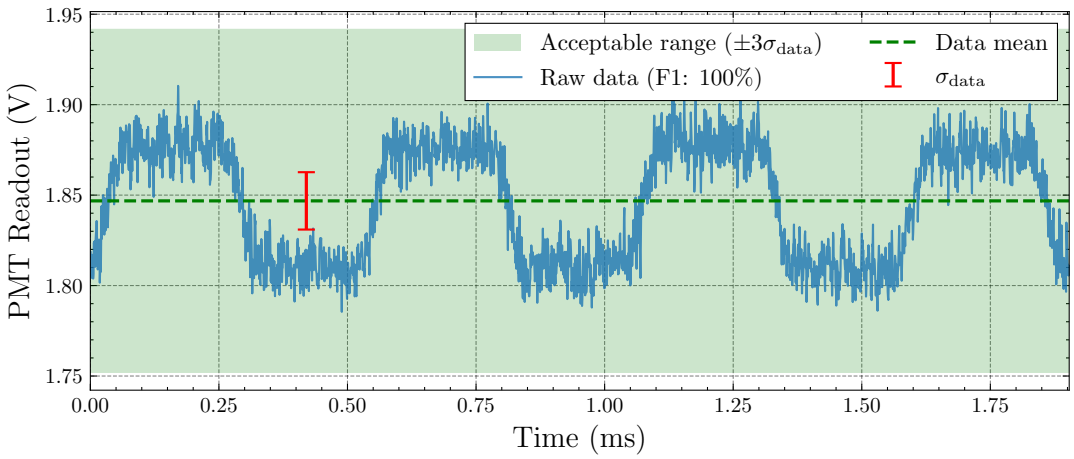


Figure 3.7: A data point is considered an outlier if it is more than 3 standard deviations ($3\sigma$) away from the data mean.

As shown in Figure 3.5, the recorded raw data from each filter exhibit a periodic waveform (a square wave). The final check assesses the deviations of each cycle period

($t$) from the mean of all the periods ($\mu_{\text{periods}}$) in that particular record. Similar to the previous method, if any cycle deviates by more than three standard deviations ($|\mu_{\text{periods}} - t| \geq 3\sigma_{\text{periods}}$), it is considered an anomaly, and the non-linearity run containing that record is deemed unsuitable for analysis. The method for calculating the period of each cycle is discussed in detail in Section 4.3.

Every non-linearity run must pass all four tests for the analysis to proceed and produce a non-linearity value for the tested PMT. Chapter 4 will detail the calculation of individual PMT non-linearity values.

# Chapter 4

# Analysis

This chapter discusses how the non-linearity calculation is performed using data collected from a PMT. The complete analysis is implemented in a Python script [30], allowing it to be automatically deployed after each PMT data collection. To increase the efficiency of the calculation, the data is first loaded and organized into matrices [34]. This step is referred to as the preprocessing stage. Subsequently, the LED asymmetry ($A_{\mathrm{LED}}$) is calculated for each filter position using the preprocessed data. Finally, the PMT non-linearity is determined.

## 4.1 Preprocessing

The collected data (ROOT files) from the filter positions are first loaded into the analysis and stored as matrices, as calculations on large datasets can be performed more efficiently by leveraging the combination of matrices and the parallel computing capabilities of modern CPUs (Central Processing Units). All the matrices are then trimmed to a fixed length. Trimming the ends of each data series is necessary due to minor irregularities in the number of points in each data file.

The process of checking the data for the minimum length was discussed at the end of the previous chapter (Section 3.5). Following a similar procedure and using the data limit equation 3.2, the matrices were trimmed to 90% of the expected points by taking into account the ADC sampling rate and the prescale value. After trimming, 661,764 data points (0.45s) per filter position were available for analysis.

The next step in the preprocessing stage is the *pedestal correction*. During data collection, two records were taken with the blackout filter position; one at the beginning of the data collection (pre-pedestal) and the other after completing all the filter rotations (post-pedestal). The histogram in Figure 4.1 illustrates an example of pre

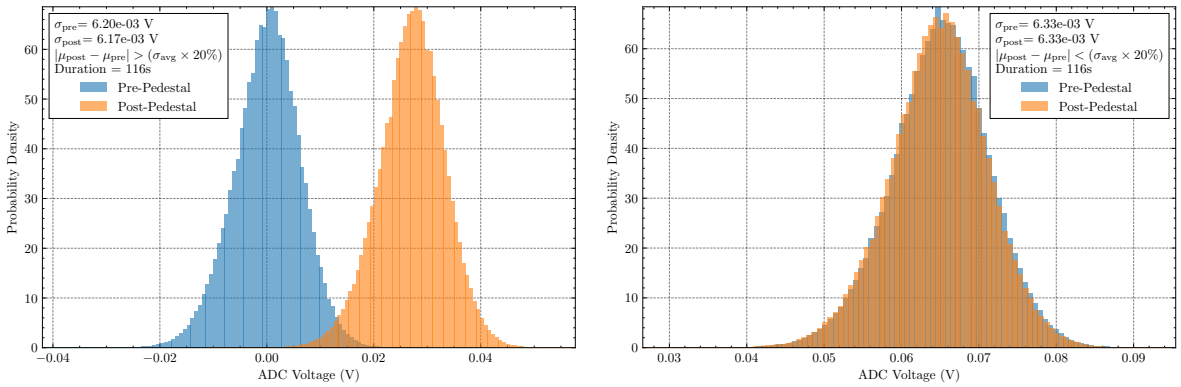


(a) (b)

Figure 4.1: The two pedestal runs recorded in the beginning and at the end of a non-linearity measurement (a) without warming up the PMT and (b) after a 2h warm-up.

and post pedestal runs.

The mean value of the initial pedestal run ($\mu_{\text{pre}}$) provides information about the overall pedestal (DC offset) of the measurement. The difference between the means of the two pedestal runs ($|\mu_{\text{post}} - \mu_{\text{pre}}|$) represents the *pedestal drift*. Since these pedestal runs were collected after warming up the PMT for 2 hours, the pedestal drift is significantly reduced. In this case, the measured pedestal drift is minor compared to the average standard deviation ($< \sigma_{\text{avg}} \times 20\%$) of the two pedestal runs.

Before proceeding with the main non-linearity calculation, the data must be corrected to account for the overall pedestal and any drifts. If no pedestal drift occurred, the correction would be as simple as subtracting the overall pedestal from all the data points. However, since the non-linearity measurement takes around 2 minutes to complete, minor pedestal variations during that period must be corrected. Equation 4.1 shows the correction applied to each original data point $x_o$ to generate the corrected data point $x$.

$$x = x_o - \left( \frac{\mu_{\text{pre}} + \mu_{\text{post}}}{2} \right) \tag{4.1}$$

Here, $\mu_{\text{pre}}$ and $\mu_{\text{post}}$ represent the mean values of the initial and final pedestal runs, respectively. This method corrects for the overall pedestal while minimizing the effects of any pedestal drift that may have occurred during data collection.

## 4.2 Data Selection for Asymmetry Calculation

After the preprocessing stage, the data is ready for the asymmetry calculation. The MOLLER experiment will measure the asymmetry using several helicity reversal patterns to perform electron beam-related corrections [15]. This study replicates two of these patterns, known as the *pairwise* and *quartet*, to perform the analysis by carefully selecting relevant data through a data selection window. Figure 4.2 illustrates the difference in how the data selection window is applied for the two methods on a signal similar to the recorded data from a filter position.

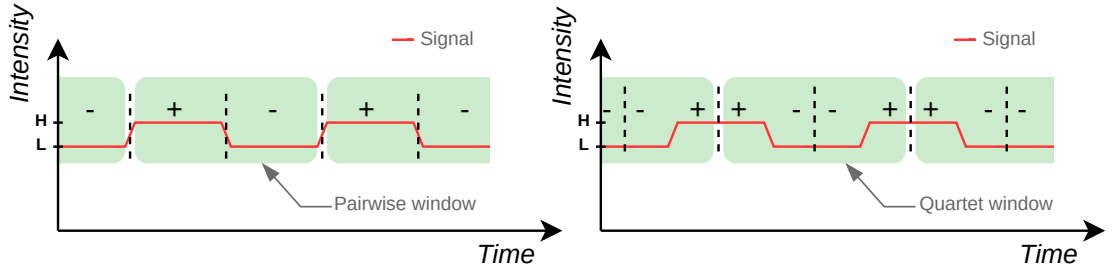


Figure 4.2: The usage of data selection window for the *pairwise* and *quartet* analysis methods.

The size of the data selection window is set to be equivalent to the period of the signal, ensuring that it always selects one cycle's worth of data. The first step in calculating the LED asymmetry is to average all the [+] data points as $H$ and all selected [–] data points as $L$ for each data selection window. Then, using Equation 2.1, the LED asymmetry ($A_{\text{LED}}$) is calculated for each window. The final LED asymmetry for a filter position is determined by the mean value of all the individual $A_{\text{LED}}$ calculated for that particular filter.

The most challenging part of this analysis is accurately placing these selection windows on the recorded data without any reference clock signal that synchronized with the data to detect rising and falling edges.

Since the apparatus uses a chopper wheel instead of an electrical switching system to generate flashing light signals, implementing a system that synchronizes to an external clock signal would be complicated and require significantly more time, effort, and equipment. Therefore, this study adopts a software-based analysis approach, which only requires the signal and some additional parameters, as shown in Table 2.3, recorded during data collection.

## 4.3 Sobel Filtering

This study employs a technique inspired by the Sobel method [35] to dynamically identify locations of the rising and falling edges of the signal. Sobel method is often used in image processing applications to detect and emphasize edges of objects in a 2D image [36]. This is accomplished by convolving a kernel (a square matrix) on the image. However, this method cannot be directly applied to this study, as the time-series data it collects is only one-dimension. Therefore, the 2D kernel was modified into a column matrix containing only one dimension, which was then convolved with the time-series data. Equation 4.2 describes a 1D convolution operator [37].

Take $\mathbf{x} = [x_1, x_2, \cdots, x_n]^T$ as the input data matrix and $\mathbf{y} = [y_1, y_2, \cdots, y_m]^T$ as the kernel, where $n > m$. The output of the one-dimensional convolution operation $\mathbf{z} = [z_1, z_2, \cdots, z_{n-m}]^T$ can then be written as;

$$z_{(i+1)} = \sum_{k=1}^{m} x_{(i+k)} \cdot y_{(k)}; \quad \text{for } i = 0, 1, \cdots, n-m \tag{4.2}$$

The elements in the kernel can be constructed in various ways to detect, emphasize or filter out different features in the data. When detecting sharp changes in data, such as edges in an image, the kernel often contains a zero crossing feature [35]. For example, the first half of the kernel ($\mathbf{g}$) chosen for this study, as shown in Equation 4.3, is filled with +1s and the later half is filled with −1s. As one moves from the beginning of the kernel to the end, data points crosses zero exactly once.

$$\mathbf{g} = [+1, +1, \cdots, +1, +1, -1, -1, \cdots, -1, -1] \tag{4.3}$$

This zero crossing feature in the kernel emphasizes sharp changes in data when convolved. However, before performing the convolution operation, the size of the kernel needs to be determined to obtain the desired output. Therefore, the kernel length was set to be equivalent to half of the signal period. Instead of hard-coding the kernel size in the analysis script, this study chose to dynamically set the size according to the chopper frequency. The Sobel kernel size (s) is calculated using the Equation 4.4.

$$s = \frac{1}{2}\frac{R}{p\nu} \tag{4.4}$$

Where $R$ is the sampling rate of the ADC board, $p$ is the prescale factor used for the down-sampling, and $\nu$ is the frequency of the chopper wheel, which determines

the LED flashing rate. Since all these parameters are collected during each run and saved with the ROOT files, the analysis has easy access to them. The length, being dependent on the experimental parameters, allows for easier prototyping, as the analysis adapts to changes in every test condition.

The Sobel filtering process is somewhat similar to discrete differentiation. However, testing reveals that the Sobel method is more suitable for this use case rather than differentiation to identify edges in data. Figure 4.3 shows an example raw signal recorded through the first filter position (100% transmission) and the output of the Sobel filtering process.

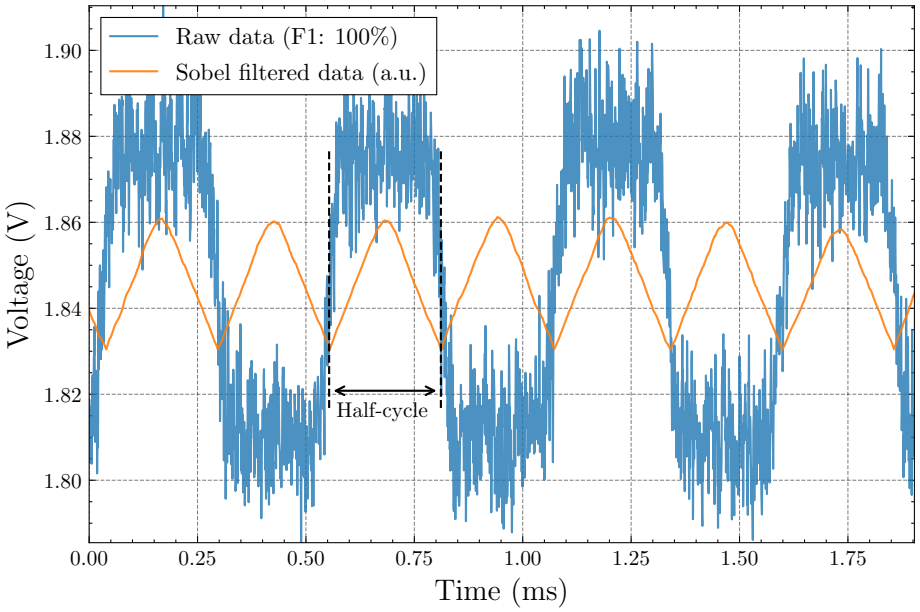


Figure 4.3: Raw data recorded from the fully open (100% transmission) filter position is plotted (only ∼0.5% of the full length is plotted) with the sobel filtered output (arbitrary unit).

Since the selected Sobel kernel size is deliberately set to half the period (half-cycle), the filtered output resembles a triangular wave, with each peak positioned roughly in the middle of each half-cycle of the raw signal. The peaks of this filtered output allow for the identification of the midpoints of every high and low light levels.

Using each midpoint, only a portion of data were selected by excluding the data points corresponding to high-low transition. This was achieved by selecting only 60% of the data points from the middle of each half cycle. Figure 4.4 shows the selected data points for two cycles of raw data recorded from the first (100% transmission) and last (5% transmission) filter positions.

Using this method to filter out unwanted data points proved to be extremely

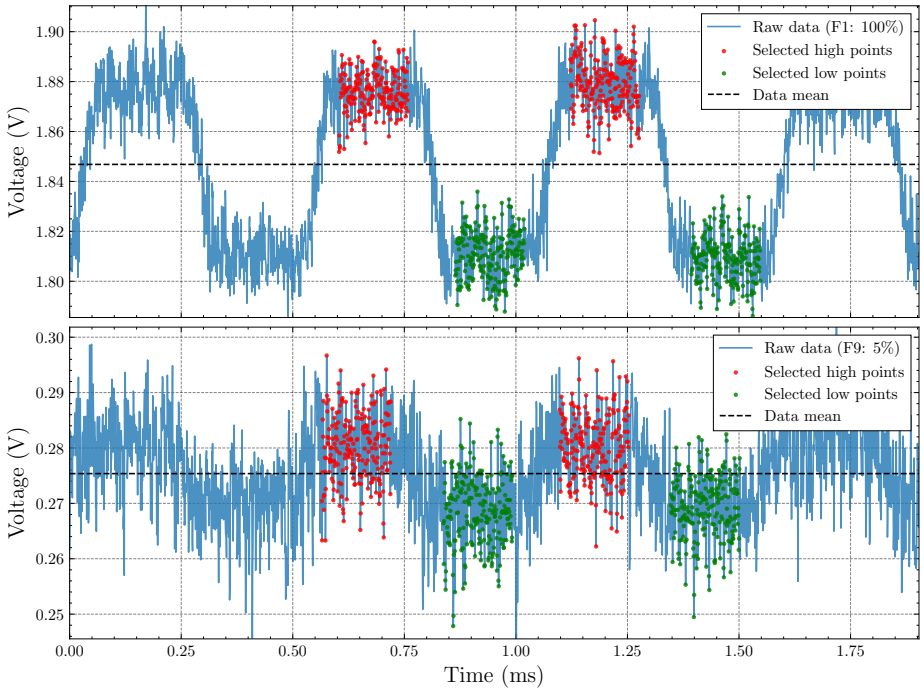


Figure 4.4: Raw data from 100% and 5% transmission filter positions plotted with the selected data for the analysis. Only ∼0.5% of the full data length and two data selection cycles are shown for each data series. 60% of the data from a middle of half-cycle is selected.

reliable for this study, as it was capable of selecting the required data points even from data with low signal-to-noise ratios. The bottom plot of Figure 4.4 shows the successful selection of data points from two high-low cycles recorded at the $9^{\text{th}}$ ( 5% transmission) filter position, which has lower signal-to-noise ratio than the data from the fully open filter position.

Figure 4.5 illustrates the similarities between the distributions of final non-linearity values when the data selection from the middle of each half-cycle is adjusted to 55% and 65%. Calculation of this differential non-linearity is discussed later in Section 4.5.2.

## 4.4 LED Asymmetry and Average Anode Current

After selecting the data points required for the analysis using the Sobel filtering method, the mean value of each data chunk (selected data points from each half-cycle) was calculated and labeled as either $H$ or $L$ based on the mean of the raw data. If the mean value of a data chunk was larger than the raw data mean, it was

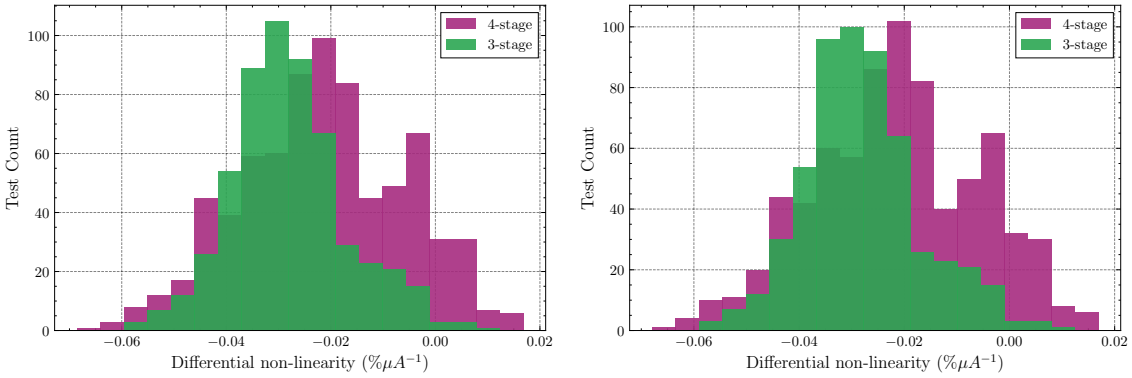


(a) Data selection: 55%

(b) Data selection: 65%

Figure 4.5: The distributions of final non-linearity (differential) values: (a) 55% of the data selected from each half-cycle, and (b) 65% selected.

labeled as $H$ (marked in red in Figure 4.4) and labeled as $L$ (in green) otherwise.

The final LED asymmetry for a filter position $f$, denoted as $(A_{\text{LED}})_f$, is then determined by averaging all the asymmetries of each adjacent high-low pair (pairwise asymmetry) using Equation 4.5.

$$(A_{\text{LED}})_f = \frac{1}{N_f} \sum_{i=1}^{N_f} \left( \frac{H - L}{H + L} \right)_i \tag{4.5}$$

Where $N_f$ is the number of high-low pairs in the data for the filter $f$, and $H$(or $L$) is the mean of the selected data chunk. The asymmetry calculation for the quartet method uses the same equation (4.5), but the data selection for the chunk $H$ is different. Instead of using one full data chunk as $H$, quartet method selects both neighboring half-chunks of $H$s closest to an $L$ (as shown in Figure 4.2). The distribution of asymmetries calculated for all nine filters is shown in Figure 4.6 (pairwise) and Figure 4.7 (quartet).

On average, around 860 high-low pairs ($N_f$) are used to calculate the final pairwise LED asymmetry (∼430 for quartet). The uncertainty of each final LED asymmetry value for a filter, denoted as $\delta\,(A_{\text{LED}})_f$, is estimated using the standard error [38], as shown in Equation 4.6.

$$\delta\,(A_{\text{LED}})_f = \pm \frac{\sigma_f}{\sqrt{N_f}} \tag{4.6}$$

Here, $\sigma_f$ is the standard deviation of the pairwise asymmetry distribution of filter $f$.

Similar to the asymmetry calculation for filter position $f$, the average anode

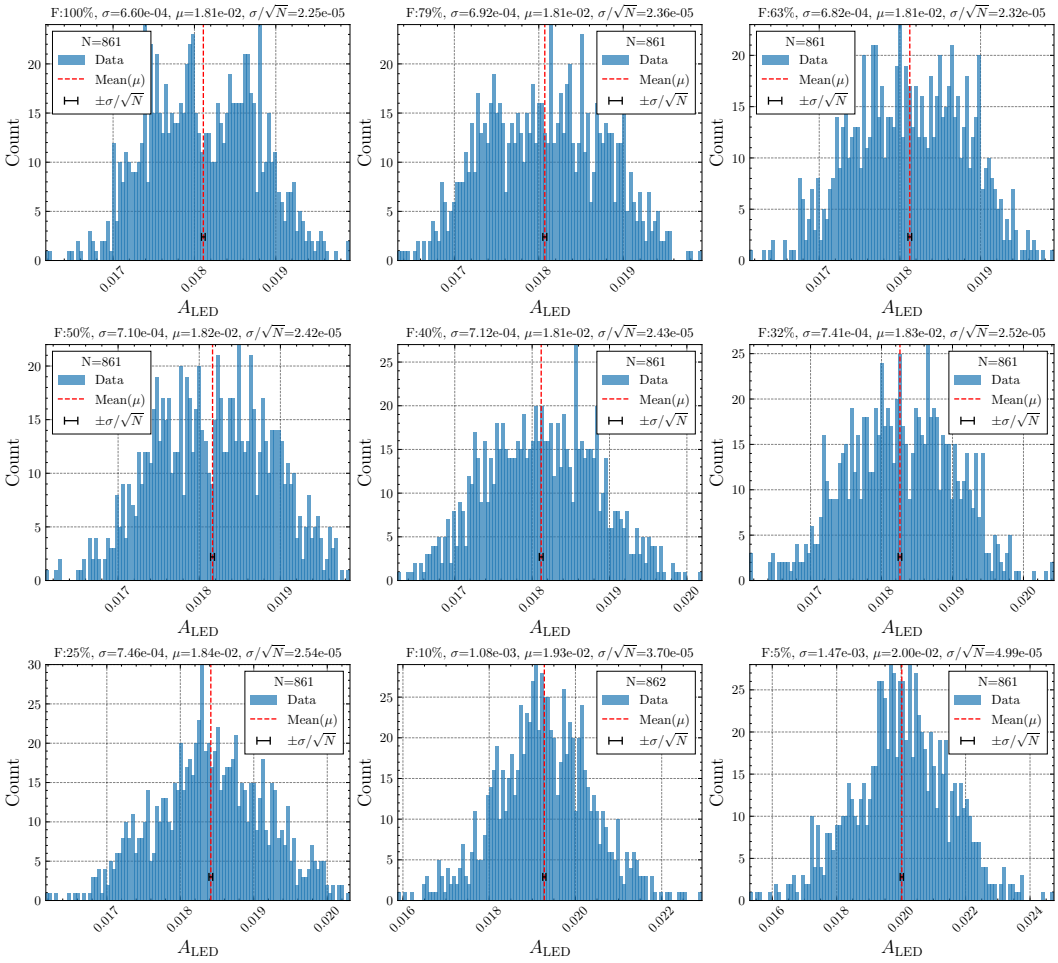


Figure 4.6: Pairwise asymmetry distribution of all 9 filter positions with their means and uncertainties.

current $(I_{\text{Anode}})_f$ is calculated using Equation 4.7 with the PMT base preamplifier impedance ($\beta$) value.

$$(I_{\text{Anode}})_f = \frac{1}{N_f \beta} \sum_{i=1}^{N_f} \left( \frac{H+L}{2} \right)_i \tag{4.7}$$

Estimating the uncertainty of the average anode current, denoted as $\delta\,(I_{\text{Anode}})_f$, for each filter position $f$ is done in a manner similar to that of the LED asymmetries, using the standard error.

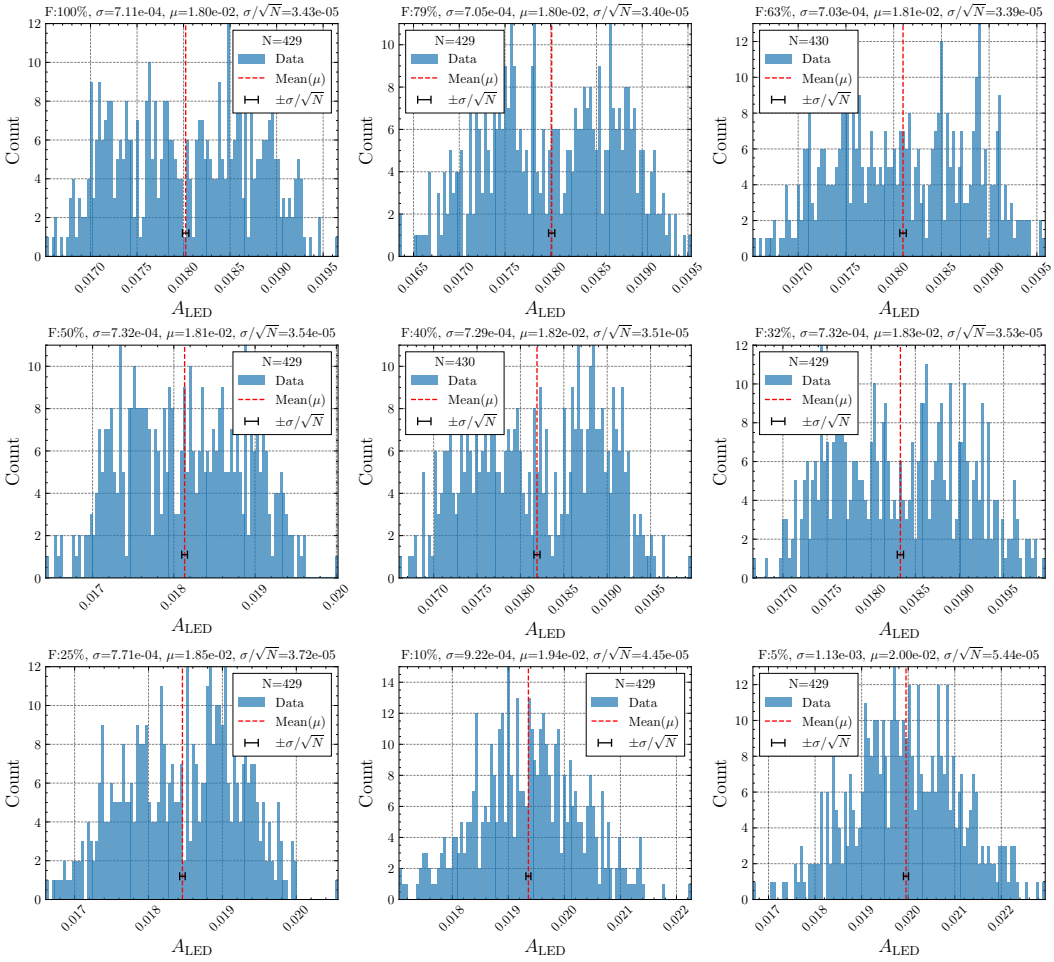


Figure 4.7: Asymmetries of all 9 filter positions calculated using the quartet method.

## 4.5 Non-Linearity Calculation

The calculated LED asymmetry values, along with the associated average anode currents for each filter position, can now be used to measure the non-linearity. A PMT is said to be linear if the measured LED asymmetry remains constant as the average anode current (signal amplitude) changes. The goal of this measurement is to quantify it precisely. This study employed two methods to estimate the non-linearity of PMTs using the measured LED asymmetry: *integral* non-linearity and *differential* non-linearity.

### 4.5.1 Integral Non-Linearity

This method quantifies the non-linearity of a PMT across the entire tested anode current range. First, a graph of LED asymmetry verses average anode current is

plotted (as shown in the top plot of Figure 4.9), and a linear function was fitted to the data points [39]. The parameters of this fit are then used to measure the non-linearity using the following calculation.

Let's assume a linear function $A = mI_{anode} + A_{true}$ as shown in Figure 4.8, where the measured asymmetry ($A$) expressed as a function of the anode current ($I_{anode}$). $m$ is the slope of the function and $A_{true}$ is the asymmetry at zero anode current (true asymmetry). If the maximum value of the function is equal to the intercept ($[A]_{I_{\max}} = A_{true}$), the function can be re-expressed as $A = A_{true}$. Therefore, if the function is constant,

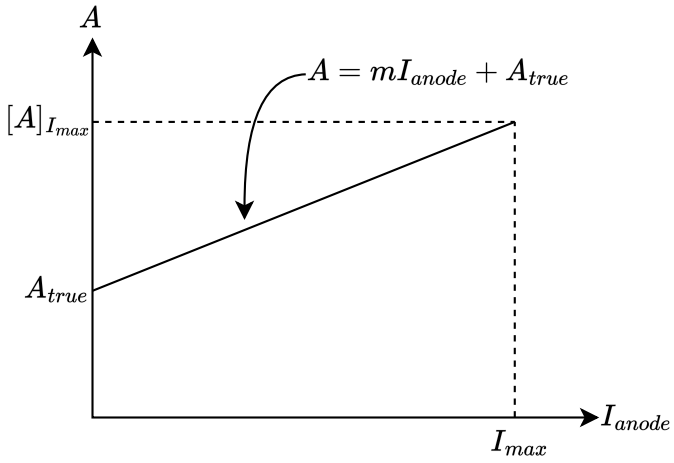


Figure 4.8: The measured asymmetry ($A$) expressed as a first order function of the PMT anode current ($I_{anode}$).

$$\left(\frac{[A]_{I_{\max}}}{A_{true}} - 1\right) = \left(\frac{m}{A_{true}}\right) I_{\max} = 0 \tag{4.8}$$

Any non-zero value for the expression 4.8 quantifies the deviation of the function from being constant. By applying this calculation with the fit, the integral non-linearity can be calculated as a percentage using the following Equation 4.9 [28].

$$\text{Integral non-linearity} = \left(\frac{m_{\text{fit}}}{(A_{true})_{\text{fit}}}\right) I_{\max} \times 100\% \tag{4.9}$$

Here, $m_{\text{fit}}$ and $c_{\text{fit}}$ are the slope and intercept of the fit. $(I_{\text{Anode}})_{\max}$ is the maximum anode current used for the fit.

This is called an 'integral' method because it characterizes the non-linearity of the PMT using its full measured anode current range. However, during the MOLLER experiment, the beam fluctuations are not expected to produce anode current devi-

ations as large as 10 $\mu$A (which is the range in which the PMTs are tested in this study). Therefore, the study also evaluates the non-linearity using a 'differential' method.

### 4.5.2 Differential Non-Linearity

Non-linearity measurement evaluates whether the measured LED asymmetry remains the same for different anode currents. This information could also be inferred from the slope of a linear function (a line) fitted to the LED asymmetry data. However, fitting assumes that the data has a linear trend to begin with, while in reality, the data might be described by a different function. Therefore, without fitting a line to the data, the trend is determined by a weighted mean of slopes between each adjacent data points on the graph of LED asymmetry versus anode current (Figure 4.9). Slopes between the adjacent data points ($\Delta A/\Delta I$) are calculated using the following Equation 4.10.

$$\left(\frac{\Delta A}{\Delta I}\right)_l = \frac{(A_{\text{LED}})_{l+1} - (A_{\text{LED}})_l}{(I_{\text{anode}})_{l+1} - (I_{\text{anode}})_l}; \quad l = 1, \cdots, L-1 \tag{4.10}$$

Where $L$ is the number of LED asymmetry data points. The weighted mean is obtained by fitting a constant value to the calculated slopes [39].

Figure 4.9 displays both the integral non-linearity (top) and the differential non-linearity (bottom) plots, along with the calculated final non-linearities of a PMT.

During PMT measurements, it was found that the LED asymmetry values at lower anode currents almost always deviate significantly from the rest as shown in Figure 4.9. Therefore, the analysis disregards the data from the two dimmest filter position.

The chi-square ($\chi^2$) value, which is used to estimate the degree to which the fitted function matches the data, is calculated using the following Equation 4.11 [38].

$$\chi^2 = \sum_{i=1}^{M} \frac{(O_i - E_i)^2}{\sigma_i^2} \tag{4.11}$$

Where $O_i$ is the measured (observed) LED asymmetry data, $E_i$ is the fitted (expected) data, $\sigma_i$ is the uncertainty of the observed data (estimated using Equation 4.6), and $M$ denotes the number of data points. A good fit is observed when the reduced chi-square reads 1 ($\chi^2/\text{ndf} = 1$), where 'ndf' represent the degrees of freedom ($\text{ndf} = M - 2$).

The calculated integral non-linearity is unitless, while the differential non-linearity is expressed in units $\%\mu A^{-1}$. Assuming the expected the anode current fluctuation during the MOLLER experiment is as large as 1 $\mu A$, the expected final differential

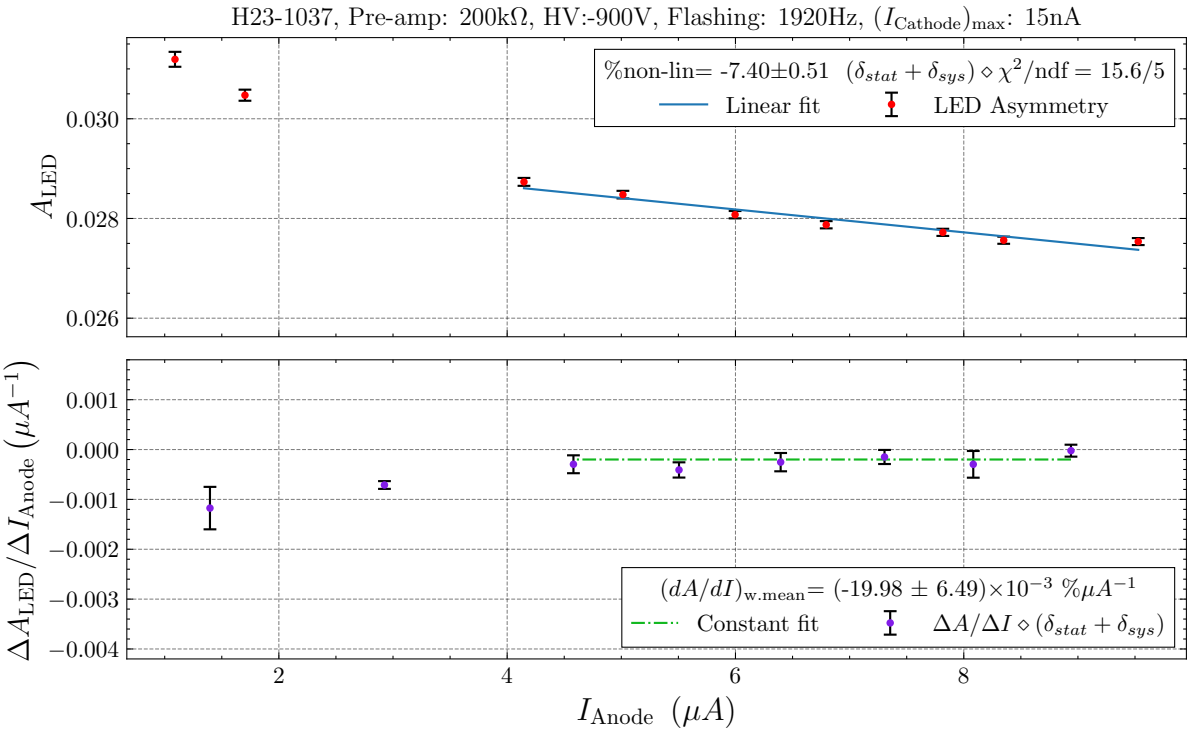


Figure 4.9: Integral (top) and differential (bottom) non-linearity plots containing final results with total uncertainties $(\delta_{stat} + \delta_{sys})$.

non-linearity for this particular PMT is $(-19.98 \pm 6.49) \times 10^{-3}\%$, which is much smaller that the $0.5 \pm 0.1\%$ non-linearity requirement for the MOLLER experiment.

## 4.6 Systematic Error Analysis

In addition to the main non-linearity measurements taken during the data collection process, data from 20 consecutive non-linearity runs were collected for 29 PMTs to assess the systematic uncertainty. Figure 4.10 illustrates the distribution of LED asymmetries for each run in the 20 consecutive measurements of a PMT at each filter position.

The systematic uncertainty on the measured asymmetry for each filter is estimated by the standard deviation of each distribution. Equation 4.12 shows the formula for the standard deviation of a population, where $\bar{x}$ is the population mean, and $N$ is the number of samples.

$$\text{SD} = \sqrt{\frac{1}{N-1}\sum_{i=0}^{N}(x_i - \bar{x})^2} \tag{4.12}$$

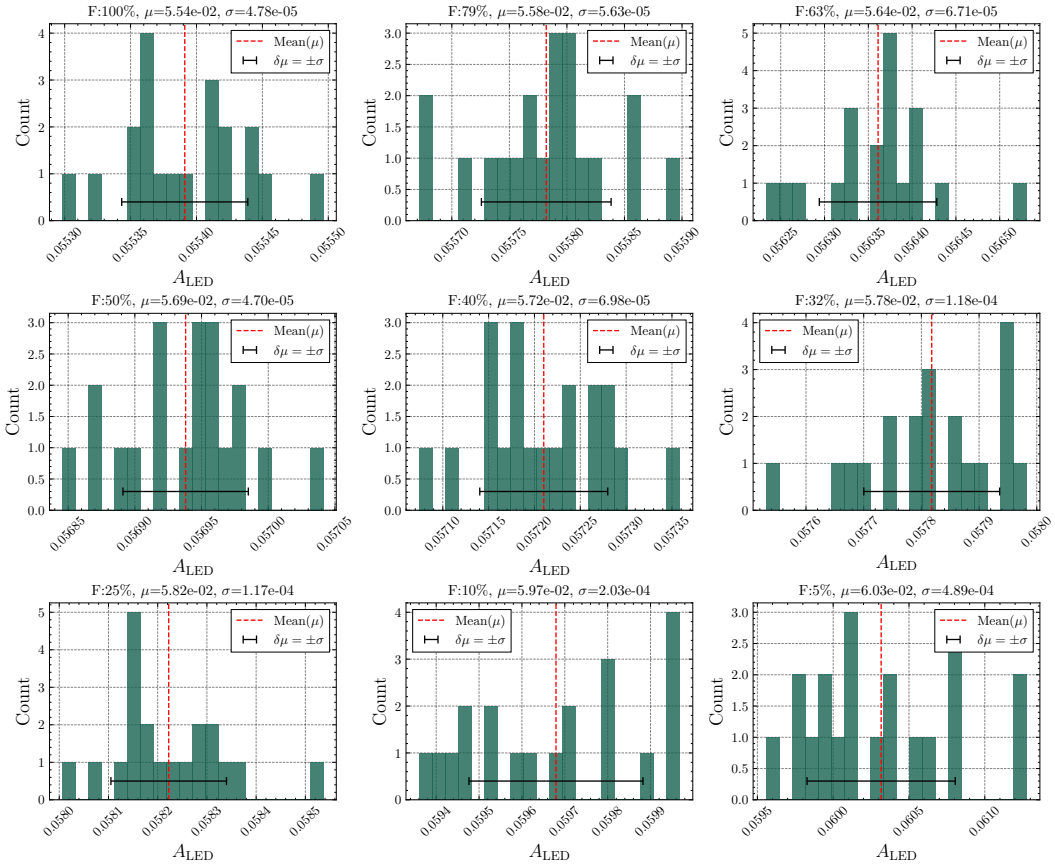


Figure 4.10: LED asymmetry distribution of 20 consecutive non-linearity runs.

Figure 4.11 shows the variation of systematic uncertainty of asymmetry measurement with respective mean anode current. The plot contains data from 29 PMTs.

The statistical uncertainties of each LED asymmetry and anode current are estimated using Equations 4.6 and 4.7. The systematic uncertainty of each asymmetry measurement with respect to its anode current is derived from the fit of the distribution shown in Figure 4.11. The total uncertainty of the measured LED asymmetry values is then calculated by combining the statistical and respective systematic uncertainties in quadrature, as shown in Equation 4.13.

$$\delta A = \sqrt{\delta^2_{stat} + \delta^2_{sys}} \tag{4.13}$$

The total LED asymmetry uncertainties are then used with fitting function to acquire the uncertainties of the linear fit parameters [39]. The final percent uncertainty for the integral non-linearity ($\%\delta_{\text{lin}}$) is then obtained by propagating the uncertainties using Equation 4.14.

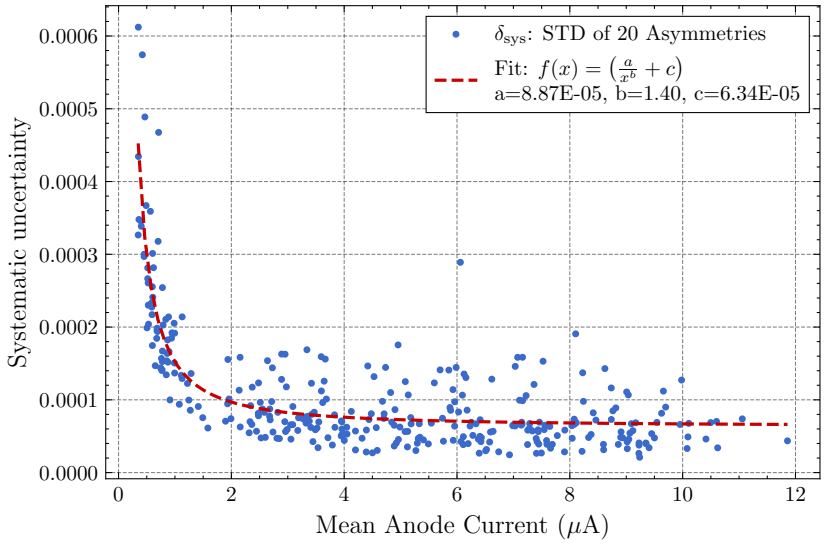


Figure 4.11: Variation of systematic uncertainty with the mean anode current.

$$\%\delta_{\text{lin}} = \frac{m_{\text{fit}}}{(A_{true})_{\text{fit}}} I_{\text{max}} \times \sqrt{\left(\frac{\delta m_{\text{fit}}}{m_{\text{fit}}}\right)^2 + \left(\frac{\delta(A_{true})_{\text{fit}}}{(A_{true})_{\text{fit}}}\right)^2 + \left(\frac{\delta I_{max}}{I_{max}}\right)^2} \times 100\% \quad (4.14)$$

Total uncertainties of the individual LED asymmetry points ($\delta A_i$), and corresponding anode current $\delta I_i$ are propagated through Equation 4.15 to obtain the uncertainties of individual $\Delta A/\Delta I$ points.

$$\delta\left(\frac{\Delta A}{\Delta I}\right)_i = \left(\frac{\Delta A}{\Delta I}\right)_i \times \sqrt{\left(\frac{\delta A_{i+1} + \delta A_i}{A_{i+1} - A_i}\right)^2 + \left(\frac{\delta I_{i+1} + \delta I_i}{I_{i+1} - I_i}\right)^2} \quad (4.15)$$

Here, $i = 1, \cdots, R$, where $R$ is the number of $\Delta A/\Delta I$ points. A constant value was then fitted to these data points to obtain the final differential non-linearity and its associated uncertainty.

The uncertainties of the LED asymmetry data points, shown in top plot in Figure 4.9, are estimated using this method (Equation 4.13). These final uncertainties with systematic errors are then propagated to the bottom differential non-linearity plot when calculating individual slopes ($\Delta A/\Delta I$), consequently scaling the uncertainty of the final differential non-linearity.

## 4.7 Validation of Systematic Error Evaluation

Figure 4.12 shows the contribution of the systematic uncertainty on the chi-square distribution of the linear fit used to assess the integral non-linearity. The distributions are separated by the PMT base used and include all the conducted non-linearity runs.

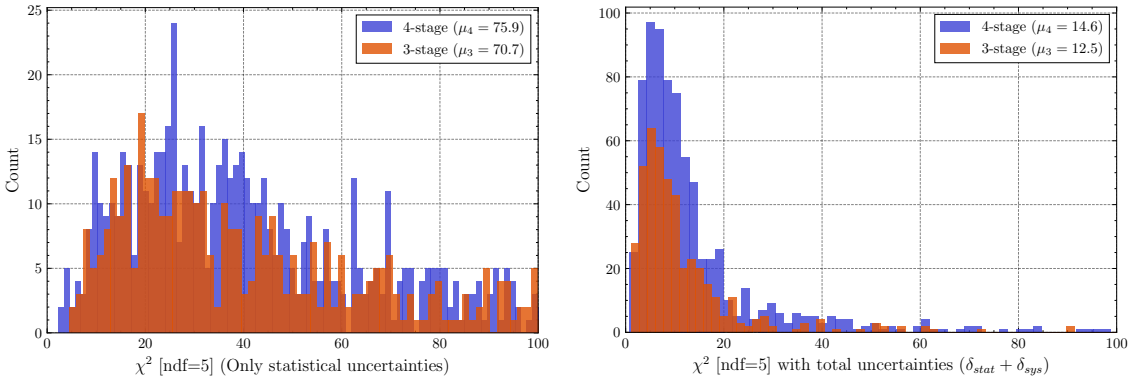


(a) (b)

Figure 4.12: The distribution of chi-square values for the linear fit with 5 degrees of freedom: (a) accounting for only the statistical uncertainties and (b) total uncertainty.

Theoretically, the mean of a chi-square distribution equals its degrees of freedom [38], which in this case is 5. Adding the systematic uncertainty reduced the mean of the chi-square distribution, bringing it closer to the theoretical value and resulting in better linear fits. Figure 4.13 illustrates the difference between the theoretical and observed chi-square distributions for the PMTs tested with the 3-stage base.

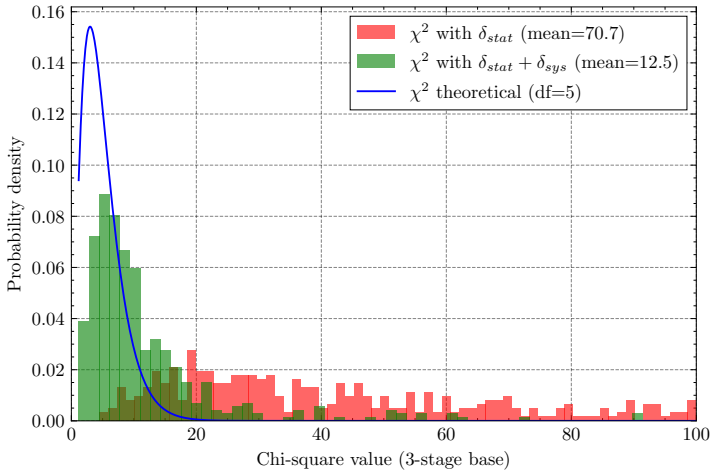


Figure 4.13: Theoretical and observed chi-square distributions (with and without systematic uncertainties) of the linear fit used to assess the integral non-linearity.

Figure 4.14 shows the distribution of pulls for each linear fit used to calculate the integral non-linearity. Pull value of each data point is calculated using the Equation 4.16, where $O$ is the observed (measured) data and $E$ denotes the expected value based on the fit, and $\sigma_o$ is the uncertainty of the measured data.

$$\text{Pull} = \frac{O - E}{\sigma_o} \tag{4.16}$$

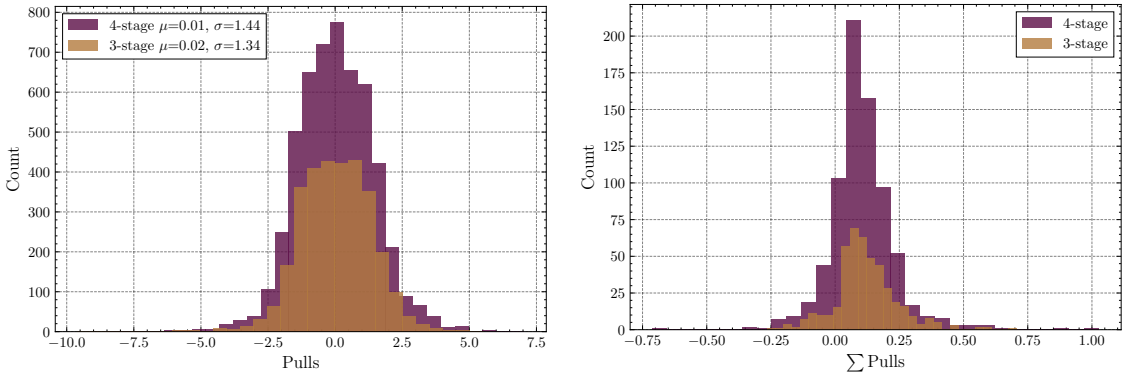


(a) (b)

Figure 4.14: (a) Distribution of pulls and (b) sum of all the pull values of each linear fit used to assess the integral non-linearity.

# Chapter 5

# Results

At the time of writing, 113 PMTs had been tested with the apparatus. This chapter discusses the final results of the analysis for those tested PMTs. These results include a comparison of PMT non-linearity values between single and 20 consecutive runs, the overall distribution of final integral and differential non-linearities for all tested PMTs, and the correlation of non-linearity with test parameters.

Since the collected data set contained several hundred gigabytes of data, a database was created to store the non-linearity results as an optimization measure. This database will also allow sharing the analyzed results with the MOLLER collaboration in the future. The organization of this final database is presented in Appendix B.

## 5.1 Measurement Stability

The non-linearity measurement was repeated multiple times with several PMTs to assess the stability of the experimental setup and to improve the estimation of systematic errors as discussed in Section 4.6. The top plot in Figure 5.1 shows the graph of LED asymmetry against the anode current for both a single non-linearity run and the mean of 20 consecutive runs. This demonstrates that, even over extended periods, up to 30 minutes, the experimental apparatus produces consistent measurements from a PMT. The uncertainties of the single run asymmetries are taking into account the statistical and systematic errors. The uncertainties of the 20 consecutive runs are estimated using the standard deviation as shown in Figure 4.10. During all of these measurements from more than 100 PMTs, the recorded temperature range was from 20.4°C to 23.5°C.

Using the estimated total uncertainty of each run in the 20 consecutive measure-

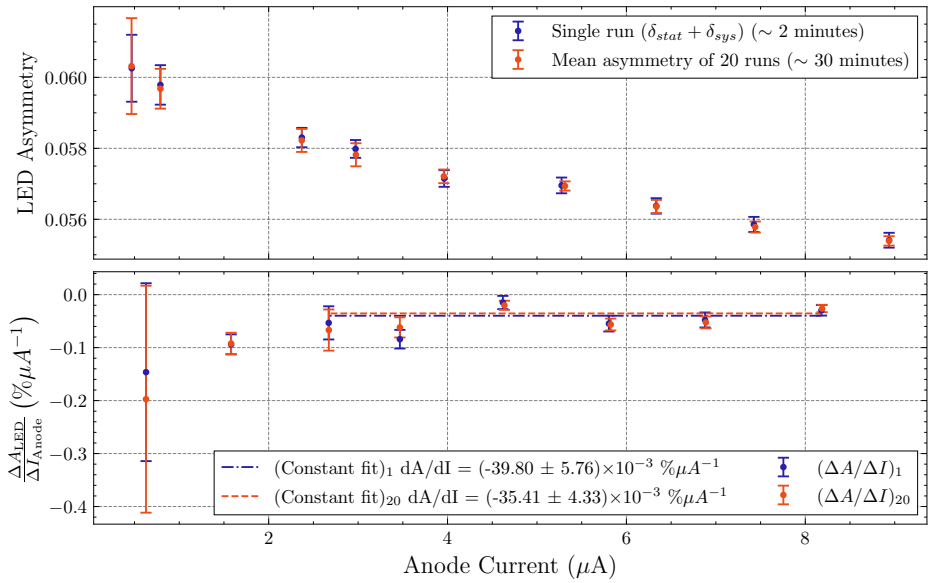


Figure 5.1: Top: LED asymmetries of single (including systematic uncertainties) and mean asymmetry of 20 multiple runs. Bottom: slopes between each adjacent LED asymmetry points against the mean anode currents. Data from the dimmest two filters were excluded from the fit.

ment, Figure 5.2 displays the variation of integral and differential non-linearity values across the 20 consecutive runs. The final data point in each plot represents the mean of the 20 runs, with its uncertainty estimated using the standard deviation.

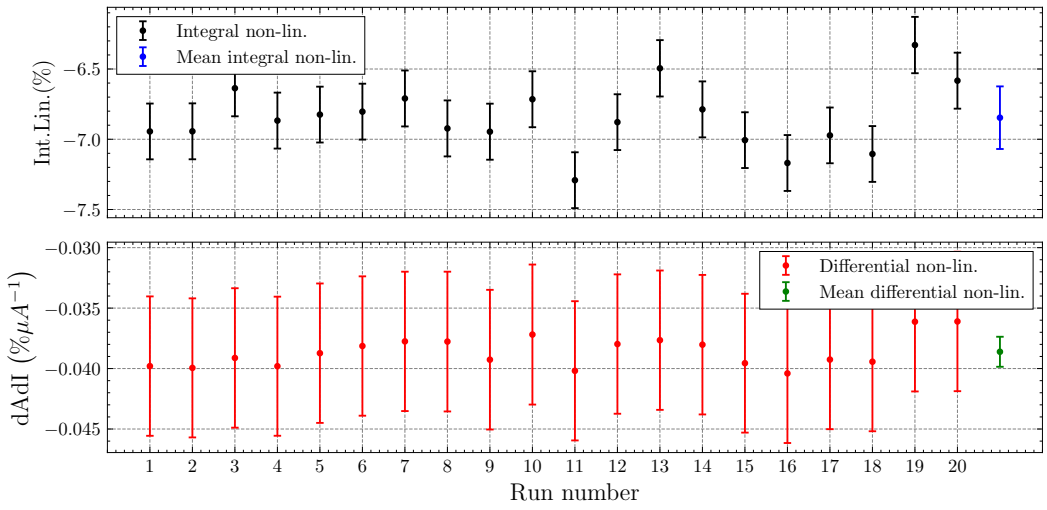


Figure 5.2: Measured integral and differential non-linearities distribution of a PMT for 20 consecutive runs.

## 5.2 Non-linearity Results

As discussed in the Chapter 3, the measurements collect data from 10 separate non-linearity runs from each PMT. These runs include variations in LED flashing frequencies, maximum cathode currents, mean asymmetries, and high voltages. The following results show the distribution of non-linearities across all those tests, comprising a total of 1,090 runs.

Figure 5.3(a) illustrates the distribution of integral non-linearity for all tested runs, separated by the number of stages utilized. Figure 5.3(b) presents the same results ordered in ascending sequence with their respective uncertainties.

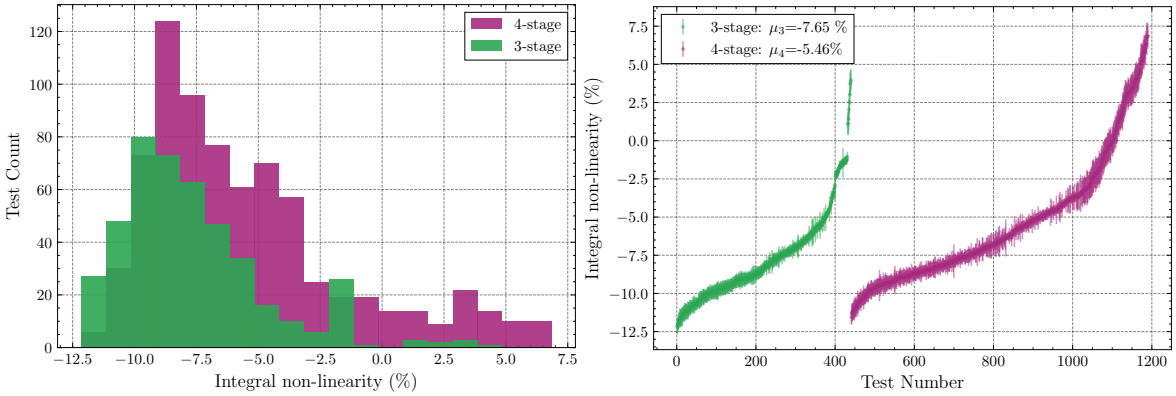


(a) (b)

Figure 5.3: Integral non-linearity distribution of PMTs tested with 3-stage and 4-stage bases plotted as (a): histogram, (b): ordered values with uncertainties.

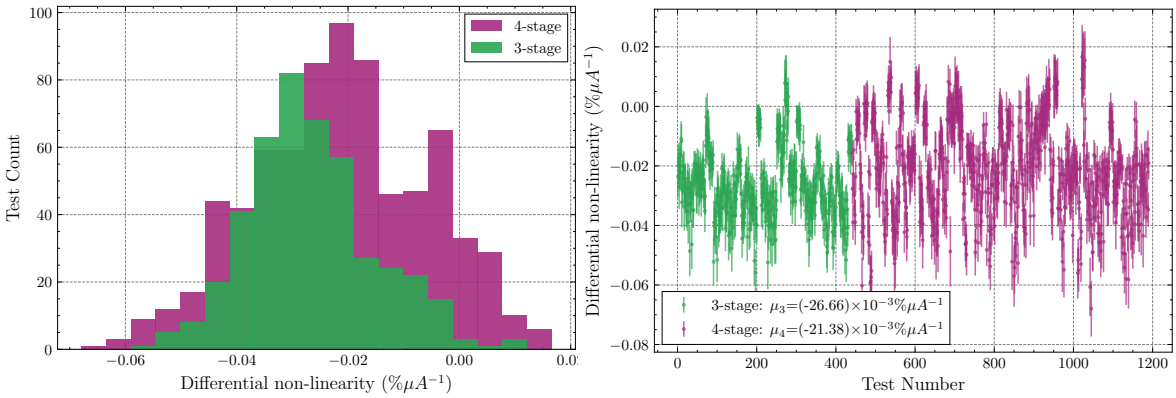


(a) (b)

Figure 5.4: Differential non-linearity distribution of PMTs tested with 3-stage and 4-stage bases plotted as (a): histogram, (b): values with uncertainties.

Figure 5.4(a) shows the distribution of differential non-linearity for all tested runs,

separated by the number of stages utilized. Figure 5.3(b) presents the same results with their uncertainties. As seen from Figure 5.4, the differential non-linearities of all the tested PMTs meet the MOLLER 0.5±0.1% requirement.

Figures 5.5 and 5.6 show the distributions of integral and differential non-linearity values, with a single entry per PMT. Among the 10 non-linearity runs performed, the selected runs feature a 1920 Hz LED flashing rate and a maximum cathode current of 15 nA[1].

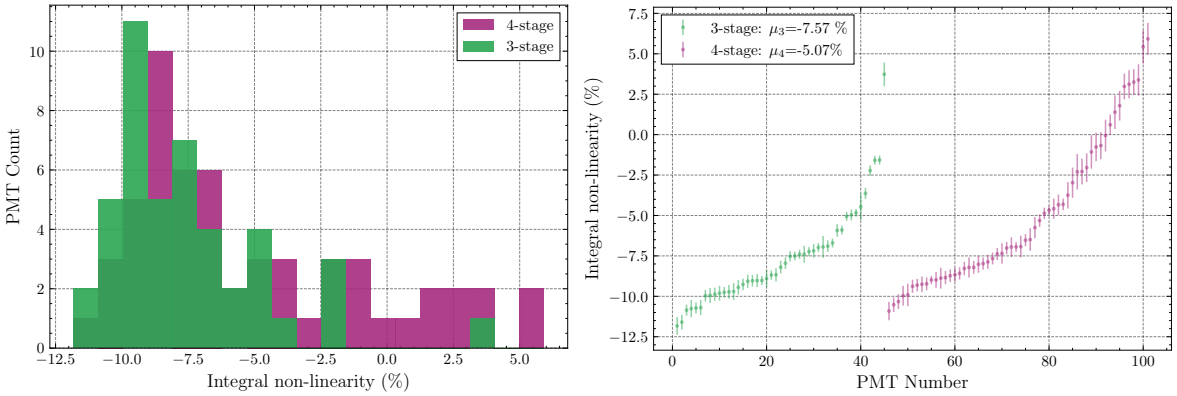


(a) (b)

Figure 5.5: Integral non-linearity distribution of PMTs (single entry per PMT) tested with 3-stage and 4-stage bases plotted as (a): histogram, (b): values with uncertainties.

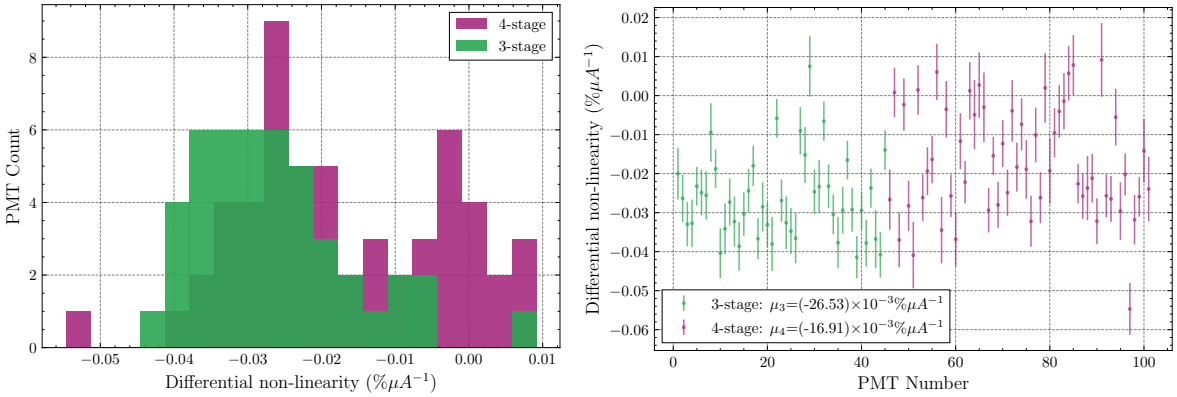


(a) (b)

Figure 5.6: Differential non-linearity distribution of PMTs (single entry per PMT) tested with 3-stage and 4-stage bases plotted as (a): histogram, (b): values with uncertainties.

[1]Some of the selected runs with 4-stage PMTs have a maximum cathode current of 9 nA

The distribution of total uncertainty values for both integral and differential non-linearities are shown in Figure 5.7. The distribution in Figure 5.7(b) illustrates that the uncertainties are within the MOLLER requirement of ±0.1% (assuming <1 $\mu$A MOLLER beam variations).

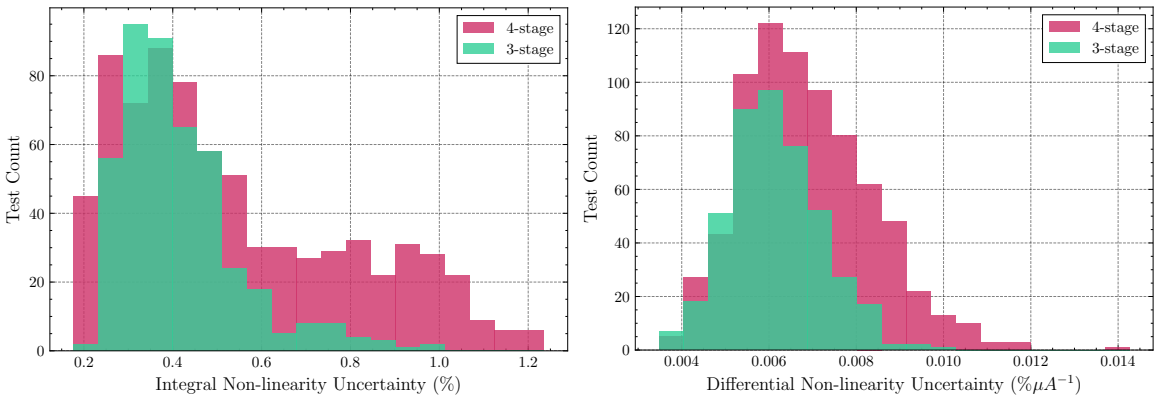


(a) (b)

Figure 5.7: Distribution of total uncertainty values of (a) integral and (b) differential non-linearities.

Figure 5.8 presents the distribution of total uncertainty with respect to their non-linearity values.

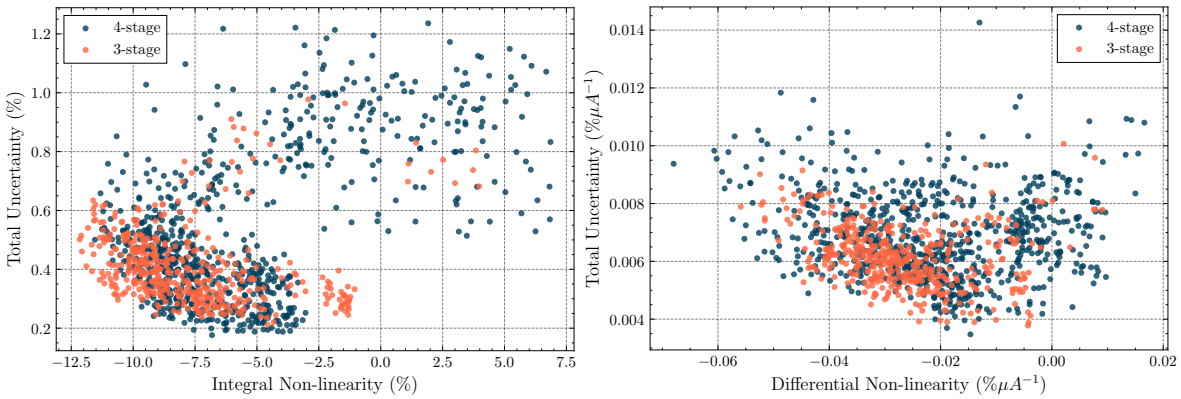


(a) (b)

Figure 5.8: Distribution of total uncertainties with their respective non-linearities.

The distribution of integral verses differential non-linearity shown in Figure 5.9 illustrate that there is a positive correlation between the two quantities.

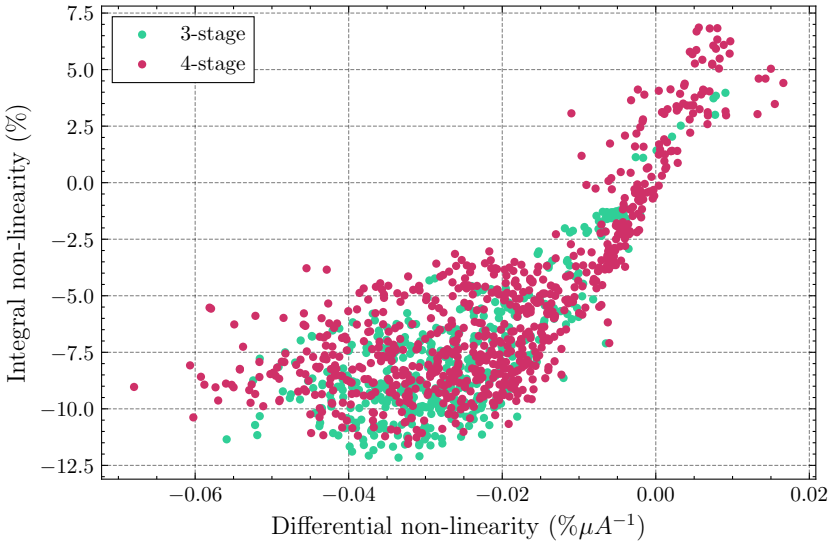


Figure 5.9: Distribution of integral non-linearity values with differential non-linearity.

## 5.3 Distribution of Measured Quantities

Following results shows the distribution of major test parameters and calculated quantities of the full data set.

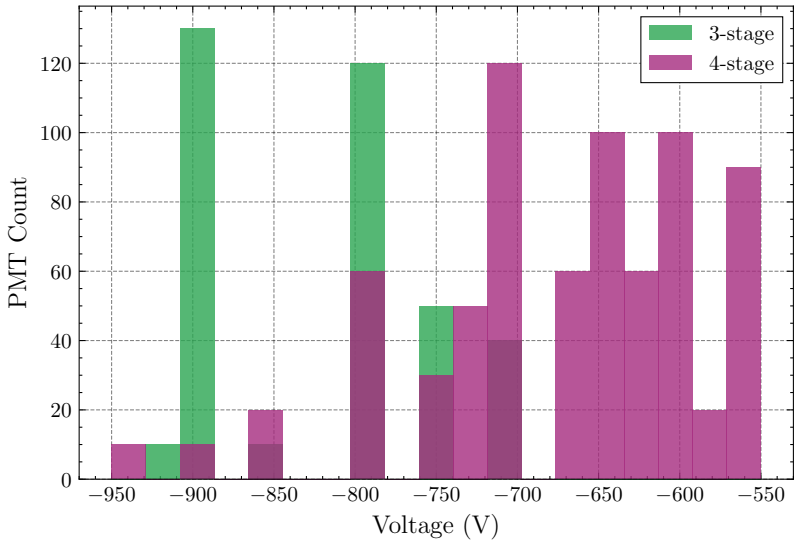


Figure 5.10: Distribution of PMT high voltages used for the non-linearity measurement.

Figure 5.10 illustrates the distribution of high voltage values used for the non-linearity measurement. PMTs equipped with the 4-stage base generally required lower high voltage to reach the 8–10 $\mu$A anode current range compared to those using the 3-stage base at similar cathode current levels. This difference arises from the

additional dynode stage in the 4-stage base, which provides greater amplification, thereby reducing the voltage required to achieve the target anode current.

Figure 5.11 illustrate the distribution of the standard deviation of the pedestal for all the tested PMTs. The pedestal standard deviation of 4-stage PMTs are generally

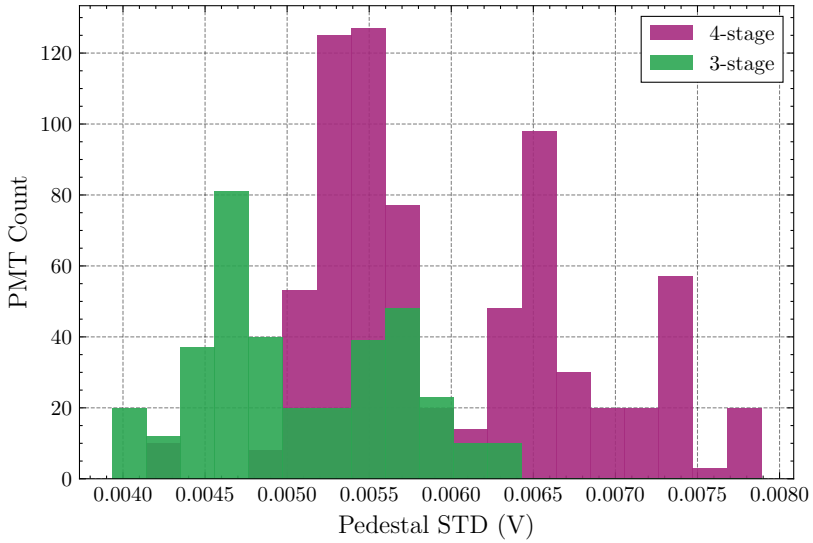


Figure 5.11: Pedestal standard deviation distribution

larger than the PMTs tested with 3-stage base. These pedestal runs are taken after the 2-hour warm-up and the HV for the PMTs were adjusted such that the maximum anode current is in between 8–10 $\mu$A.

Figure 5.12 presents the normalized distribution of measured asymmetry from the 9 filters.

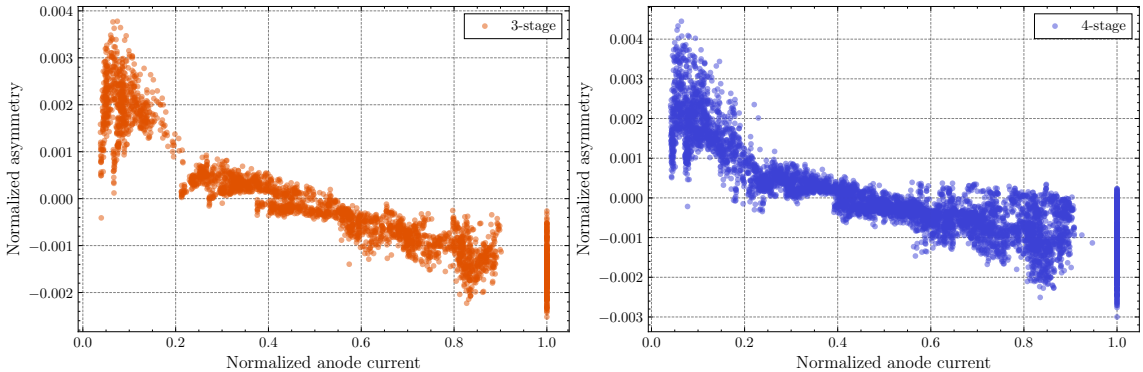


(a) (b)

Figure 5.12: Distribution of normalized asymmetries measured with the PMTs that utilized (a) 3 stages, (b) 4 stages. The asymmetries are normalized by their mean values and the anode currents are normalized by their maximum.

This result shows that, generally, the first two asymmetry data points (from the two dimmest filters) exhibit significant deviations from a linear trend compared to the others. Consequently, the asymmetry values associated with the two dimmest filter positions were excluded from the analysis to ensure an accurate calculation of the PMT non-linearity.

The variation of anode currents with the transmission rates of the ND filters for all the tested PMTs are shown in Figure 5.13(a). Figure 5.13(b) presents the normalized anode and cathode current variations with the filter transmission setting for one PMT. cathode and anode currents are normalized between 0 and 1. Since the anode current exhibits the same trend as the cathode current, this plot (Figure 5.13(b)) demonstrates that the cathode current response of the PMT is a significant contributor to the overall PMT non-linearity.

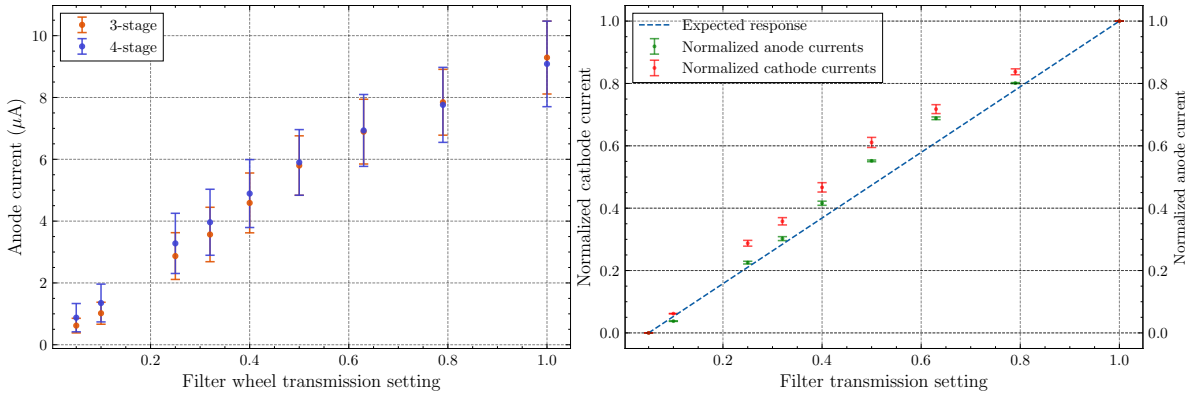


(a) Anode current variations for all the tested PMTs.

(b) Normalized anode and cathode current variations for one PMT.

Figure 5.13: Variations of anode and cathode currents with filter transmission rates (factory calibrated).

## 5.4 Correlations of Non-linearity with Test Parameters

With the use of all the calculated non-linearity data from the tested PMTs, the following results demonstrate the correlation of non-linearities with major test parameters.

Figure 5.14 illustrates the distribution of differential and integral non-linearity values across the high voltages used during the tests. The high voltage required by the PMTs to achieve the maximum anode current range of 8–10 $\mu$A appears to have no clear correlation with the non-linearity values.

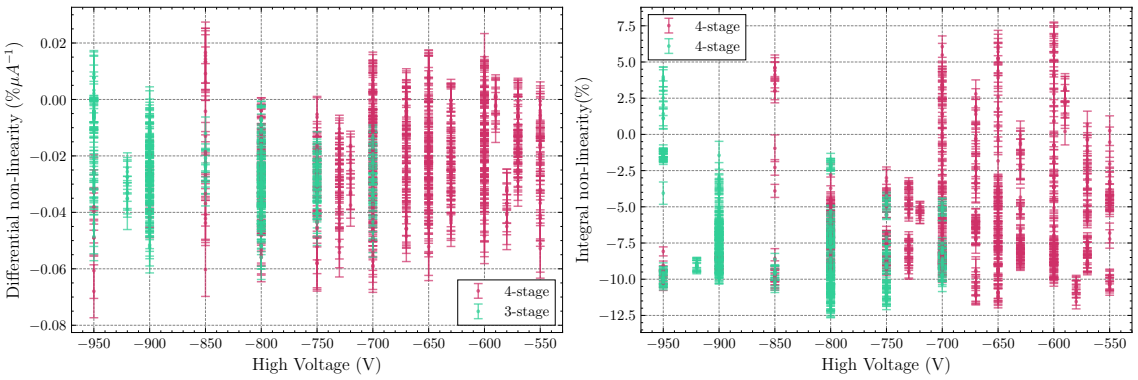


(a) (b)

Figure 5.14: Distribution of (a) differential and (b) integral non-linearity variations with the high voltage values.

Similarly, Figure 5.15 shows the distribution of non-linearities with pedestal standard deviations, revealing little to no correlation between the non-linearity values and the pedestal standard deviation.

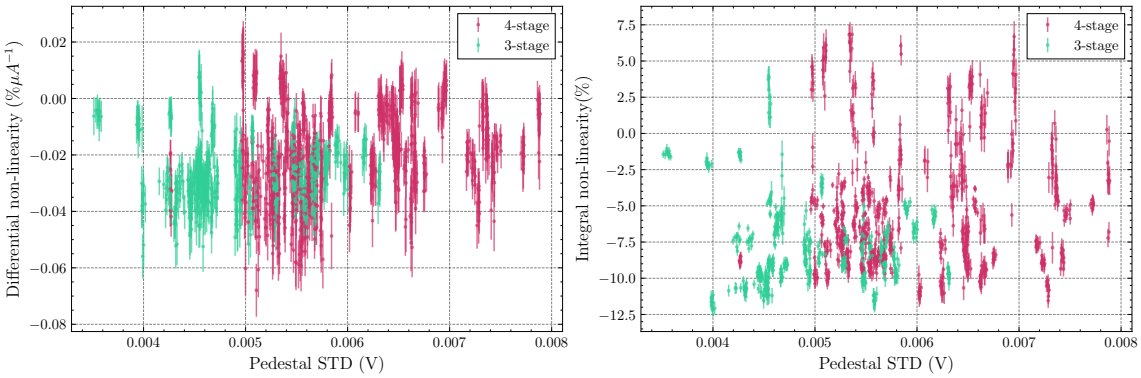


(a) (b)

Figure 5.15: Distribution of (a) differential and (b) integral non-linearity results variations with the standard deviation of the pedestal.

Figure 5.16 presents the variation of normalized differential non-linearities and integral non-linearities as a function of the measured mean LED asymmetry. The differential non-linearity values are normalized by the mean asymmetry for each respective run. The results indicate that lower asymmetry values generally correspond to better (i.e., closer to zero) non-linearity compared to higher asymmetry values.

Although the asymmetry is set by the LEDs to approximately 2–3% using current-limiting resistors, it varies due to LED voltage perturbations, as discussed in Table 3.1.

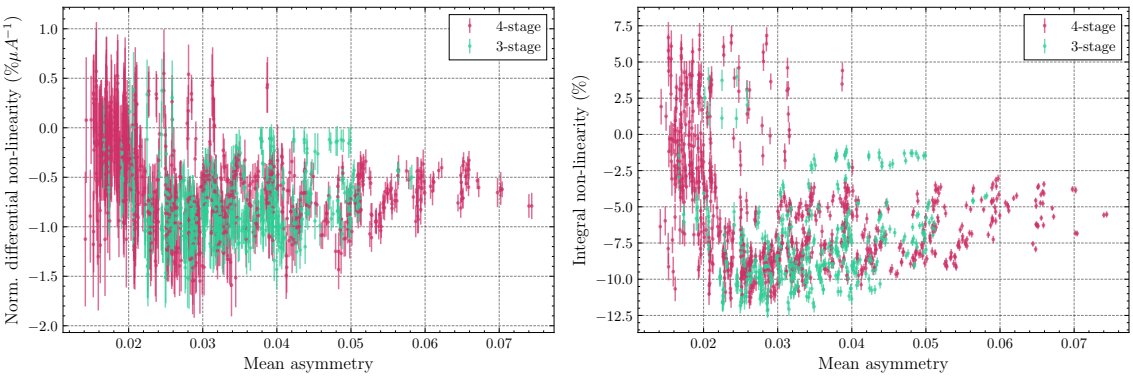


(a) (b)

Figure 5.16: Distribution of (a) normalized differential and (b) integral non-linearity results variations with mean asymmetry.

Figure 5.17 illustrates the variations in non-linearities with the voltages applied to the bright constant LED. In this context, higher voltages correspond to increased LED brightness. The results reveal a positive correlation between LED voltage and PMT non-linearities, with higher LED voltages being associated with reduced photocathode sensitivity of the PMT.

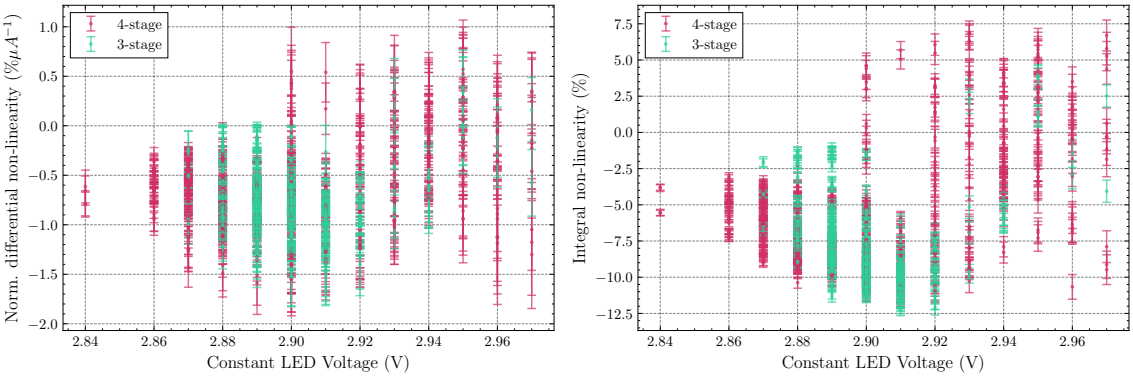


(a) (b)

Figure 5.17: Distribution of (a) normalized differential and (b) integral non-linearity results variations with constant LED voltage.

Figure 5.18 illustrates the distribution of non-linearities with the measured maximum PMT anode current. The differential non-linearity is normalized by the mean asymmetry. While the integral non-linearity shows no significant correlation with the maximum anode current, the differential non-linearity exhibits a positive correlation.

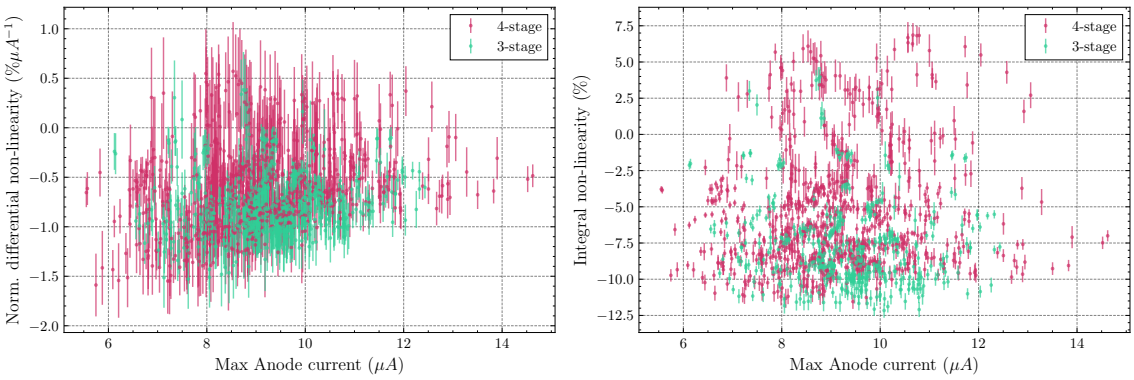


(a) (b)

Figure 5.18: Distribution of (a) normalized differential and (b) integral non-linearity results variations with max anode current.

During this study, every PMT is tested for non-linearity at multiple maximum cathode current settings (Table 3.1). The plots in Figure 5.19 and Figure 5.20 show the distribution of non-linearity values grouped by the same maximum cathode current.

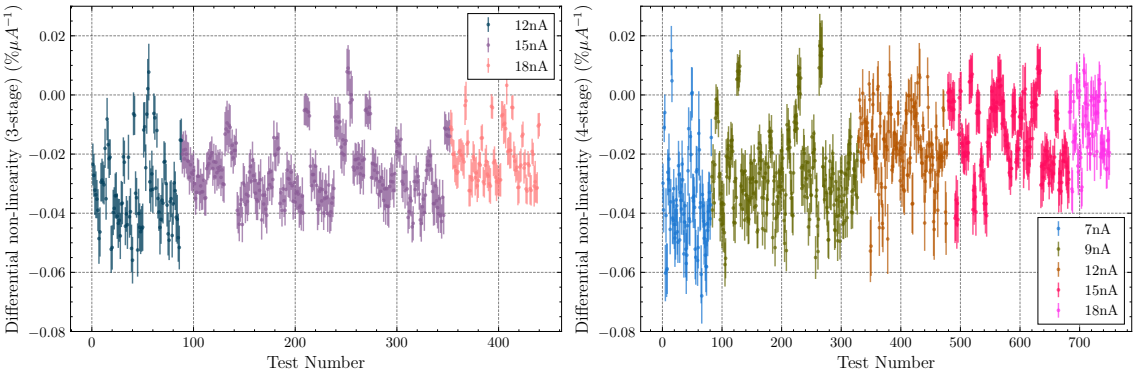


(a) 3-stage PMTs (b) 4-stage PMTs

Figure 5.19: Distribution of differential non-linearity values grouped with max cathode currents for PMTs tested with (a) 3-stage and (b) 4-stage bases.

The differential non-linearity values exhibit a positive trend with increasing maximum cathode current, whereas the integral non-linearity does not show a clear correlation.

Each PMT is tested for non-linearity at two different flashing frequencies: 1920 Hz and 960 Hz. The data collected at 1920 Hz were analyzed using the *pairwise* method, while the 960 Hz data were analyzed using the *quartet* method (see Section 4.2). Figure 5.21 shows the difference between the differential non-linearity results

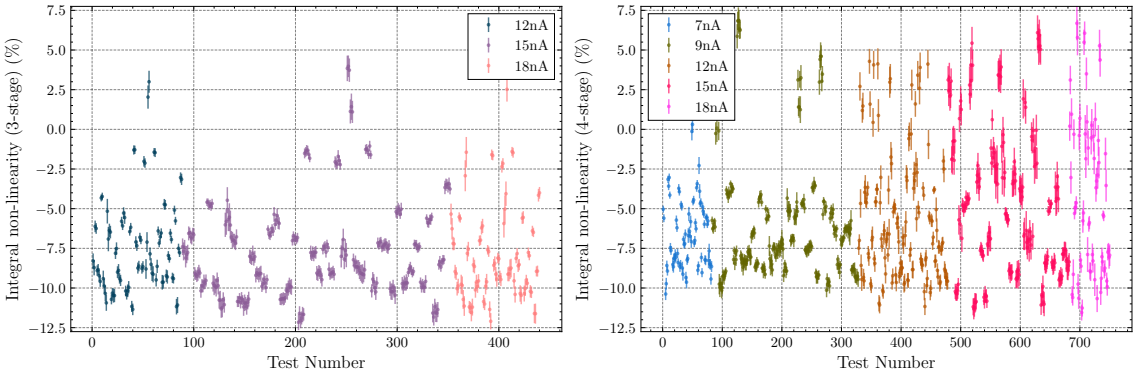


(a) 3-stage PMTs (b) 4-stage PMTs

Figure 5.20: Distribution of integral non-linearity values grouped with max cathode currents for PMTs tested with (a) 3-stage and (b) 4-stage bases.

obtained with the pairwise and quartet methods. In both cases, the results appear to be similar.

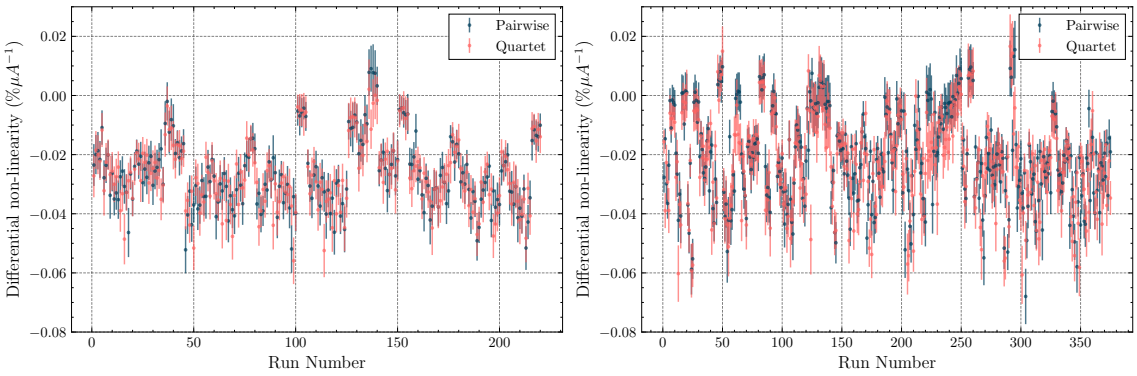


(a) 3-stage PMTs (b) 4-stage PMTs

Figure 5.21: Distribution of differential non-linearity values analyzed by pairwise and quartet methods for PMTs tested with (a) 3-stage and (b) 4-stage bases.

# Chapter 6

# Conclusion

This study has systematically characterized the non-linearity of the PMTs that are planned to be used in the main detector of the MOLLER experiment. The non-linearity of these PMTs play an important role when estimating the systematic uncertainty of the final MOLLER measurement which is aim to achieve an overall factional accuracy of 2.4% [15]. Due to this never seen before higher precision at low momentum transfers, the measurement of PMT non-linearities needed to be measured under conditions relevant to the MOLLER experiment precisely to reduce systematic uncertainties.

To that end, a test apparatus was built from scratch considering all the MOLLER requirements. The experimental setup was designed to replicate the asymmetrical light signals that PMTs will encounter during the MOLLER measurement, enabling precise evaluation of their performance in integration mode.

Key findings from this work include the development and validation of a robust methodology for measuring PMT non-linearity (differential) with a precision of $< \pm 0.1\%$, meeting the MOLLER experiment's stringent requirements. The results of the tested PMTs confirm that, within the tested range, PMTs exhibit non-linear behavior below the required threshold of 0.5%, ensuring their suitability for high-precision asymmetry measurements. This achievement directly addresses one of the critical challenges in the MOLLER experiment—minimizing systematic uncertainties in detector response.

The data collection with automation techniques developed for this study not only facilitated the efficient testing of over 300 PMTs but also provided a scalable framework for future experiments requiring large-scale detector arrays.

In addition to addressing the immediate goals of the MOLLER experiment, this research contributes to the broader field of particle physics by advancing the tech-

niques used for detector characterization. By achieving this level of precision, the study enhances the potential of the MOLLER experiment to probe fundamental parameters of the Standard Model, such as the weak mixing angle, and to identify signals of physics beyond the Standard Model.

Overall, this work represents a significant step forward in ensuring the reliability and accuracy of the MOLLER detector system. The methods and findings established here provide a foundation for the successful implementation of the MOLLER experiment and offer a template for tackling similar challenges in other high-precision measurements in experimental particle physics.

# References


[1] D. Griffiths, *Introduction to elementary particles*. John Wiley & Sons, 2020. (Cited on pages 1, 2, 3, 4, 5, 6, and 87.)

[2] S. Navas *et al.*, "Review of particle physics," *Phys. Rev. D*, vol. 110, no. 3, p. 030001, 2024. (Cited on pages 1, 2, 3, 4, and 6.)

[3] G. Aad, T. Abajyan, B. Abbott, J. Abdallah, S. A. Khalek, A. A. Abdelalim, R. Aben, B. Abi, M. Abolins, O. AbouZeid, *et al.*, "Observation of a new particle in the search for the standard model higgs boson with the atlas detector at the lhc," *Physics Letters B*, vol. 716, no. 1, pp. 1–29, 2012. (Cited on pages 2 and 4.)

[4] M. E. Peskin, *An introduction to quantum field theory*. CRC press, 2018. (Cited on page 3.)

[5] R. Demina and A. Garcia-Bellido, *Electroweak Symmetry and its Breaking*. World Scientific, 2023. (Cited on pages 4, 5, 6, and 82.)

[6] P. Anthony, R. Arnold, C. Arroyo, K. Baird, K. Bega, J. Biesiada, P. E. Bosted, M. Breuer, R. Carr, G. Cates, *et al.*, "Observation of parity nonconservation in møller scattering," *Physical review letters*, vol. 92, no. 18, p. 181602, 2004. (Cited on page 4.)

[7] J. Benesch, P. Brindza, R. Carlini, J. Chen, E. Chudakov, S. Covrig, M. Dalton, A. Deur, D. Gaskell, A. Gavalya, *et al.*, "The moller experiment: An ultra-precise measurement of the weak mixing angle using moller scattering," *arXiv preprint arXiv:1411.4088*, 2014. (Cited on pages 4, 7, 8, 9, 11, 12, 19, 22, and 82.)

[8] T.-D. Lee and C.-N. Yang, "Question of parity conservation in weak interactions," *Physical Review*, vol. 104, no. 1, p. 254, 1956. (Cited on page 5.)

[9] C.-S. Wu, E. Ambler, R. W. Hayward, D. D. Hoppes, and R. P. Hudson, "Experimental test of parity conservation in beta decay," *Physical review*, vol. 105, no. 4, p. 1413, 1957. (Cited on page 6.)

[10] S. L. Glashow, "Partial-symmetries of weak interactions," *Nuclear physics*, vol. 22, no. 4, pp. 579–588, 1961. (Cited on page 6.)

[11] S. M. Bilenky and J. Hošek, "Glashow-weinberg-salam theory of electroweak interactions and the neutral currents," *Physics Reports*, vol. 90, no. 2, pp. 73–157, 1982. (Cited on page 6.)

[12] A. CZARNECKI and W. J. MARCIANO, "Polarized mØller scattering asymmetries," *International Journal of Modern Physics A*, vol. 15, p. 2365–2375, June 2000. (Cited on pages 8 and 82.)

[13] P. Souder and K. Paschke, "Parity violation in electron scattering," *Frontiers of Physics*, vol. 11, pp. 1–31, 2016. (Cited on page 8.)

[14] J. P. N. N. Brynne Blaikie, Michael Gericke, "Developing the integrating detector electronics chain for the moller experiment." `https://indico.cern.ch/event/1191895/contributions/5321234/attachments/2669507/4627109/2023CAP_Blaikie.pdf`, 2022. Accessed: 2024-07-24. (Cited on pages 10 and 82.)

[15] D. Armstrong, S. Covrig, J. Fast, C. Gal, M. Gericke, D. Jones, P. King, K. Kumar, J. Mammei, D. McNulty, and et al., *MOLLER Technical Design Report - Final*. Feb 2024. (Cited on pages 10, 11, 12, 13, 14, 15, 16, 17, 19, 20, 21, 25, 33, 35, 49, 75, 82, and 83.)

[16] H. P. K.K., *Photomultiplier Tubes - Basics and Applications 4th ed.* Hamamatsu Photonics K.K., 2017. (Cited on pages 12, 13, 15, and 16.)

[17] "Et enterprises 78 mm (3") photomultiplier 9305kb series data sheet." `https://et-enterprises.com/images/data_sheets/9305KB.pdf`. Accessed: 2024-08-24. (Cited on pages 14, 19, and 21.)

[18] A. G. Wright, *The photomultiplier handbook*. Oxford University Press, 2017. (Cited on page 15.)

[19] S. Yin, Q. Lin, and Y. Li, "Study on linearity of photomultiplier tubes by accurately controlling the incident light intensity," *Optical and Quantum Electronics*, vol. 56, no. 3, p. 310, 2024. (Cited on pages 16 and 17.)

[20] H. Lv, X. Sheng, H. He, J. Liu, Z. Zhang, C. Hou, J. Zhao, L. collaboration, *et al.*, "Extension of photomultiplier tube dynamic range for the lhaaso-km2a electromagnetic particle detectors," *Nuclear Instruments and Methods in Physics Research Section A: Accelerators, Spectrometers, Detectors and Associated Equipment*, vol. 781, pp. 34–38, 2015. (Cited on pages 16 and 17.)

[21] D. Barnhill, F. Suarez, K. Arisaka, B. Garcia, J. Gongora, A. Lucero, I. Navarro, T. Ohnuki, A. Risi, and A. Tripathi, "Testing of photomultiplier tubes for use in the surface detector of the pierre auger observatory," *Nuclear Instruments and Methods in Physics Research Section A: Accelerators, Spectrometers, Detectors and Associated Equipment*, vol. 591, no. 3, pp. 453–466, 2008. (Cited on pages 16 and 17.)

[22] D. Wu, F. Luo, Z. Wang, M. Li, J. Xu, M. He, C. Yang, and Y. Heng, "Study on the linearity of 20"dynode and mcp pmts," *Journal of Instrumentation*, vol. 18, no. 05, p. P05033, 2023. (Cited on pages 16 and 17.)

[23] H. Zhang, Y. Yu, K. Tariq, Z. Zeng, X. Li, C. Liu, D. Liu, C. Feng, L. Collaboration, *et al.*, "Photomultiplier tube performance of the wcda++ in the lhaaso experiment," *Nuclear Instruments and Methods in Physics Research Section A: Accelerators, Spectrometers, Detectors and Associated Equipment*, vol. 958, p. 162079, 2020. (Cited on pages 16 and 17.)

[24] Y. Yu, H. Lv, K. Tariq, D. Liu, X. Sheng, and C. Feng, "Study of the performance of photomultiplier tubes at high variable counting rates," *Nuclear Instruments and Methods in Physics Research Section A: Accelerators, Spectrometers, Detectors and Associated Equipment*, vol. 1008, p. 165433, 2021. (Cited on pages 16 and 17.)

[25] X. Wang and S. Cui, "Measurement of pmt charge nonlinearity using the continuous light attenuation method," *Journal of Instrumentation*, vol. 18, no. 12, p. T12010, 2023. (Cited on pages 16 and 17.)

[26] F. Longhitano, M. Buscemi, F. Barbato, D. Bonanno, D. Bongiovanni, R. Caruso, F. Guarino, and D. L. Presti, "A laser-based system for a fast and accurate measurement of gain and linearity of photomultipliers," *Journal of Instrumentation*, vol. 13, no. 01, p. T01007, 2018. (Cited on pages 16 and 17.)

[27] M. Friend, G. Franklin, and B. Quinn, "An led pulser for measuring photomultiplier linearity," *Nuclear Instruments and Methods in Physics Research Section*

*A: Accelerators, Spectrometers, Detectors and Associated Equipment*, vol. 676, pp. 66–69, 2012. (Cited on page 17.)

[28] D. L. Adhikari, *Neutron Skin Measurement of $^{208}$Pb Using Parity-Violating Electron Scattering*. PhD thesis, Idaho State University, Eastern Idaho, USA, 2021. (Cited on pages 17 and 56.)

[29] D. Adhikari and D. McNulty, "Pmt non-linearity characterization for precision parity experiments." Idaho State University, unpublished. (Cited on page 19.)

[30] A. Gunawardhana, "Moller-pmt-non-linearity-measurements." `https://github.com/LKbrilliant/MOLLER-PMT-Non-Linearity-Measurements`, 2024. (Cited on pages 22, 24, 28, 30, 33, 36, 44, and 47.)

[31] Thorlabs, "FW102C, FW102CNEB, FW212C, FW212CNEB motorized filter wheel user guide." `https://www.thorlabs.com/drawings/873b5e89737212fe-6079C961-CCA7-E91A-172A03D35A014820/FW212CNEB-Manual.pdf`. Accessed: 2024-12-02. (Cited on page 27.)

[32] M. Gericke, "Moller-intelec-protosoft." `https://github.com/mtgericke/MOLLER-IntElec-ProtoSoft/tree/rev1`, 2024. Commit:6c61c4d. (Cited on page 37.)

[33] R. Brun and F. Rademakers, "ROOT - an object oriented data analysis framework," *Nuclear instruments and methods in physics research section A: accelerators, spectrometers, detectors and associated equipment*, vol. 389, no. 1-2, pp. 81–86, 1997. (Cited on page 42.)

[34] C. R. Harris, K. J. Millman, S. J. van der Walt, R. Gommers, P. Virtanen, D. Cournapeau, E. Wieser, J. Taylor, S. Berg, N. J. Smith, R. Kern, M. Picus, S. Hoyer, M. H. van Kerkwijk, M. Brett, A. Haldane, J. F. del Río, M. Wiebe, P. Peterson, P. Gérard-Marchant, K. Sheppard, T. Reddy, W. Weckesser, H. Abbasi, C. Gohlke, and T. E. Oliphant, "Array programming with NumPy," *Nature*, vol. 585, pp. 357–362, Sept. 2020. (Cited on page 47.)

[35] I. Sobel, "An isotropic 3x3 image gradient operator," *Presentation at Stanford A.I. Project 1968*, 02 2014. (Cited on page 50.)

[36] W. R. E. Gonzalez Rafael C, *Digital image processing (fourth edition)*. Pearson Education, 2018. (Cited on page 50.)

[37] B. P. Lathi and R. A. Green, *Linear systems and signals*, vol. 2. Oxford University Press New York, 2005. (Cited on page 50.)

[38] G. Snedecor and W. Cochran, *Statistical Methods (8th ed.)*. Iowa State University Press, 1989. (Cited on pages 53, 57, and 61.)

[39] P. Virtanen, R. Gommers, T. E. Oliphant, M. Haberland, T. Reddy, D. Cournapeau, E. Burovski, P. Peterson, W. Weckesser, J. Bright, S. J. van der Walt, M. Brett, J. Wilson, K. J. Millman, N. Mayorov, A. R. J. Nelson, E. Jones, R. Kern, E. Larson, C. J. Carey, İ. Polat, Y. Feng, E. W. Moore, J. VanderPlas, D. Laxalde, J. Perktold, R. Cimrman, I. Henriksen, E. A. Quintero, C. R. Harris, A. M. Archibald, A. H. Ribeiro, F. Pedregosa, P. van Mulbregt, and SciPy 1.0 Contributors, "SciPy 1.0: Fundamental Algorithms for Scientific Computing in Python," *Nature Methods*, vol. 17, pp. 261–272, 2020. (Cited on pages 56, 57, and 59.)

# List of Figures

# List of Tables

# Listings

# Appendix A

# PMT Voltage Divider

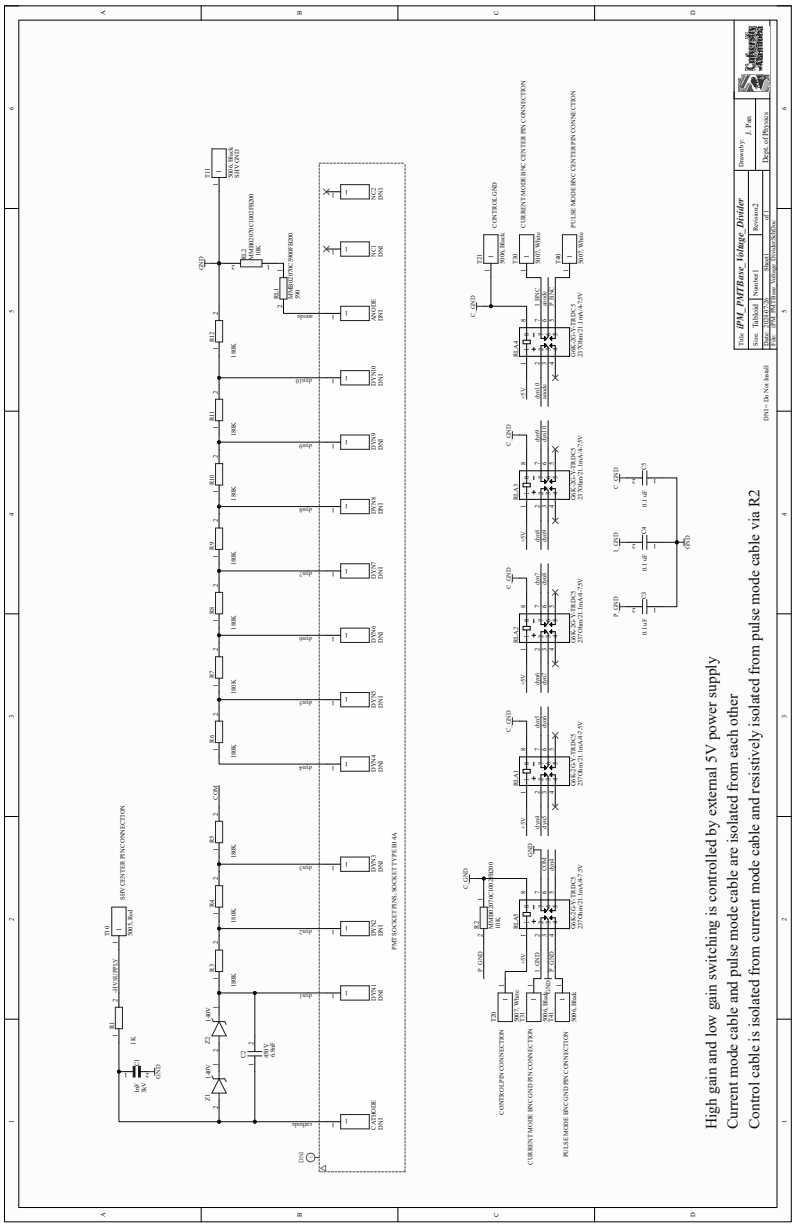

# Appendix B

# Database Structure

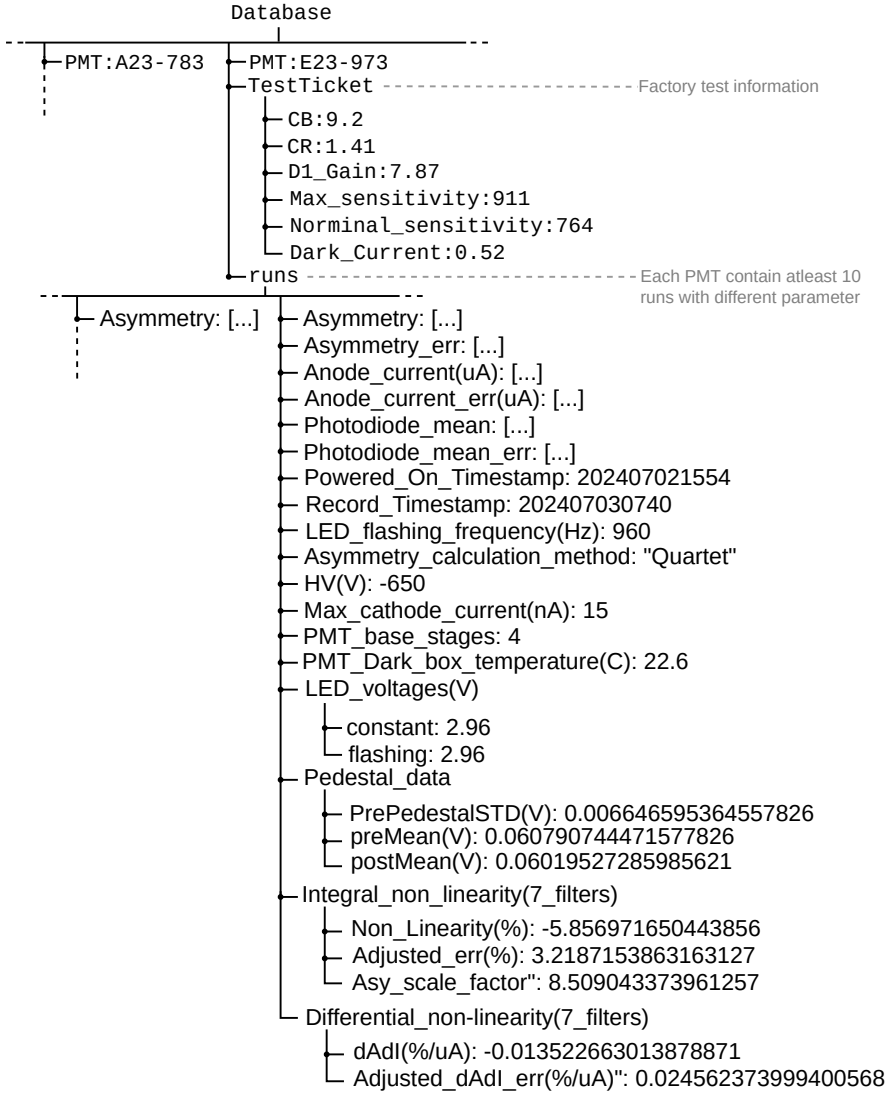

# Appendix C

# Pre-Test Checklist

# PMT Non-Linearity Pre-Tests Checklist

PMT Serial:..... Name:.....(Initials)

Start date:..... (YYYY-MM-DD) Time:.....(hh-mm)

Base-stages:..... High Voltage:.....V Operational Time:..... h

Notes:.....

01. Stop the data collection script ☐
02. Turn off all the power supplies **(HV, DCsupply, Photodiode Temp., Photodiode Amp.)** ☐
03. Note down the operational time for the previous PMT **(on paper and spreadsheet)** ☐
04. Swap the PMT ☐
05. Connect the **unitary gain base** to the new PMT **with HV cable** ☐
06. Remove the PMT cap and set the distance between PMT and filter wheel to **14cm** ☐
07. Cover the PMT and filter wheel with the cardboard dark box ☐
08. Lock the metal dark box and place the key on the designated location ☐
09. Set HV=**280V**, DC-ch3=**2V (Constant LED)**, Filter-Position=**9** ☐
10. Record the currents using the Picoammeter **(Wait until you read 0.01nA on the meter)** ☐

For 4 stage

| | Constant LED Voltage (V) | Cathode Current (nA) | |
|---|---|---|---|
| -v7 | | | 7 nA |
| -v9 | | | 9 nA |
| -v12 | | | 12 nA |

For 3 stage

| | Constant LED Voltage (V) | Cathode Current (nA) | |
|---|---|---|---|
| -v12 | | | 12 nA |
| -v15 | | | 15 nA |
| -v18 | | | 18 nA |

11. Unplug the Picoammeter from the power outlet (to reduce AC noise) ☐
12. Turn off the HV power supply ☐
13. Connect **3/4 stage base** to the new PMT **with HV cable** ☐
14. Adjust the distance between PMT and Filter wheel to be **14cm** ☐
15. Cover the PMT and filter wheel with the cardboard dark box ☐
16. Lock the dark box and place the key on the designated location ☐
17. Turn on High Voltage Power Supply **(4-Stage base: -600V, 3-stage base: -800V)** ☐
18. Turn on 3 Channel DC Power supply **[I/O]** ☐
19. Turn on the photodiode temperature controller ☐
20. Plug in the photodiode amplifier barrel connector ☐
21. Run the "`record.sh`" script ☐
22. Wait for the first run to complete ☐
23. Adjust the High Voltage if the max anode current is not within the **8-10uA** range. Input the new high voltage into the data collection script. **($HV_{min}$=-500V, $Hv_{max}$=-900V)** ☐

Note: If anode current cannot be set to the required range by adjusting HV, change the base